

NPS ARCHIVE
1967
LAFERTY, J.

AN INVESTIGATION OF THE AERODYNAMIC
RESPONSE OF A WIND ANEMOMETER

JOHN DENISON LAFERTY
and
WILLIAM FRANKLIN HICKS

AN INVESTIGATION OF THE AERODYNAMIC

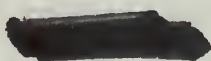
RESPONSE OF A WIND ANEMOMETER

by

John Denison Laferty
Lieutenant, United States Navy
B.S., Naval Academy, 1959

and

William Franklin Hicks
Lieutenant, United States Navy
B.A.E., Rensselaer Polytechnic Institute, 1959



Submitted in partial fulfillment of the
requirements for the degree of

AERONAUTICAL ENGINEER

from the

NAVAL POSTGRADUATE SCHOOL
June 1967

ABSTRACT

An experimental investigation was made to determine the aerodynamic response of a wind anemometer to unsteady air loads. The anemometer, a perforated drag sphere mounted upon a cylindrical pedestal, sensed dynamic pressure by a strain gage balance system.

The anemometer response was calibrated for static and dynamic mechanical inputs and for steady aerodynamic loads prior to the unsteady investigation. The unsteady environment was obtained in an oscillating flow wind tunnel which utilizes a rotating shutter valve to superimpose a harmonically varying velocity upon a mean free stream.

For steady flow conditions the anemometer drag coefficient remained essentially constant, apparently independent of Reynolds number. The anemometer responded well to the unsteady air loads at frequencies up to 20 cycles per second and mean dynamic pressures to 8.85 pounds per square foot. Unsteady aerodynamic response was qualitatively substantiated by a quasi-steady approximation to the measured unsteady drag.

ERRATA

page 14, line 14: should read contrast vice constrast.

page 17, line 26: should read shown vice fhown.

page 106, left hand sketch: should read steel
rod vice steel rid.

page 109, bottom line: add a period at the end
of the sentence.

page 110, line 3 of the 3rd paragraph: the symbol
w should be inserted in order to read "...the
product wA is...".

page 113, the line under Equation E.04: should
read E.o4 vice E,04.

TABLE OF CONTENTS

Section	Page
1. Introduction	13
2. Experimental Equipment and Procedures	15
Anemometer Calibrations	16
Nonsteady Tunnel Investigation	20
Nonsteady Tunnel Instrumentation	22
3. Experimental Results and Discussion	24
Run Program	24
Data Reduction	25
Drag-Steady Values	26
Unsteady Drag and Phasing	27
Quasi-Steady Assumption	29
Drag Ratio	30
Harmonic Considerations	32
4. Conclusions	34
5. Bibliography	99
 APPENDIX	
A Accelerometer Calibrations	100
B Anemometer Corrections for Tunnel Floor Accelerations	102
C Hot Wire Response	106
D Tunnel Floor Velocity Effects	110
E Quasi-Steady Theory	112
F Fourier Analysis of Signals	114

LIST OF TABLES

Table		Page
1	Reduced Data - Small Vanes	35
2	Reduced Data - Medium Vanes	40
3	Reduced Data - Large Vanes	45
4	Anemometer Phase Lag - Small Vanes	50
5	Anemometer Phase Lag - Medium Vanes	53
6	Comparison of Fourier Components	56
7	Reduced Data - Small Vanes	58
8	Reduced Data - Medium Vanes	61

LIST OF ILLUSTRATIONS

Figure		Page
1	Inertial Response Investigation	63
2	Anemometer Static Calibration	64
3	Anemometer Inertial Response	65
4	Shutter Vane Blockage	66
5	Diagram of Data Acquisition System	67
6	Nonsteady Tunnel Installation	68
7	Sensor Installation Details	69
8	Anemometer Drag vs. Dynamic Pressure (W.C.R. Tunnel)	70
9	Mean Anemometer Drag vs. Mean Dynamic Pressure (Nonsteady Tunnel)	71
10	Unsteady Drag vs. Frequency (Small Vanes)	72
11	Unsteady Drag vs. Frequency (Medium Vanes)	73
12	Unsteady Drag vs. Frequency (Large Vanes)	74
13	Anemometer Phase Lag (Small Vanes)	75
14	Anemometer Phase Lag (Medium Vanes)	76
15	Sample Waveforms (Small Vanes)	77
16	Sample Waveforms (Medium Vanes)	78
17	Signal Distortion of Large Vanes	79
18	Drag Ratio Variation (Small Vanes, $q = 1.0$ psf)	80
19	Drag Ratio Variation (Small Vanes, $q = 2.3$ psf)	81
20	Drag Ratio Variation (Small Vanes, $q = 4.2$ psf)	82
21	Drag Ratio Variation (Small Vanes, $q = 5.9$ psf)	83
22	Drag Ratio Variation (Small Vanes, $q = 7.6$ psf)	84
23	Drag Ratio Variation (Medium Vanes, $q = 0.7$ psf)	85
24	Drag Ratio Variation (Medium Vanes, $q = 1.4$ psf)	86

Figure		Page
25	Drag Ratio Variation (Medium Vanes, $q = 2.2$ psf)	87
26	Drag Ratio Variation (Medium Vanes, $q = 2.6$ psf)	88
27	Drag Ratio Variation (Medium Vanes, $q = 2.8$ psf)	89
28	Drag Ratio Variation (Large Vanes, $q = 0.6$ psf)	90
29	Drag Ratio Variation (Large Vanes, $q = 1.2$ psf)	91
30	Drag Ratio Variation (Large Vanes, $q = 1.3$ psf)	92
31	Drag Ratio Variation (Large Vanes, $q = 1.5$ psf)	93
32	Drag Ratio Variation (Large Vanes, $q = 1.7$ psf)	94
33	Second Harmonic Influence	95
34	Sphere Vibration	96
35	Statham Accelerometer Calibration	97
36	Sensor Separation Phase Shift	98

LIST OF SYMBOLS

<u>Symbol</u>		<u>Units</u>
A	Projected frontal area of drag sphere	0.268 ft ²
C _D	Drag Coefficient, $\frac{D}{qA}$	_____
D	Steady Drag	lbs
d(t)	Unsteady Drag	lbs
E ()	Electrical signal representing analog of term in subscripts, steady (D.C.) component	volts
e ()	Electrical signal representing analog of term in subscripts, time dependent component	volts
f	Frequency	cycles/sec
g	Acceleration due to gravity	32.2ft/sec ²
l	Diameter of sphere	0.583 ft
q	Dynamic pressure, $1/2 \rho v^2$	lbs/ft ²
S	Strouhal number, $\frac{fl}{v}$	_____
V	Steady wind velocity	ft/sec
v(t)	Unsteady wind velocity component	ft/sec
ζ	Damping ratio, fraction of critical	_____
ρ	Air density	slugs/ft ³
ϕ	Phase angle	degrees
ω	Circular frequency, $2\pi f$	radians/sec

Subscript Notation

A	Anemometer
B	Bently reluctance gage
C	Accelerometer
H	Hot wire
o	Zero frequency value

Superscript Notation

\bar{y} Mean value of quantity, $y(t)$,

$$= \lim_{T \rightarrow \infty} \frac{1}{T} \int_0^T y(t) dt$$

\hat{y} Root mean square of quantity, $y(t)$, = $\sqrt{y^2}$

$$= \lim_{T \rightarrow \infty} \frac{1}{T} \int_0^T y^2(t) dt$$

Note: Symbols associated with a particular derivation are defined when first used in the text.

ACKNOWLEDGEMENT

The Authors wish to express their deepest appreciation to Dr. Louis V. Schmidt for his many valuable suggestions and assistance in the preparation of the manuscript.

Grateful acknowledgement is also due Dr. James A. Miller for his instruction and cooperation in the operation of the oscillating flow wind tunnel, and engineering technicians Ted Dunton and Stanley Johnson for their efforts in behalf of the project.

In addition, the efforts of Mr. W. H. Reed of NASA who was instrumental in the sponsoring of the project, 80 x 0108 R&D, are sincerely appreciated.

Finally, to the Authors wives, Jean and Mary; much is due to their patience, encouragement and cheerfulness when they were sorely needed.

1.. Introduction

Structures exposed to ground winds can experience, depending on the geometry and/or motion involved, both steady and unsteady bending, torsional, and distortional loads. The effects of wind loads upon the elastic response of large structures have been observed as the oscillations of tall slender smoke stacks and antennas, "galloping" of transmission lines, warping motion of suspension bridges, and more recently as the vibrations of space launch vehicles while on the launch pad. These effects have been the subjects of such investigators as Den Hartog [3] , Scruton and Walshe [10] , Scruton [11] and Buell, et al [1] .

Many of the studies conducted on ground wind loads have used wind tunnel tests in which the velocity was steady in magnitude and direction and whose profile was essentially uniform (tunnel boundary layer was small compared to model dimensions). In reality the ground wind is rarely constant in either magnitude or direction and the boundary layer of a ground wind can be several hundred feet thick. A structure's response to a steady uniform flow can be quite different from its response to a flow which varies in space and time. Although correct reproduction of aerodynamic flow properties as a prerequisite for meaningful dynamic model tests has been recognized for some time, possibly the first tests in which the dynamics of the structure and the turbulent boundary layer flow were both reproduced occurred in 1964, directed by A. G. Davenport [2] in cooperation with J. E. Cermak using the Army meteorological wind tunnel at the Colorado State University.

Any meaningful prediction of wind loads must be based on a knowledge of the wind itself, which in turn implies accurate measurements of the wind. These measurements are becoming increasingly more important as the studies of wind loading on large elastic structures become more

detailed. Measurement of fluctuating, gusty winds is difficult with instruments that are frequency-response limited, and hence can only indicate averages of the various components. Recently the National Aeronautics and Space Administration, Langley Research Center (NASA Langley), Hampton, Virginia, has developed a fast response anemometer capable of following wind fluctuations in the range of zero to five cycles per second. According to Reed and Lynch [9] this development resulted from the gratifying performance of a ping-pong ball, attached to a single component force pick-up, which was used to measure time fluctuations of low level dynamic pressures in the early 1950's. Additionally, wind tunnel testing at NASA/Langley demonstrated that the steady drag force vector for a perforated hollow sphere remained aligned with the steady wind velocity vector within a tolerance of ± 3 degrees. In contrast a smooth sphere exhibited an abrupt, random shift of the drag vector to either of two positions, symmetrically located about 15 degrees from the wind direction. The latter result is not surprising since the separation point for the flow is not geometrically stabilized as is the case for a perforated sphere. The choice of a perforated sphere for use in a drag anemometer is a logical one based on these observations.

The drag sphere anemometer, in addition to fast response, has several other important characteristics:

- (1) measurable drag forces are generated in the low dynamic pressure regions.
- (2) the coefficient of drag is constant over a wide range of velocities, hence dynamic pressure can be readily interpreted from the drag.

(3) the natural frequency is high compared to the frequencies of interest.

(4) the drag force vector remains aligned with the wind direction.

Current use of the drag sphere anemometer has been indicated by Duncan and Foughner [4] as part of a continuing ground wind loads investigation at Wallops Island, Virginia.

An oscillating flow may be defined to consist of a harmonically varying velocity superimposed upon a constant free stream. Low speed oscillating flow investigations have, in general, been limited. Miller [7] has investigated boundary layer transition over a flat plate. Murphy [8] recently investigated the pressure distribution about a circular cylinder in an unsteady flow. No investigations concerning perforated spheres in an oscillating flow were found in the literature.

This investigation was undertaken to determine the aerodynamic behavior of the perforated sphere in an oscillating flow. The frequency range of interest was from zero to twenty cycles per second, with dynamic pressures to 8.85 pounds per square foot, which approximately corresponds to air velocities of 88 feet per second, or 60 miles per hour.

2. Experimental Equipment and Procedures

The perforated sphere anemometer used in these investigations was supplied to the Naval Postgraduate School by the Aeroelastic Branch of NASA (Langley) in support of the aerodynamic frequency response program. The anemometer was floor mounted when installed in either the 3.5 x 5.0 foot low-speed wind tunnel or the 2.0 x 2.0 foot nonsteady wind tunnel, both of which are located at the Naval Postgraduate School, Monterey, California.

The seven-inch drag sphere was made of plastic (weight and corrosion considerations) and had forty 0.75-inch diameter perforations uniformly distributed over the surface (see Figure 1). It was mounted on a two-component strain gage balance system oriented such that the balances sensed the two horizontal components of sphere drag force. Static inertial compensation was provided by an internal counterweight arrangement which could be positioned such that the center of gravity of the sphere system corresponded to the effective center of the strain gage balances. No adjustments of the balance weight were made following receipt of the anemometer from NASA/Langley.

Anemometer Calibrations

The anemometer strain gage balances, conventional 350 ohm full-bridge circuits, were statically calibrated through force ranges that corresponded to gage strain levels of approximately ± 1000 micro-inches per inch. With a bridge excitation level of 10.0 volts (D.C.), the sensitivities were found to be approximately 4.42 and 4.15 millivolts per pound respectively, with the results being linear in the range investigated. See Figure 2 for actual calibration curves.

Although both balances were calibrated in order to allow simultaneous evaluation of lateral (side) and drag forces, only one balance was operative following the calibrations, since the second balance became unusable due to an apparent unbonding of one of the strain gage elements. Consequently the scope of the program became restricted to a frequency response evaluation of sphere drag force.

Astrodata differential D.C. amplifiers, model A885, were used in these calibrations, with a gain of 100 to increase the output level to a value suitable for magnetic tape recording, and to allow biasing of

the steady drag component so that only the unsteady portion of the signal would be recorded. Balance sensitivities stated in a previous paragraph are equivalent to amplifier input values.

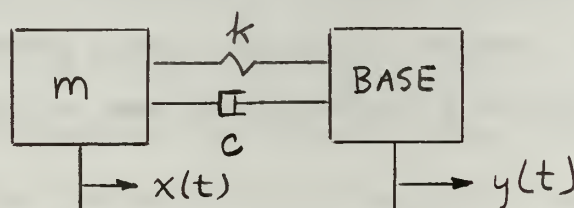
Since the anemometer was to be exposed to velocity perturbations while attached to the floor of the nonsteady tunnel, which definitely is a vibratory environment, it was necessary to consider the inertial response traits of the anemometer for possible correctional terms during data reduction. The need for such considerations can be visualized by realizing that the strain gage balance is an elastic system that relies upon relative motion between the sphere and the pedestal base in order to produce measurable strains in the balance system.

It would normally be necessary to consider both rotational and translational inertia terms, however, during preliminary tests the nonsteady wind tunnel (described later in this section) was found to have floor motion predominantly in a direction tangential to the floor with maximum accelerations of 2.0 "g's" at 10.0 and 17.5 cps. This acceleration direction is dominant since the tunnel test section is relatively stiff, and the tunnel is mounted on a framework of steel pipes which act like a "bent", without significant bending moment constraint at the joints. Therefore a calibration was made only in the translational vibration mode.

The inertial frequency response calibration was performed over a frequency range of 5 to 100 cps. A Calidyne Shaker, model 219, operated by a Ling control console, model CP 3/4 was used to accelerate a steel plate upon which the anemometer and reference accelerometer were mounted, as shown in Figure 1. Horizontal accelerations were measured with a Statham accelerometer, model SCO 210, which was used as a reference sensor unit in both the mechanics laboratory and the nonsteady wind

tunnel. The primary range of frequencies was below 100 cps, and this was readily measured by the Statham strain gage device since it had a usable frequency range from 0(D.C.) to 150 cps, and an acceleration range of ± 5 "g's" (see Appendix A for accelerometer calibration). The shaker was connected to the plate by a 1/16 inch diameter steel wire flexure coupling, which had an estimated critical buckling load of 5400 pounds. A wire flexure coupling was used to avoid imposing transverse loads onto the shaker table. The steel plate rested upon a steel surface table which was adjusted to be level. The surface table and the plate had polished surfaces, and an oil film was applied between the moving surfaces in order to reduce the level of frictional forces. The coupling was positioned such that the axial force transmitted through the wire coupling acted approximately through the center of mass of the combined dynamic assembly (plate, anemometer, and accelerometer).

If the anemometer were represented as a system with a single degree of freedom:



then, the equation of motion for the freely vibrating mass is:

$$m \ddot{x} + c(\dot{x} - \dot{y}) + k(x - y) = 0. \quad (2.01)$$

Let $z = x - y$, and rewrite

$$m \ddot{z} + c \dot{z} + kz = -m \ddot{y}$$

then for sinusoidal motion of the base, $y = y_0 \sin \omega t$

$$\ddot{z} + 2\zeta\omega_N \dot{z} + \omega_N^2 z = y_0 \omega^2 \sin \omega t \quad (2.02)$$

where

$$2 \zeta \omega_N = \frac{c}{m} \quad , \quad \omega_N^2 = \frac{k}{m}$$

The solution of (2.02) is:

$$Z(t) = \frac{y_0 \omega^2 [\sin(\omega t - \phi)]}{\frac{1}{\omega_N^2} \sqrt{\left[1 - \left(\frac{\omega}{\omega_N}\right)^2\right]^2 + 4 \zeta^2 \left(\frac{\omega}{\omega_N}\right)^2}}$$

$$\phi = \arctan \left\{ \frac{\left[2 \zeta \frac{\omega}{\omega_N} \right]}{\left[1 - \left(\frac{\omega}{\omega_N}\right)^2 \right]} \right\}$$

where $Z(t)$ is the displacement of the anemometer force pickup relative to the base, and $y_0 \omega^2$ is the magnitude of the harmonic forcing function.

Accelerations of various magnitudes and constant frequency were applied to the base plate at four intervals up to and down from the maximum of 2.0 "g's". The anemometer response $Z(t)$, accelerometer output, $y_0 \omega^2$, and phase difference between these sensors were recorded at each level of acceleration. The frequency was increased and the procedure repeated. Figure 3 is a summary of the anemometer inertial response calibration.

The anemometer natural frequency was found to be approximately 60 cps as indicated by maximum response from oscilloscope traces, and by observation of large excursions of the perforated sphere. For frequencies greater than 60 cps, the response wave forms became very distorted. Considerable difficulty was encountered in the determination of a 90 degree phase shift between input and output. The difficulty was attributed to the anemometer not behaving as a system with a single degree of freedom.

Anemometer damping was evaluated by observing the output response to a step input. No low frequency oscillation ensued for any of the step inputs, and it was concluded that the system fundamental mode was at least critically damped. Examination of the response, however, with the single sweep capability of the Tektronix (type 551) oscilloscope, revealed a high frequency (greater than 100 cps) signal superimposed upon the basic wave form. The excitation of this high frequency signal was controllable to a degree and was apparently caused by a ringing mode of the perforated shell.

Nonsteady Tunnel Investigation

The investigation of anemometer unsteady aerodynamic response was conducted in the low speed, oscillating flow tunnel located in the Aeronautical Laboratories of the Naval Postgraduate School. The open circuit tunnel has a 24 inch square test section, 223.5 inches long. Air is driven by two series-connected Joy Axivane fans connected directly to 100 hp, 1750 rpm electric motors. The tunnel has a bell-mouthed entrance with a nozzle area contraction ratio of 16:1. There are three fine mesh screens in the settling section area which reduce steady flow turbulence levels in the test section below 0.1 percent of mean velocity.

Construction of the test section floor and ceiling is from 2.0 inch thick aluminum, the sides from 2.0 inch lucite. Heavy construction was necessary to reduce structural deflections caused by large variations in static pressure.

Oscillating flow was created by a rotating shutter valve assembly located at the trailing edge of the test section and driven through belts by a variable speed electric motor. The shutter blades were removable to permit installation of various widths that could enclose

from 50 to 100 percent of the test section area, and which provided unsteady velocity amplitudes from 1.3 to 84.0 percent of free stream velocity. Various pulley ratios of the belt drive were available effecting an operational range of frequency from 2 cps to 933 cps.

Murphy [8] performed steady flow velocity surveys across the test section and found that the variation of V relative to V_{\max} was less than ± 1 percent for distances greater than three inches from the tunnel walls.

For the actual nonsteady tunnel tests it was desired to subject the anemometer to five values of mean dynamic pressure with each of the three available shutter vane sizes. The investigation in general included fifteen points of data for each run at various frequencies up to 20 cps.

In order to determine the effect of blockage produced by the rotating shutter vanes, and to insure that the hot wire system would perform satisfactorily, several trial runs were performed with the anemometer absent from the test section. Dynamic pressures of 7.8 and 15.6 pounds per square foot (psf) were set with the vanes horizontal. The hot wire DC output was set to read full scale (1.0 volts) for zero frequency and maximum velocity. The tunnel was operated at various frequencies and the drop of the DC level of the hot wire was noted. Figure 4 is typical of results for an initial mean dynamic pressure of 7.8 psf. Post-run checks were performed to ensure the absence of hot wire drift.

With the information obtained from an evaluation of the blockage effect, a zero frequency dynamic pressure was selected. The hot wire DC attenuation was adjusted to full scale, and the zero frequency RMS values were recorded for the anemometer, hot wire, and accelerometer.

The speed of the rotating shutter valve was initially adjusted to the minimum, 3.6 cps, for the combination of pulley ratios used. After amplified anemometer and hot wire DC values were biased to zero and the oscillation frequency was stabilized, tape recording of signals for the particular data point was commenced. RMS values of the anemometer, hot wire, frequency, and mean dynamic pressure were logged manually. This procedure was repeated at seven increments of frequency up to and down from the maximum of 20 cps. Post-run zero frequency and zero dynamic pressure were noted. This procedure of data acquisition was repeated at five levels of dynamic pressure for each of the shutter vane widths.

Nonsteady Tunnel Instrumentation

The Ampex magnetic tape system used was an electron tube type model FR-100 with 14-channel recording capability. Both frequency modulated and direct record amplifiers were available. A tape speed of 7.5 inches per second was used throughout the data acquisition, which provided a flat frequency response on the FM channels from 0 to 1250 cps. Three frequency modulated channels were used to record anemometer, hot wire, and accelerometer signals, whereas voice information, to identify blocks of taped data, was recorded through a direct record amplifier.

A Tektronix type 555 oscilloscope with a pair of 4-channel pre-amplifiers was used to simultaneously monitor original and recorded data.

An integrating digital voltmeter (Vidar 510) was used to alternately monitor the DC output of the anemometer bridge circuit and the hot wire anemometer. The DC values of the amplified signals from both

instruments were maintained at values as near to zero as possible by a battery-supplied bias voltage. The DC biasing permitted the tape recording of optimum level AC signals. Figure 5 presents a block diagram of the entire data acquisition system shown by photograph in Figure 6. Details of the anemometer installation are shown in Figure 7. Shielded co-axial cables with BNC fittings were used to reduce the influence of extraneous signals, for example 60-cycle ground loops. A centrally located switch panel afforded an orderly flow of data and convenient monitoring of information.

The hot wire probe was constructed at the Postgraduate School by soldering an 0.0015 inch diameter tungsten wire on a pair of jewelers broaches. The jewelers broaches were imbedded in epoxy plastic, which was fitted to a 1/4 inch hollow steel rod. The performance of the Security Associates bridge circuit/analog computer system was excellent. Repeated results assured a linear DC variation from zero to full scale and a high degree of system stability was noted. The sensitivity of the system was such that outside wind fluctuations during steady operation of the wind tunnel were detectable.

3. Experimental Results and Discussion:

Run Program

The investigation of the aerodynamic response of the wind anemometer performed in the oscillating flow tunnel was separated into three phases: (a,) tunnel familiarization and calibration of flow, (b.) evaluation of the steady flow drag, and (c.) the determination of unsteady drag in oscillating flow. The phases may be further subdivided as follows:

Phase I Calibration

Run	q (psf)	f (cps)	Objectives
C1	7.8	3.6 - 20.0	Tunnel familiarization, check blockage effects on small vanes, and evaluate hot wire performance
C2	"	"	Medium vane blockage
C3	"	"	Large " "
C4	15.6	"	Small " "
C5	"	"	Medium " "
C6	"	"	Large " "

Phase II Steady Drag

Run	q (psf)	f (cps)	Objectives
C7	1.3-15.7	0	Determine anemometer output vs q
C8	1.0-15.6	"	" " " " "
C9	2.1-15.6	0 - 19.0	Determine velocity perturbation effects upon mean value of drag

Phase III Unsteady Drag

Run	q (psf)	f (cps)	Objective
1-4, 10	1.0-7.6	3.6 - 19.3	Effects of small vanes (small velocity perturbation) upon unsteady drag
5-9	0.6-1.7	3.6 - 21.0	Effects of large vanes upon unsteady drag
11-15	0.7-2.9	"	" " medium " " " "
16-18	4.2-7.8	3.6 - 19.1	" " small " " " "
19,20	2.1,2.6	"	" " medium " " " "

Data Reduction

The initial step in the reduction of experimental data was to evaluate the operating conditions for which the anemometer output was significantly affected by tunnel floor accelerations. In consideration of the inherent fluctuations of anemometer RMS output, "significantly" was interpreted to mean those data points which influenced the total anemometer signal by more than five percent. Frequencies which caused excessive tunnel vibration were avoided, but using the criteria above it was necessary to correct about 25 percent of the data points.

A method to correct the anemometer response, both in magnitude and phase, is presented in Appendix B. An important assumption in the analysis is that the dominant floor accelerations are of a sinusoidal nature and of the same frequency as the oscillating air flow. The assumption was based upon oscilloscope photographs that were made of the response signals reproduced from the tape recorded data. Two Kron-Hite band pass filters were employed in the playback channels to eliminate the high frequency components of the actual signals. Tables 1, 2 and 3 contain the corrected data for small, medium and large shutter vanes respectively.

Appendix C is a development of hot wire response to a base or floor acceleration based upon elementary beam theory. For all values of frequency and acceleration in the range investigated this effect can be neglected. The effect of tunnel floor velocity on hot wire response, considered in Appendix D, is less than two percent of the unsteady air velocity and therefore negligible. The hot wire output can then be considered as the true behavior of the oscillating air flow.

The phase differences between (a.) anemometer and hot wire signals and (b.) anemometer and accelerometer signals were determined by averaging the output of an AD-YU phase meter for an interval of taped data (30-45 secs). The difference was qualitatively substantiated by photographic measurements. Phase angles of the anemometer relative to the hot wire are listed in Tables 4 and 5 for the small and medium shutter vanes. Phase differences for the large vanes are omitted due to the large degree of variation resulting from the complex waveform.

Drag-Steady Values

Figures 8 and 9 are plots of raw anemometer drag as a function of dynamic pressure as obtained in the steady West Coast Research (W.C.R.) tunnel and in the oscillating flow tunnel for zero frequency. The steady coefficient of drag was evaluated for each set of data using the anemometer static sensitivity (Figure 2) previously determined. The drag coefficient obtained from the W.C.R. tunnel was 0.69, while the non-steady tunnel yielded 0.71, which includes an estimated correction for solid blocking. For both evaluations, the anemometer output was a linear function of dynamic pressure in the range investigated, which indicated that the drag coefficient for the perforated drag sphere was apparently independent of Reynolds Number.

Reed [9] has shown for the one-dimensional case of a non-steady velocity $v(t)$ superimposed upon a mean free stream V that the time average of the instantaneous velocity squared is

$$\overline{V^2} = V^2 \left(1 + \frac{\overline{v^2}}{V^2} \right)$$

Taking the square root of both sides, expanding the right hand side in a binomial series, and retaining first order terms yields:

$$\sqrt{\overline{V^2}} = V \left[1 + \frac{1}{2} \frac{\overline{V'^2}}{V^2} \right]$$

In other words, the mean velocity when determined by a measurement of dynamic pressure (or V^2) is biased by the turbulence in the flow.

The unsteady tunnel was used to determine the effect of an oscillating flow on the mean drag of the anemometer. The first step was to measure the drag in a steady flow over a dynamic pressure range of 1.04 to 15.6 pounds per square foot. This test corroborated earlier results obtained in the W.C.R. tunnel. Next the mean anemometer drag was recorded in an oscillating flow (both small and medium sized vanes were used) over a mean dynamic pressure range of 2.08 to 8.84 pounds per square foot. The mean drag was recorded at about 16 discrete frequencies between 3.6 and 19.1 cycles per second at each of 9 dynamic pressure levels. It was found that the mean anemometer drag at a mean dynamic pressure was independent of flow oscillation frequency and equal to the steady flow value. The results of the steady and the unsteady flow tests are shown in Figure 9.

Unsteady Drag and Phasing

The variation of unsteady drag as a function of frequency and dynamic pressure for the case of the small shutter vanes is presented in Figure 10. The individual data points for the curves were obtained by positive incremental frequency steps up to the maximum obtainable, and then by negative steps to the minimum frequency. A high degree of repeatability was obtained for the small vanes. Unsteady drag, for the lowest dynamic pressure (1.0 psf) in the series, remained essentially constant with frequency, while each of the other curves for higher

dynamic pressures generally decreased with frequency and apparently approached a limiting value. It is interesting to note that the variation of unsteady drag with dynamic pressure at a constant frequency of 19 cps is approximately one-fifth the value at a frequency of 3.6 cps.

All of the curves exhibited a peak in the vicinity of 10 cps, the relative magnitude of which increased with dynamic pressure. Also, at frequencies near 10 cps, the ratio of \hat{v}/V was a local maximum for the particular run, and is believed to cause the rise in unsteady drag. The reason for an increase in this velocity perturbation ratio at this frequency is not known but was attributed to the flow characteristics of the tunnel.

The unsteady drag variation for the medium and large shutter vanes is shown in Figures 11 and 12. For the case of medium vanes an additional peak appears at approximately 17.5 cps, which also can be attributed to a local maximum of \hat{v}/V . Although the medium-vane curves display a lower degree of consistency than do the small-vane curves, the trend of decreasing magnitudes with frequency is maintained, as is the trend toward a limiting value for each dynamic pressure with increasing frequency. The large shutter-vane results display an even lower degree of consistency, but still display the drag peaks at approximately 10 and 17 cps. Unsteady drag dependence on dynamic pressure, as indicated by the smaller vane data, is substantiated for frequencies less than 11 cps; for frequencies greater than 11 cps the scatter of data precludes immediate interpretation.

The anemometer phase lag to an aerodynamic forcing function is affected both by dynamic pressure and frequency as shown in Figure 13, which is a summary of results for the small velocity perturbations

($\hat{v}/V \doteq 0.02$). Phase lag generally increases with frequency and apparently has no dependence upon dynamic pressure. The increase in phase lag with frequency up to about 16 cps was also observed during the inertial investigation described in Section 2 (cf., Figure 3).

With the exception of the lowest dynamic pressure (0.73 psf) in the medium vane runs (where $\hat{v}/V \doteq 0.12$), anemometer phase lag remained near zero up to a frequency of 12 cps, where a rapid increase was observed toward a peak value occurring at approximately 15 cps. See Figure 14.

Quasi-Steady Assumption

A theoretical treatment of bluff body oscillating flows is very scarce in published literature. Isaacs [6], in an investigation of the non-steady flow over a helicopter blade at small angle of attack, has approached the problem for a potential flow case. However, the analysis included two limiting assumptions: the flow was two-dimensional over a flat plate airfoil, and the vortices shed remain in the plane of the airfoil. The method is not directly applicable to the three-dimensional sphere problem because of obvious differences between idealized potential flow and bluff body separated flow, but Isaacs does suggest that the lift on the airfoil can be evaluated from an averaging of the instantaneous lift due to the variable velocity.

Fung [5] further defines this quasi-steady principle, which assumes that the characteristics of an airfoil in an unsteady flow at any instant of time are equal to the characteristics of the same airfoil in a steady flow with flow parameters equal to the instantaneous values.

Appendix E is a development of the quasi-steady principle for the three-dimensional sphere.

Drag Ratio

Anemometer drag ratio (DR_A) is defined as the quotient of unsteady drag divided by drag produced by the steady component of velocity. The quasi-steady drag ratio (DR_Q) is approximately equal to $2 \frac{\hat{v}}{V}$ and is developed in Appendix E. These ratios are plotted versus Strouhal number ($\frac{f}{V}$) to indicate the variation with frequency and mean velocity, and to evaluate the degree of validity of the quasi-steady assumption. The scales for the coordinate axes are not consistent due to the large variation of maximum values between runs.

The quasi-steady assumption agrees best with the anemometer response for the runs with the small shutter vanes installed. Two factors are significant for this result: (1) velocity perturbations produced by the small vanes are better approximations to harmonic functions, and (2) the ratio of \hat{v}/V is small, which is inherent to the approximation of quasi-steady theory. Photographs of response signals from oscilloscope traces are presented in Figures 15 and 16 to illustrate the effects of shutter vane size upon the deviation from harmonic perturbations.

The variation of drag ratio with Strouhal number and dynamic pressure for five runs with the small shutter vanes installed is contained in a sequence of figures beginning with Figure 18. The anemometer response curves have the same form as the curves for the quasi-steady approach (based upon the hot wire output) or, in other words, the anemometer is sensing the velocity perturbations throughout the frequency range. The level of response increases, as expected, with increasing dynamic pressure. However, for a given dynamic pressure,

both the average value of the drag ratio and the quotient, DR_A/DR_Q , decrease with increasing Strouhal number. Figures 20, 21 and 22 also contain results obtained from separate test dates to demonstrate the repeatability of data and thereby provide a confirmation of results.

Drag ratio variation obtained with the medium vanes installed is presented in a second sequence of figures, starting with Figure 23. The correlation of anemometer and quasi-steady results is still maintained, although the appearance of a second peak occurs at a Strouhal number of 0.22 (the equivalent frequency is approximately 17.5 cps). For the medium vanes, the average value of the drag ratios are on the order of seven times the small vane values, although the actual vane size has been increased only 50 percent.

Large vane effects upon drag ratio exhibit more deviation and less repeatability than the vane sizes previously considered. The large vanes create more distortion of the velocity perturbation, and anemometer response becomes more random in nature. Large fluctuations (50% of the freestream value) produced anemometer response that was generally about half of the quasi-steady value, as shown in the series of figures starting with Figure 28.

Due to the non-linear variation of the tunnel nonsteady velocity for a given mean dynamic pressure and shutter size, as a function of frequency, it is not clear what the effects are, if any, of aerodynamic damping upon anemometer response. However, a tendency toward reduced response (as evidenced by the reduced drag ratio in relation to the hot wire value) has been observed for a combination of the greater dynamic pressures, large fluctuations, and higher frequencies.

Throughout the nonsteady investigation, the tunnel radiated various levels of noise dependent upon frequency, shutter size, and dynamic pressure. If the inlet test section is compared to an open organ pipe, then the fundamental frequency may be calculated equal to 27 cycles per second. The peaks of the drag ratio curves may then reflect a significant degree of sub-harmonic response.

Harmonic Considerations

The output signals obtained from the anemometer and hot wire were obviously not true sinusoids. Observations of these signals indicated a possible significant higher harmonic component, as shown in Figure 33. The anemometer response has been shown to follow the gross aerodynamic input reasonably well but a more quantitative definition of response was desired. Therefore, the gross signals were examined to determine the amplitude and phase relationships among the fundamental, second, and third harmonic components and between the anemometer and hot wire signals. A numerical approximation of a Fourier analysis was used, as indicated in Appendix F. Since the required computations were performed with a desk calculator, only a few selected data points were analyzed. Results of this examination are shown in Table 6. As a check on the consistency of the approximations, and the results, two different data samples from runs 1-2 and 2-4 were analyzed. The data samples from run 1-2 were taken from different cycles on the same oscilloscope photograph, while the samples from run 2-4 were taken from separate photographs. Quantities with good correlation, and discrepancies, are obvious in Table 6. The existence of a significant second harmonic component is definitely shown, having an average amplitude, over the points tested, of 23 percent and 17 percent of the fundamental component amplitudes for the hot wire and anemometer respectively. Corresponding

values for the third harmonic component are 4 and 6 percent. The fundamental component of the hot wire led that of the anemometer by an average of 9 degrees. The phase angles between hot wire and anemometer computed for the second and third harmonic components were random in sign and magnitude.

Inspection of several oscilloscope photographs (cf. Figure 34) revealed a higher frequency superimposed on the basic signal. This higher frequency, about 145 cps, shows up on both hot wire and anemometer signals, but it is much more prominent for the latter. The sensitivity of the anemometer to this input frequency is believed due to the oscillations of the sphere itself, as opposed to the sphere-pedestal combination. This "ringing" of the sphere was also noted during part of the inertial response calibration to determine anemometer damping ratio.

4. Conclusions

The natural frequency of the anemometer was 60 cps with approximately a critical amount of damping.

For steady flow conditions the anemometer has a constant drag coefficient, thus apparently independent of Reynolds Number within the dynamic pressure range of 0.78 to 15.6 psf.

The average drag measured by the anemometer in an unsteady flow for a given mean dynamic pressure was independent of frequency and equal to the drag measured in a steady flow at the same dynamic pressure.

Unsteady drag, as determined from a quasi-steady approach, provided a good qualitative comparison to the unsteady drag measured by the anemometer. Quantitative results of the quasi-steady assumption provided only an order of magnitude indication of anemometer response.

The unsteady component of anemometer response increased with mean dynamic pressure and with unsteady velocity. For the runs performed with the small shutter vanes, the unsteady anemometer response relative to the unsteady velocity decreased with increasing frequency, and apparently approached a limiting value.

The investigation was complicated by an amplification of the unsteady air flow at several frequencies in the range of interest, and by a significant second harmonic component, about 25 percent of the fundamental amplitude.

It is recommended that future investigation be directed toward a thorough definition of the oscillating flow behavior of the nonsteady tunnel throughout its operating range.

TABLE 1
REDUCED DATA: SMALL VANES

Run*	f (CPS)	q (psf)	e _A (VRMS) x 10 ²	$2 \frac{\hat{v}}{V}$
1-1	3.6	4.21	0.031	0.068
1-2	5.0	4.21	0.026	0.054
1-3	7.7	4.21	0.018	0.042
1-4	10.0	4.21	0.022	0.056
1-5	13.0	4.21	0.013	0.039
1-6	16.3	4.21	0.011	0.036
1-7	19.2	4.21	0.010	0.044
1-8	17.8	4.21	0.011	0.039
1-9	15.2	4.16	0.012	0.036
1-10	11.6	4.16	0.016	0.052
1-11	9.2	4.16	0.019	0.048
1-12	6.4	4.16	0.020	0.046
1-13	4.2	4.16	0.029	0.062
1-14	3.6	4.16	0.031	0.070

*The run number is followed by a coordination number which is used to identify data as recorded on magnetic tape.

TABLE 1 (Cont'd)

Run	f (CPS)	q (psf)	e _A (VRMS) x 10 ²	$2 \frac{\hat{v}}{V}$
2-1	3.6	2.34	0.0130	0.044
2-2	6.0	2.34	0.0100	0.032
2-3	8.8	2.34	0.0084	0.031
2-4	11.2	2.34	0.0090	0.034
2-5	13.3	2.34	0.0068	0.026
2-6	15.0	2.34	0.0068	0.025
2-7	16.9	2.34	0.0064	0.075
2-8	19.1	2.34	0.0064	0.029
2-9	18.1	2.34	0.0060	0.027
2-10	15.9	2.34	0.0065	0.025
2-11	14.1	2.34	0.0066	0.025
2-12	10.1	2.34	0.0099	0.039
2-13	7.0	2.34	0.0090	0.028
2-14	5.0	2.34	0.0110	0.034
2-15	4.2	2.34	0.0120	0.038

TABLE 1 (Cont'd)

Run	f	q	e _A	$2 \frac{\hat{v}}{V}$
	(CPS)	(psf)	(VRMS) $\times 10^2$	
3-1	3.6	7.60	0.077	0.087
3-2	5.8	7.60	0.050	0.064
3-3	8.6	7.55	0.037	0.056
3-4	11.1	7.55	0.047	0.070
3-5	13.6	7.55	0.026	0.054
3-6	17.4	7.55	0.017	0.058
3-7	19.2	7.60	0.018	0.078
3-8	15.7	7.60	0.019	0.054
3-9	12.4	7.55	0.033	0.058
3-10	9.7	7.55	0.050	0.076
3-11	7.0	7.55	0.043	0.056
3-12	4.8	7.60	0.060	0.078
3-13	4.2	7.55	0.070	0.078

TABLE 1 (Cont'd)

Run	f (CPS)	q (psf)	e _A (VRMS) x 10 ²	$2 \frac{\hat{v}}{v}$
4-1	3.6	5.98	0.055	0.0594
4-2	5.1	5.98	0.043	0.0458
4-3	7.9	5.92	0.030	0.0344
4-4	10.1	5.92	0.040	0.0504
4-5	12.0	5.92	0.030	0.0412
4-6	14.0	5.92	0.019	0.0322
4-7	17.0	5.88	0.016	0.0300
4-8	19.3	5.98	0.016	0.0346
4-9	15.6	5.92	0.017	0.0298
4-10	13.1	5.92	0.021	0.0344
4-11	9.1	5.92	0.034	0.0392
4-12	6.6	5.92	0.033	0.0390
4-12	4.6	5.98	0.046	0.0504
4-14	4.0	5.98	0.050	0.0574

TABLE 1 (Cont'd)

Run	f (CPS)	q (psf)	e _A (VRMS) x 10 ²	$2 \frac{\hat{V}}{V}$
10-1	3.6	0.99	0.0039	0.0288
10-2	5.5	0.99	0.0037	0.0266
10-3	7.4	0.99	0.0038	0.0266
10-4	9.7	0.99	0.0041	0.0308
10-5	12.3	0.99	0.0039	0.0236
10-6	14.5	0.99	0.0030	0.0206
10-7	16.7	0.99	0.0035	0.0194
10-8	19.2	0.99	0.0032	0.0184
10-9	17.6	0.99	0.0032	0.0190
10-10	13.3	0.99	0.0036	0.0224
10-11	10.9	0.99	0.0039	0.0288
10-12	8.4	0.99	0.0038	0.0266
10-13	6.3	0.99	0.0037	0.0266
10-14	4.3	0.99	0.0039	0.0288

TABLE 2
REDUCED DATA: MEDIUM VANES

Run*	f (CPS)	q (psf)	e _A (VRMS) x 10 ²	$2 \frac{\Delta v}{V}$
11-1	3.7	1.56	0.048	0.282
11-2	6.4	1.45	0.033	0.228
11-3	8.6	1.40	0.037	0.216
11-4	11.2	1.45	0.036	0.228
11-5	13.1	1.40	0.032	0.179
11-6	15.5	1.35	0.033	0.202
11-7	18.2	1.40	0.033	0.190
11-8	19.3	1.51	0.029	0.166
11-9	16.8	1.35	0.033	0.212
11-10	14.2	1.35	0.033	0.184
11-11	9.7	1.40	0.040	0.278
11-12	7.7	1.40	0.030	0.222
11-13	5.3	1.45	0.036	0.276
11-14	4.4	1.51	0.043	0.278

*The run number is followed by a coordination number which is used to identify data as recorded on magnetic tape.

TABLE 2 (Cont'd)

Run	f (CPS)	q (psf)	e _A (VRMS) x 10 ²	$2 \frac{\Delta V}{V}$
12-1	3.7	2.49	0.090	0.346
12-2	5.6	2.29	0.063	0.332
12-3	8.1	2.13	0.047	0.250
12-4	10.9	2.24	0.060	0.274
12-5	13.1	2.13	0.047	0.218
12-6	15.5	2.03	0.053	0.256
12-7	18.5	2.03	0.050	0.256
12-8	19.2	2.39	0.048	0.206
12-9	17.2	2.08	0.050	0.252
12-10	14.1	2.08	0.048	0.222
12-11	12.0	2.18	0.050	0.246
12-12	9.3	2.18	0.057	0.298
12-13	6.8	2.18	0.050	0.268
12-14	4.8	2.34	0.077	0.336

TABLE 2 (Cont'd)

Run	f (CPS)	q (psf)	e _A (VRMS) x 10 ²	$2 \frac{\hat{v}}{v}$
13-1	3.6	2.96	0.120	0.388
13-2	5.6	2.65	0.077	0.376
13-3	8.8	2.44	0.053	0.276
13-4	12.0	2.65	0.077	0.332
13-5	15.4	2.44	0.053	0.240
13-6	18.2	2.39	0.060	0.290
13-7	19.1	2.86	0.055	0.230
13-8	16.9	2.34	0.060	0.282
13-9	13.8	2.49	0.057	0.266
13-10	10.8	2.65	0.080	0.342
13-11	9.4	2.49	0.063	0.294
13-12	7.7	2.44	0.053	0.262
13-13	6.6	2.54	0.060	0.290
13-14	4.5	2.70	0.100	0.375

TABLE 2 (Cont'd)

Run	f (CPS)	q (psf)	e _A (VRMS) x 10 ²	$2 \frac{\hat{v}}{V}$
14-1	3.6	0.73	0.015	0.204
14-2	5.8	0.73	0.017	0.204
14-3	8.3	0.73	0.016	0.181
14-4	11.3	0.68	0.022	0.219
14-5	14.1	0.68	0.016	0.142
14-6	16.6	0.68	0.017	0.156
14-7	20.5	0.68	0.015	0.134
14-8	18.3	0.68	0.016	0.148
14-9	15.2	0.73	0.017	0.142
14-10	12.7	0.73	0.018	0.158
14-11	9.7	0.73	0.017	0.188
14-12	7.2	0.73	0.016	0.188
14-13	6.2	0.73	0.017	0.204
14-14	5.3	0.73	0.016	0.204
14-15	4.2	0.73	0.016	0.220

TABLE 2 (Cont'd)

Run	f (CPS)	q (psf)	e _A (VRMS) x 10 ²	$2 \frac{\hat{V}}{V}$
15-1	3.6	3.28	0.140	0.428
15-2	6.2	2.91	0.090	0.378
15-3	9.9	2.70	0.598	0.246
15-4	12.5	2.86	0.080	0.316
15-5	15.1	2.76	0.060	0.256
15-6	17.2	2.54	0.070	0.294
15-7	20.8	3.28	0.058	0.232
15-8	18.5	2.60	0.070	0.292
15-9	16.2	2.60	0.066	0.264
15-10	13.8	2.76	0.063	0.272
15-11	11.3	2.96	0.090	0.336
15-12	8.8	2.65	0.053	0.258
15-13	7.5	2.76	0.066	0.298
15-14	4.9	3.01	0.120	0.390

TABLE 3
REDUCED DATA: LARGE VANES

Run*	f (CPS)	q (psf)	e _A (VRMS) x 10 ²	$2 \frac{\hat{v}}{v}$
5-1	3.7	2.29	0.150	1.084
5-2	5.6	2.08	0.120	0.978
5-3	7.8	1.40	0.080	0.922
5-4	10.0	1.71	0.110	0.894
5-5	12.5	1.56	0.100	0.876
5-6	14.3	1.45	0.100	0.776
5-7	17.0	1.04	0.120	1.072
5-8	19.3	2.08	0.093	0.704
5-9	16.0	1.04	0.120	0.960
5-10	13.0	1.56	0.090	0.876
5-11	9.3	1.45	0.079	0.776
5-12	6.6	1.66	0.170	0.910
5-13	4.7	1.77	0.130	1.118
5-14	3.6	2.24	0.150	1.108

*The run number is followed by a coordination number which is used to identify data as recorded on magnetic tape.

TABLE 3 (Cont'd)

Run	f (CPS)	q (psf)	e _A (VRMS) x 10 ²	$2 \frac{\Delta v}{v}$
6-1	3.6	1.97	0.145	1.040
6-2	5.2	1.56	0.120	1.186
6-3	7.5	1.40	0.077	0.870
6-4	10.0	1.51	0.100	0.842
6-5	12.4	1.48	0.101	0.908
6-6	14.6	1.30	0.110	0.906
6-7	16.8	1.04	0.120	1.138
6-8	19.4	1.77	0.090	0.584
6-9	15.2	1.20	0.108	1.004
6-10	13.6	1.40	0.090	0.816
6-11	11.3	1.56	0.110	0.928
6-12	8.3	1.25	0.082	0.982
6-13	6.5	1.56	0.090	1.032
6-14	4.4	1.66	0.120	1.200

TABLE 3 (Cont'd)

Run	f (CPS)	q (psf)	e _A (VRMS) x 10 ²	$2 \frac{\Delta V}{V}$
7-1	3.7	1.92	0.130	0.924
7-2	6.4	1.56	0.100	1.076
7-3	8.6	1.25	0.077	0.850
7-4	10.3	1.30	0.083	0.784
7-5	13.0	1.14	0.097	0.766
7-6	15.6	1.20	0.097	0.766
7-7	17.7	1.04	0.110	0.986
7-8	21.0	1.14	0.083	0.626
7-9	16.2	1.04	0.110	0.876
7-10	14.2	1.35	0.083	0.672
7-11	11.5	1.45	0.100	0.832
7-12	9.3	1.14	0.081	0.784
7-13	7.5	1.35	0.077	0.816
7-14	5.1	1.45	0.110	1.062

TABLE 3 (Cont'd)

Run	f (CPS)	q (psf)	e _A (VRMS) x 10 ²	$2 \frac{\Delta V}{V}$
8-1	4.0	1.61	0.109	0.864
8-2	6.5	1.40	0.087	0.922
8-3	8.4	1.19	0.066	0.708
8-4	10.6	1.14	0.083	0.724
8-5	13.2	1.25	0.083	0.652
8-6	16.0	1.14	0.083	0.638
8-7	21.0	1.30	0.077	0.480
8-8	18.3	1.46	0.110	0.874
8-9	14.1	1.14	0.077	0.596
8-10	12.3	1.30	0.090	0.720
8-11	9.5	1.14	0.073	0.682
8-12	7.5	1.25	0.070	0.734
8-13	5.2	1.30	0.090	0.920

TABLE 3 (Cont'd)

Run	f (CPS)	q (psf)	e _A (VRMS) x 10 ²	$2 \frac{\hat{v}}{V}$
9-1	3.6	0.68	0.047	0.670
9-2	6.1	0.62	0.050	0.618
9-3	9.6	0.57	0.063	0.702
9-4	11.8	0.62	0.043	0.412
9-5	14.7	0.52	0.066	0.622
9-6	18.1	0.47	0.073	0.674
9-7	20.9	0.52	0.044	0.424
9-8	16.7	0.47	0.059	0.626
9-9	13.4	0.62	0.039	0.388
9-10	10.6	0.62	0.060	0.644
9-11	8.5	0.57	0.043	0.540
9-12	7.3	0.62	0.047	0.594
9-13	5.5	0.68	0.050	0.670
9-14	4.4	0.68	0.043	0.670

TABLE 4

Experimental Phase Difference Between
Anemometer and Hot Wire
Small Vanes

q = 4.19 psf

q = 2.34 psf

Run	f (CPS)	ϕ (degrees)	Run	f (CPS)	ϕ (degrees)
1-1	3.6	7	2-1	3.6	7
1-2	5.0	12	2-2	6.0	13
1-3	7.7	15	2-3	8.8	21
1-4	10.0	20	2-4	11.2	12
1-5	13.0	17	2-5	13.3	22
1-6	16.3	22	2-6	15.0	24
1-7	19.2	27	2-7	16.9	24
1-8	17.8	22	2-8	19.1	27
1-9	15.2	23	2-9	18.1	29
1-10	11.6	18	2-10	15.9	28
1-11	9.2	16	2-11	14.1	22
1-12	6.4	12	2-12	10.1	12
1-13	4.2	9	2-13	7.0	13
1-14	3.6	6	2-14	5.0	12

TABLE 4 (Cont'd)

q = 7.55 psf

q = 5.90 psf

Run	f (CPS)	ϕ (degrees)	Run	f (CPS)	ϕ (degrees)
3-1	3.6	11	4-1	3.6	3
3-2	5.8	15	4-2	5.1	7
3-3	8.6	21	4-3	7.9	8
3-4	11.1	29	4-4	10.1	10
3-5	13.6	32	4-5	12.0	18
3-6	17.4	36	4-6	14.0	17
3-7	19.2	32	4-7	17.0	21
3-8	15.7	37	4-8	19.3	15
3-9	12.4	32	4-9	15.6	21
3-10	9.7	23	4-10	13.1	19
3-11	7.0	20	4-11	9.1	9
3-12	4.8	15	4-12	6.6	8
3-13	4.2	13	4-13	4.6	4
			4-14	4.0	4

TABLE 4 (Cont'd)

 $q = 1.00$ psf

Run	f (CPS)	ϕ (degrees)
10-1	3.6	23
10-2	5.5	29
10-3	7.4	33
10-4	9.7	29
10-5	12.3	36
10-6	14.5	38
10-7	16.7	49
10-8	19.2	56
10-9	17.6	48
10-10	13.3	37
10-11	10.9	34
10-12	8.4	30
10-13	6.3	29
10-14	4.3	26

TABLE 5

Experimental Phase Difference Between

Anemometer and Hot Wire

Medium Vanes

 $q = 1.43$ psf $q = 2.23$ psf

Run	f (CPS)	ϕ (degrees)	Run	f (CPS)	ϕ (degrees)
11-1	3.7	1	12-1	3.7	1
11-2	6.4	3	12-2	5.6	2
11-3	8.6	3	12-3	8.1	2
11-4	11.2	1	12-4	10.9	0
11-5	13.1	11	12-5	13.1	5
11-6	15.5	46	12-6	15.5	40
11-7	18.2	30	12-7	18.5	23
11-8	19.3	27	12-8	19.2	24
11-9	16.8	30	12-9	17.2	22
11-10	14.2	37	12-10	14.1	23
11-11	9.7	1	12-11	12.0	0
11-12	7.7	0	12-12	9.3	0
11-13	5.3	3	12-13	6.8	0
11-14	4.4	0	12-14	4.8	0

TABLE 5 (Cont'd)

q = 2.56 psf

q = 0.71 psf

Run	f (CPS)	ϕ (degrees)	Run	f (CPS)	ϕ (degrees)
13-1	3.6	1	14-1	3.6	16
13-2	5.6	3	14-2	5.8	15
13-3	8.8	0	14-3	8.3	7
13-4	12.0	0	14-4	11.3	8
13-5	15.4	18	14-5	14.1	20
13-6	18.2	28	14-6	16.6	42
13-7	19.1	22	14-7	20.5	34
13-8	16.9	36	14-8	18.3	27
13-9	13.8	0	14-9	15.2	44
13-10	10.5	0	14-10	12.7	2
13-11	9.4	0	14-11	9.7	21
13-12	7.7	1	14-12	7.2	12
13-13	6.6	0	14-13	6.2	13
13-14	4.5	1	14-14	5.3	15
			14-15	4.2	14

TABLE 5 (Cont'd)

q = 2.85 psf

Run	f (CPS)	ϕ (degrees)
15-1	3.6	1
15-2	6.2	2
15-3	9.9	0
15-4	12.5	0
15-5	15.1	4
15-6	17.2	40
15-7	20.8	20
15-8	18.5	27
15-9	16.2	33
15-10	13.8	0
15-11	11.3	0
15-12	8.8	1
15-13	7.5	0
15-14	4.9	0

TABLE 6
COMPARISON OF FOURIER COMPONENTS

Run	S (x 10 ²)	Signal	Fundamental	2nd Harmonic		3rd Harmonic	
			ϕ_1 (degrees)	A_2/A_1 (%)	ϕ_2 (degrees)	A_3/A_1 (%)	ϕ_3 (degrees)
1-1	3.47	e_H	-	19.7	-	4.4	-
		e_A	-2.0	8.5	-13	10.7	47
1-2	4.83	e_H	-	28.7	-	3.4	-
		e_A	7.3	30.8	56	2.8	23
1-2*	4.83	e_H	-	30.5	-	6.0	-
		e_A	7.5	24.6	20	9.4	-69
1-3	7.45	e_H	-	27.4	-	2.1	-
		e_A	14.0	8.1	5	6.4	139
1-4	9.69	e_H	-	10.0	-	2.8	-
		e_A	7.0	9.0	-104	1.6	162

Note:

1. $\phi()$ is phase difference between hot wire and anemometer signal for component in subscripts (positive for hot wire leading anemometer).
2. $\frac{A()}{A()}$ indicates amplitude ratio of components in subscripts for specified signal, i.e., e_H or e_A .
- * indicates different waveform sample in run.

TABLE 6 (Cont'd)

Run	S ($\times 10^2$)	Signal	Fundamental	2nd Harmonic		3rd Harmonic	
			ϕ_1 (degrees)	A_2/A_1 (%)	ϕ_2 (degrees)	A_3/A_1 (%)	ϕ_3 (degrees)
2-1	4.69	e _H	-	20.9	-	1.1	-
		e _A	4	16.6	10	8.3	56
2-14	6.15	e _H	-	27.2	-	4.8	-
		e _A	14	21.3	-13	9.4	46
2-13	8.51	e _H	-	23.4	-	2.8	-
		e _A	28	8.4	50	9.4	5
2-12	12.25	e _H	-	26.5	-	4.4	-
		e _A	0.2	8.8	57	7.8	-16
2-4	14.55	e _H	-	16.7	-	2.8	-
		e _A	9	15.7	-27	1.6	45
2-4*	14.55	e _H	-	16.2	-	5.1	-
		e _A	4	16.3	25	1.1	-25
2-11	18.4	e _H	-	24.5	-	4.3	-
		e _A	12	35.3	1	2.3	-14

TABLE 7

REDUCED DATA: SMALL VANES

Run	f (CPS)	q (psf)	e _A (VRMS) x 10 ²	$2 \frac{\hat{v}}{V}$
16-1	3.6	4.32	0.0310	0.0723
16-2	5.4	4.26	0.0240	0.0562
16-3	7.0	4.26	0.0200	0.0474
16-4	8.4	4.26	0.0170	0.0444
16-5	9.4	4.26	0.0180	0.0526
16-6	10.8	4.26	0.0200	0.0621
16-7	11.9	4.26	0.0140	0.0503
16-8	13.6	4.26	0.0104	0.0416
16-9	14.2	4.26	0.0104	0.0397
16-10	15.6	4.26	0.0104	0.0387
16-11	16.6	4.26	0.0096	0.0387
16-12	17.7	4.26	0.0097	0.0399
16-13	19.1	4.26	0.0095	0.0444
16-14	18.3	4.26	0.0096	0.0411
16-15	16.3	4.26	0.0099	0.0387
16-16	13.7	4.26	0.0104	0.0406
16-17	11.7	4.26	0.0148	0.0511
16-18	9.3	4.26	0.0191	0.0515
16-19	7.4	4.26	0.0180	0.0454
16-20	6.1	4.26	0.0212	0.0507

TABLE 7 (Cont'd)

Run	f (CPS)	q (psf)	e _A (VRMS) x 10 ²	$2 \frac{\hat{v}}{V}$
17-1	3.6	6.03	0.0524	0.0793
17-2	5.3	5.98	0.0392	0.0609
17-3	6.8	5.98	0.0320	0.0507
17-4	8.1	5.98	0.0279	0.0473
17-5	9.5	5.98	0.0341	0.0588
17-6	10.4	5.98	0.0382	0.0684
17-7	12.0	5.98	0.0247	0.0527
17-8	13.1	5.98	0.0183	0.0456
17-9	14.2	5.98	0.0150	0.0429
17-10	15.7	5.92	0.0139	0.0411
17-11	18.5	5.98	0.0139	0.0470
17-12	19.1	5.98	0.0139	0.0489
17-13	18.0	5.98	0.0139	0.0454
17-14	16.6	5.92	0.0139	0.0428
17-15	13.2	5.98	0.0183	0.0451
17-16	11.0	5.98	0.0341	0.0647
17-17	9.0	5.98	0.0299	0.0533
17-18	7.0	5.98	0.0310	0.0505

TABLE 7 (Cont'd)

Run	f (CPS)	q (psf)	e _A (VRMS) x 10 ²	$2 \frac{\hat{v}}{v}$
18-1	3.6	7.60	0.0784	0.0836
18-2	6.4	7.53	0.0469	0.0562
18-3	6.8	7.53	0.0428	0.0540
18-4	8.1	7.51	0.0398	0.0499
18-5	8.4	7.51	0.0377	0.0507
18-6	9.3	7.53	0.0449	0.0584
18-7	10.7	7.53	0.0531	0.0709
18-8	11.4	7.48	0.0459	0.0640
18-9	12.2	7.48	0.0346	0.0546
18-10	12.8	7.48	0.0314	0.0499
18-11	13.1	7.48	0.0293	0.0491
18-12	14.0	7.53	0.0251	0.0454
18-13	15.7	7.48	0.0173	0.0449
18-14	17.2	7.48	0.0162	0.0465
18-15	19.1	7.60	0.0173	0.0554
18-16	18.3	7.53	0.0162	0.0502
18-17	15.5	7.48	0.0173	0.0445
18-18	13.7	7.48	0.0251	0.0463
18-19	11.1	7.48	0.0490	0.0669
18-20	8.3	7.48	0.0387	0.0497

TABLE 8
REDUCED DATA: MEDIUM VANES

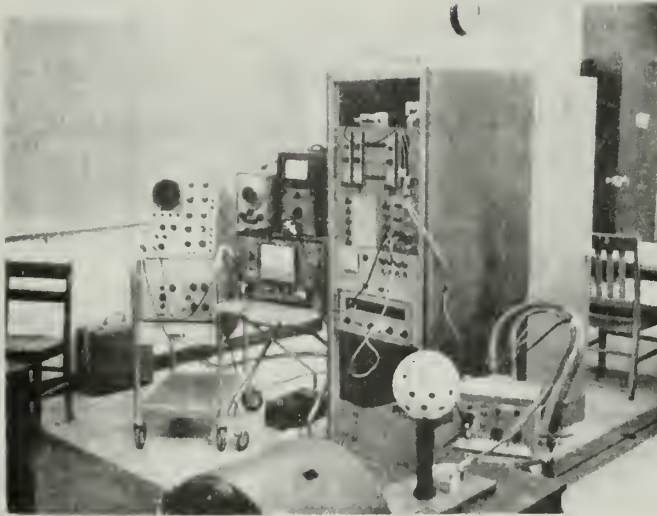
Run	f (CPS)	q (psf)	e _A (VRMS) x 10 ²	2 $\frac{\hat{v}}{V}$
19-1	3.6	2.34	0.084	0.370
19-2	5.5	2.18	0.058	0.326
19-3	7.1	2.08	0.043	0.238
19-4	8.6	2.05	0.041	0.230
19-5	9.6	2.08	0.052	0.266
19-6	11.3	2.13	0.055	0.290
19-7	12.7	2.08	0.044	0.222
19-8	14.2	2.03	0.046	0.216
19-9	15.8	1.98	0.050	0.246
19-10	17.6	2.08	0.046	0.236
19-11	19.1	2.34	0.040	0.206
19-12	18.0	2.13	0.046	0.232
19-13	17.2	2.03	0.047	0.238
19-14	15.2	1.98	0.049	0.236
19-15	13.8	2.08	0.044	0.214
19-16	13.0	2.08	0.043	0.216
19-17	11.9	2.08	0.048	0.248
19-18	10.6	2.18	0.060	0.312
19-19	7.8	2.03	0.040	0.226

TABLE 8 (Cont'd)

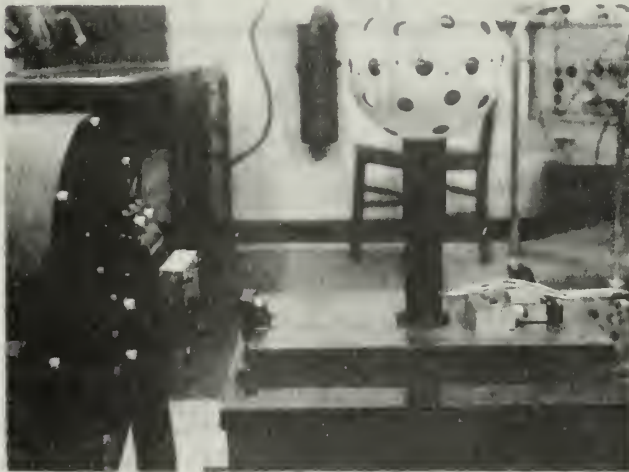
Run	f (CPS)	q (psf)	e _A (VRMS) x 10 ²	$2 \frac{\hat{v}}{V}$
20-1	3.6	3.33	0.138	0.440
20-2	6.9	2.83	0.064	0.270
20-3	7.7	2.70	0.056	0.248
20-4	9.0	2.81	0.057	0.240
20-5	10.6	3.02	0.091	0.352
20-6	12.5	2.86	0.062	0.258
20-7	13.5	2.83	0.057	0.236
20-8	15.0	2.70	0.065	0.254
20-9	16.4	2.70	0.066	0.276
20-10	18.4	3.17	0.061	0.258
20-11	19.0	3.54	0.057	0.238
20-12	17.7	2.91	0.064	0.270
20-13	14.1	2.81	0.059	0.234
20-14	11.6	2.86	0.072	0.300
20-15	8.0	2.70	0.054	0.238

FIG. 1
INERTIAL RESPONSE TEST SET-UP

(A) Inertial Test Set



(B) Shaker Mount



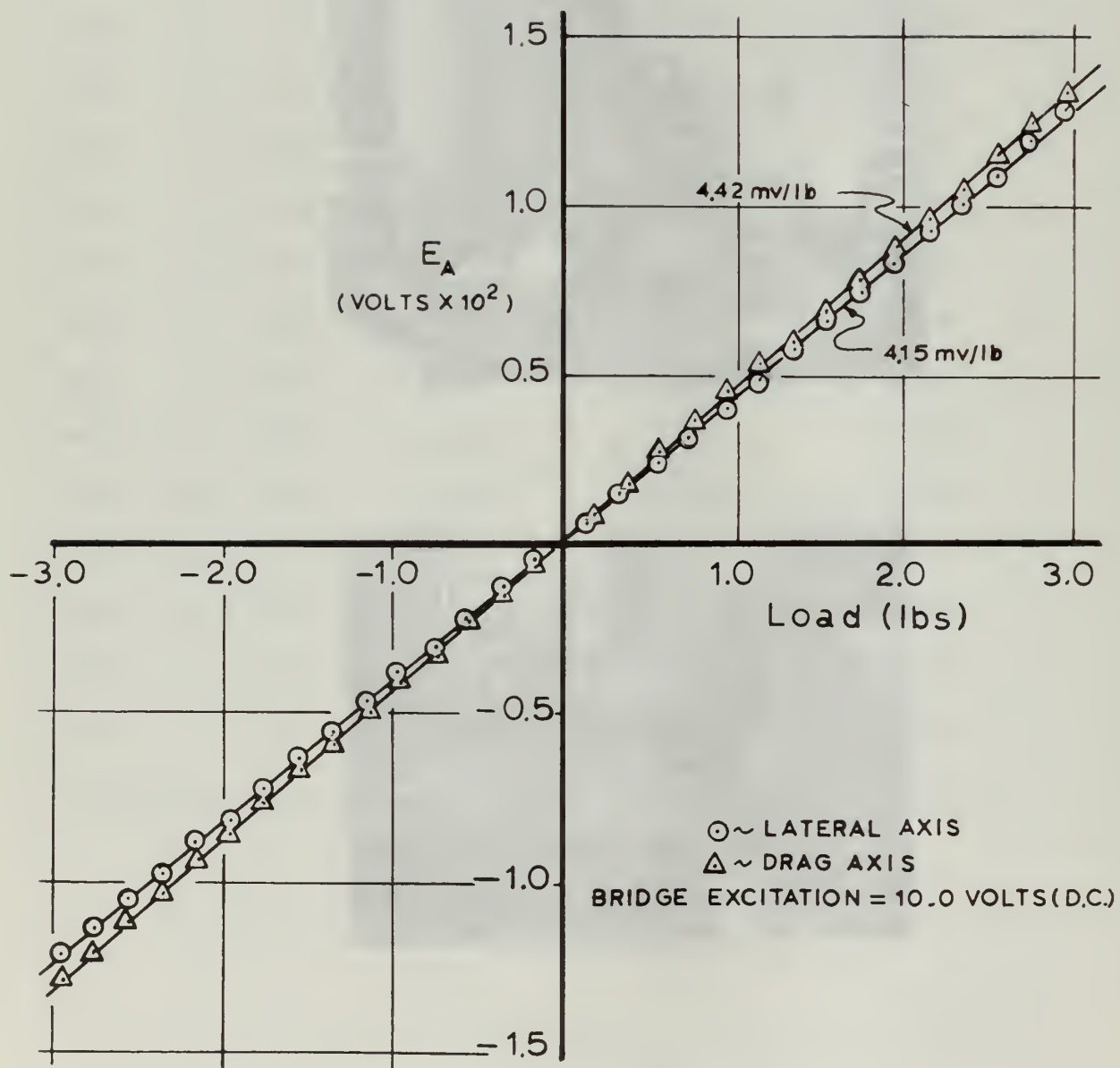


FIG. 2: ANEMOMETER STATIC CALIBRATION

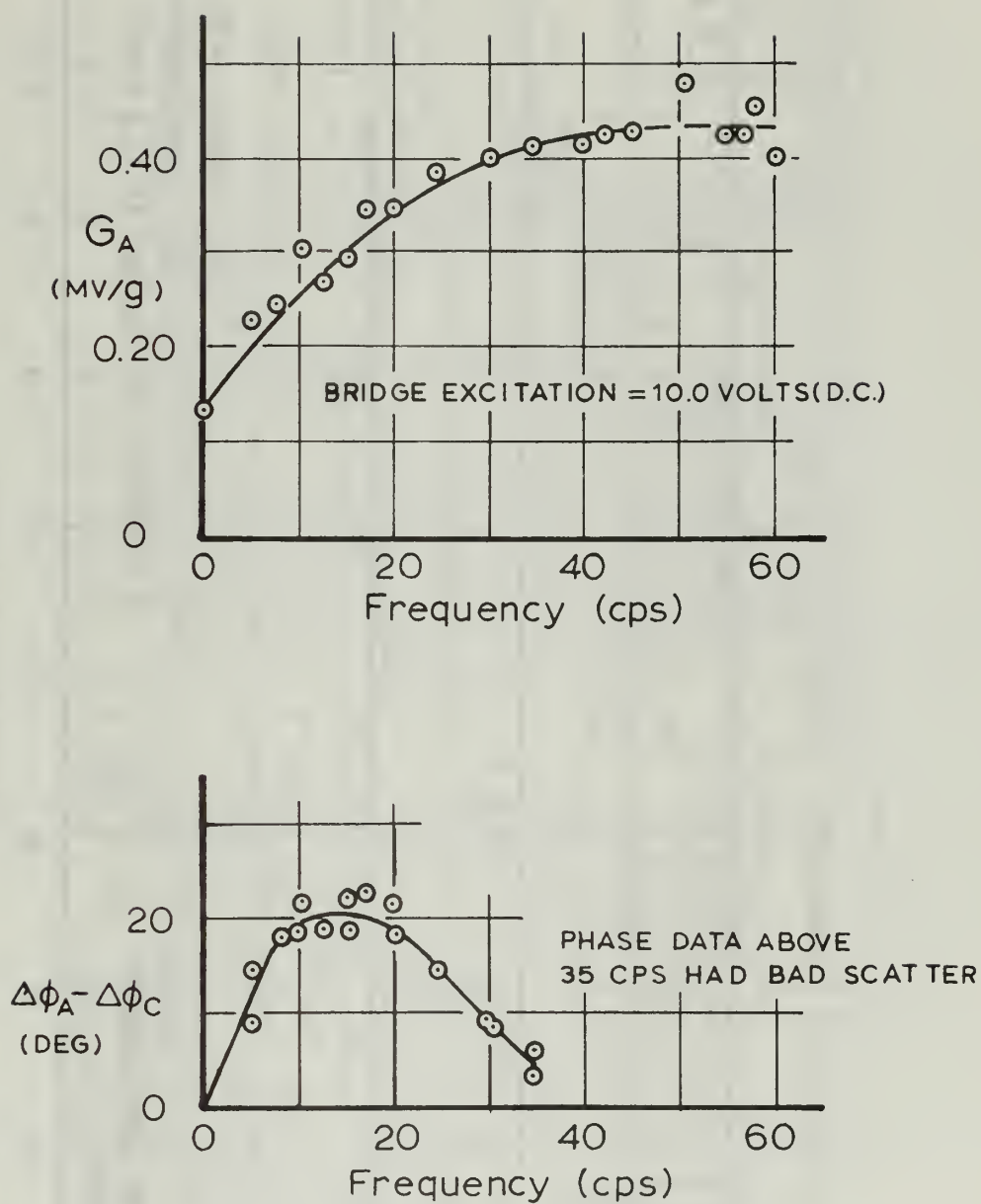


FIG. 3: ANEMOMETER INERTIAL RESPONSE

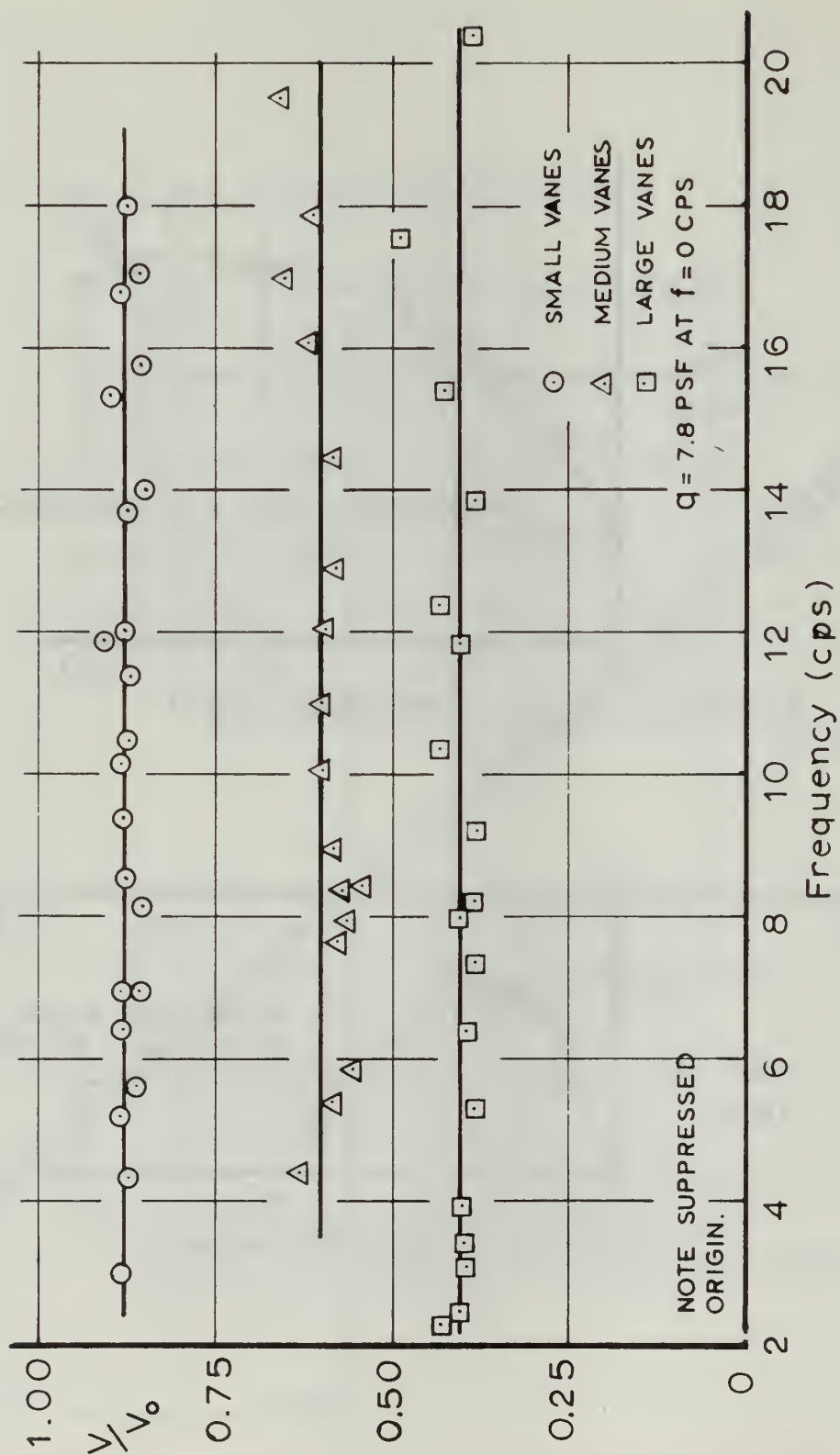


FIG. 4: SHUTTER VANE BLOCKAGE

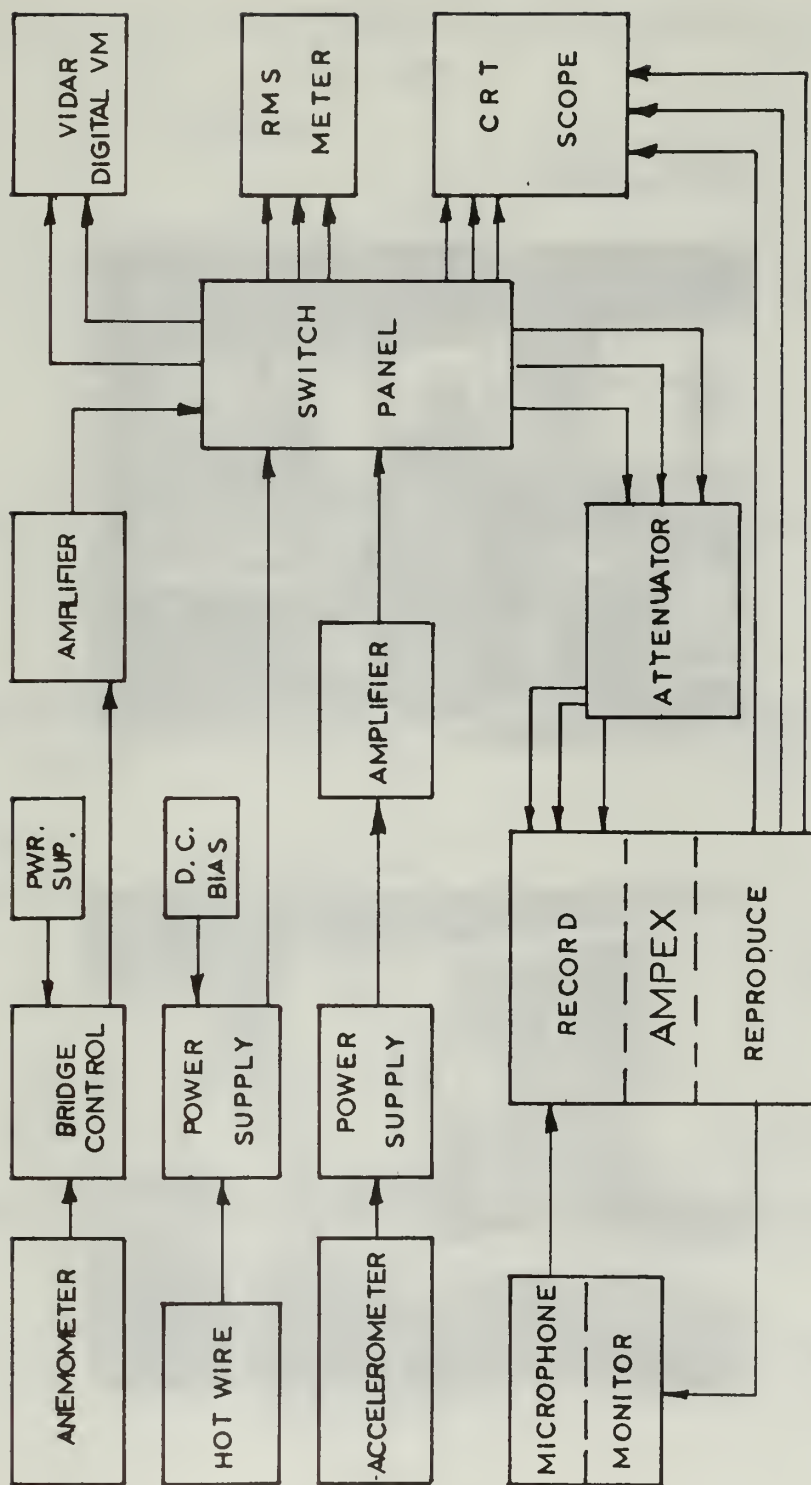
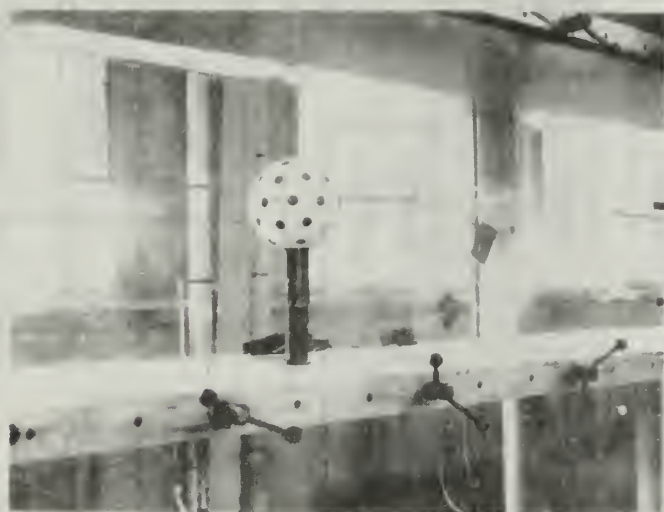


FIG.5: DIAGRAM OF DATA ACQUISITION SYSTEM



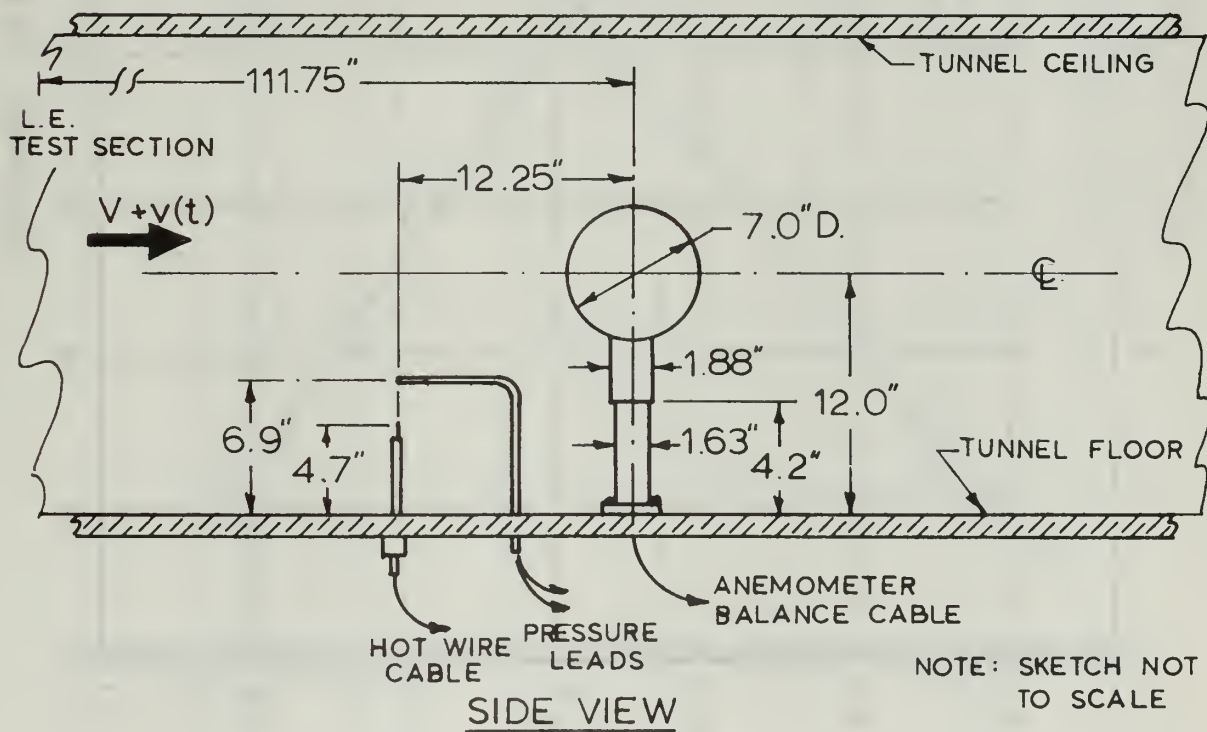
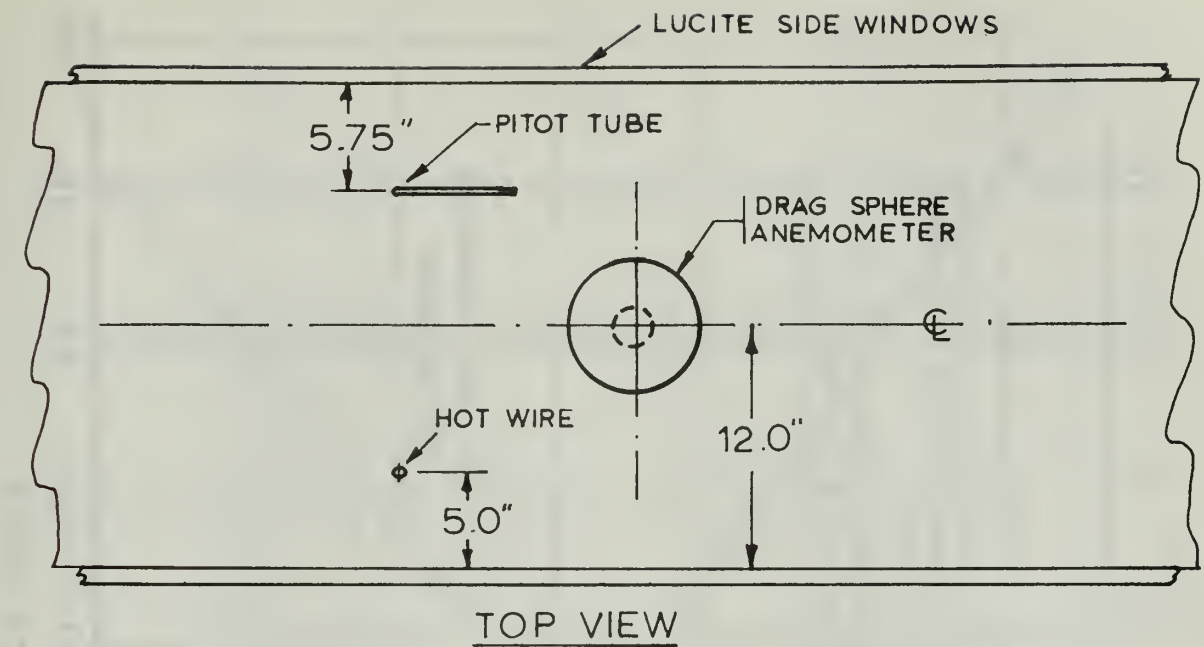


FIG.7: SENSOR INSTALLATION DETAILS

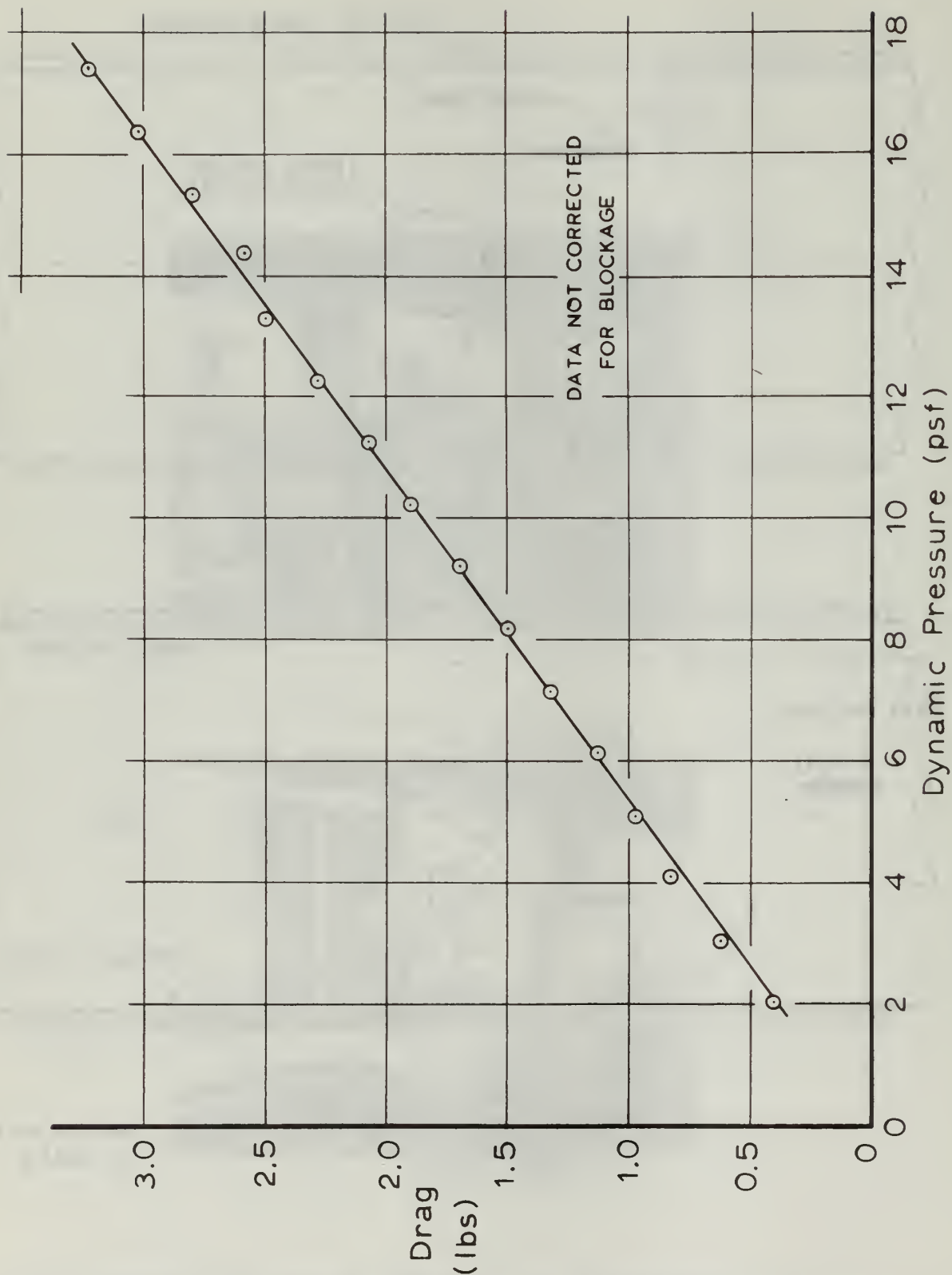


FIG. 8: ANEMOMETER DRAG vs. DYNAMIC PRESSURE (W.C.R. TUNNEL)

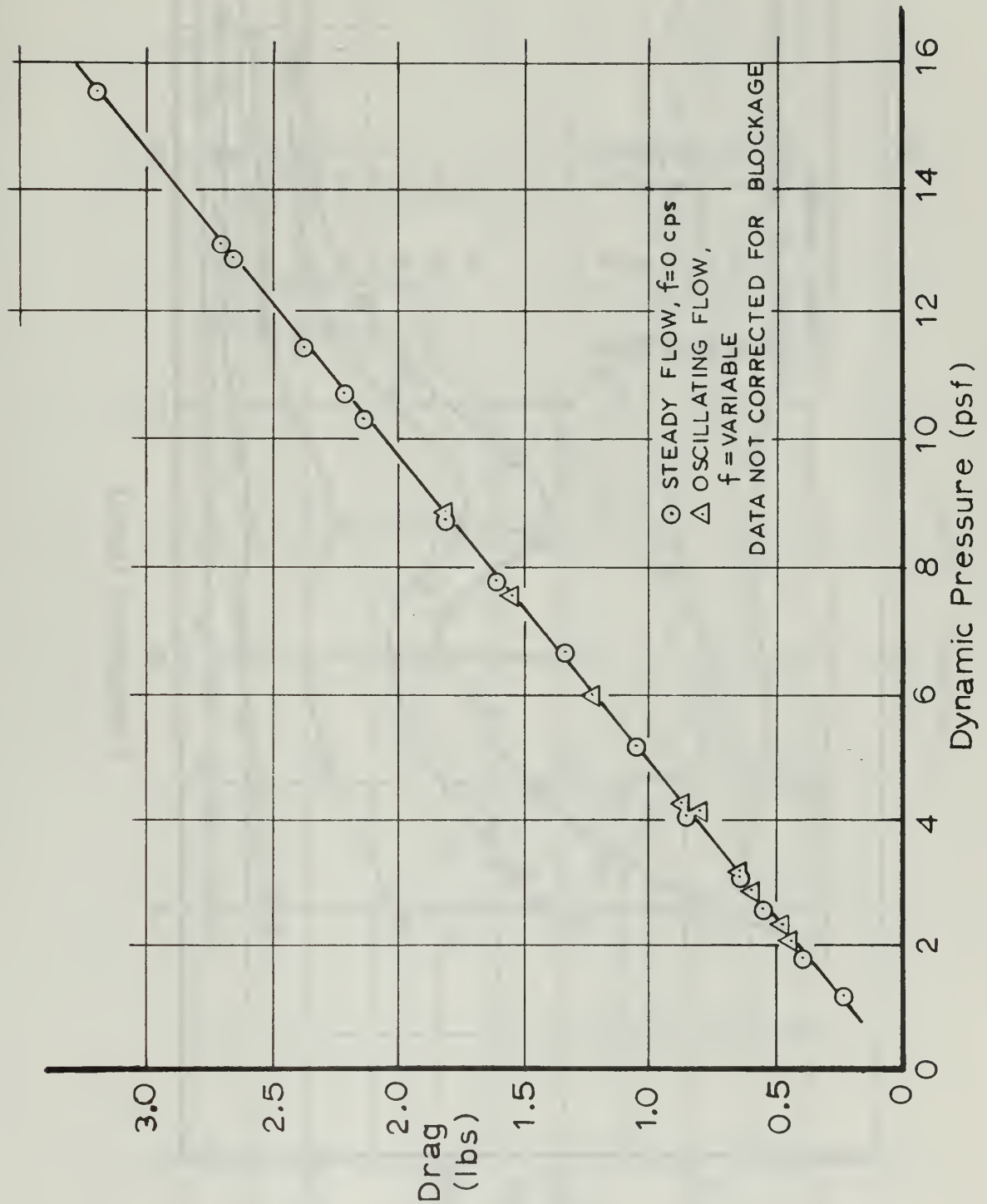


FIG. 9: MEAN ANEMOMETER DRAG vs. MEAN DYNAMIC PRESSURE (NONSTEADY TUNNEL)

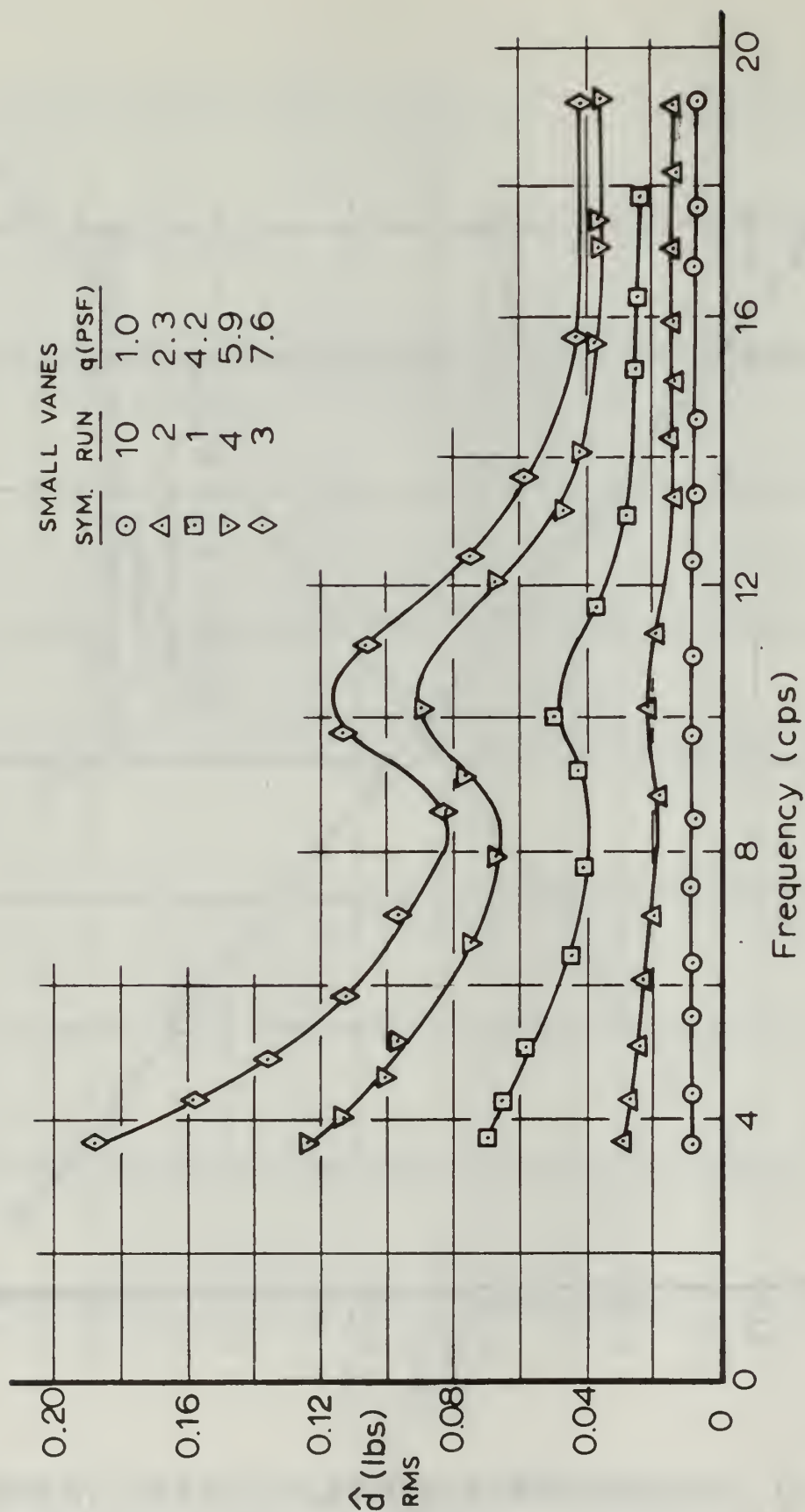


FIG.10: UNSTEADY DRAG vs. FREQUENCY
(SMALL VANES)

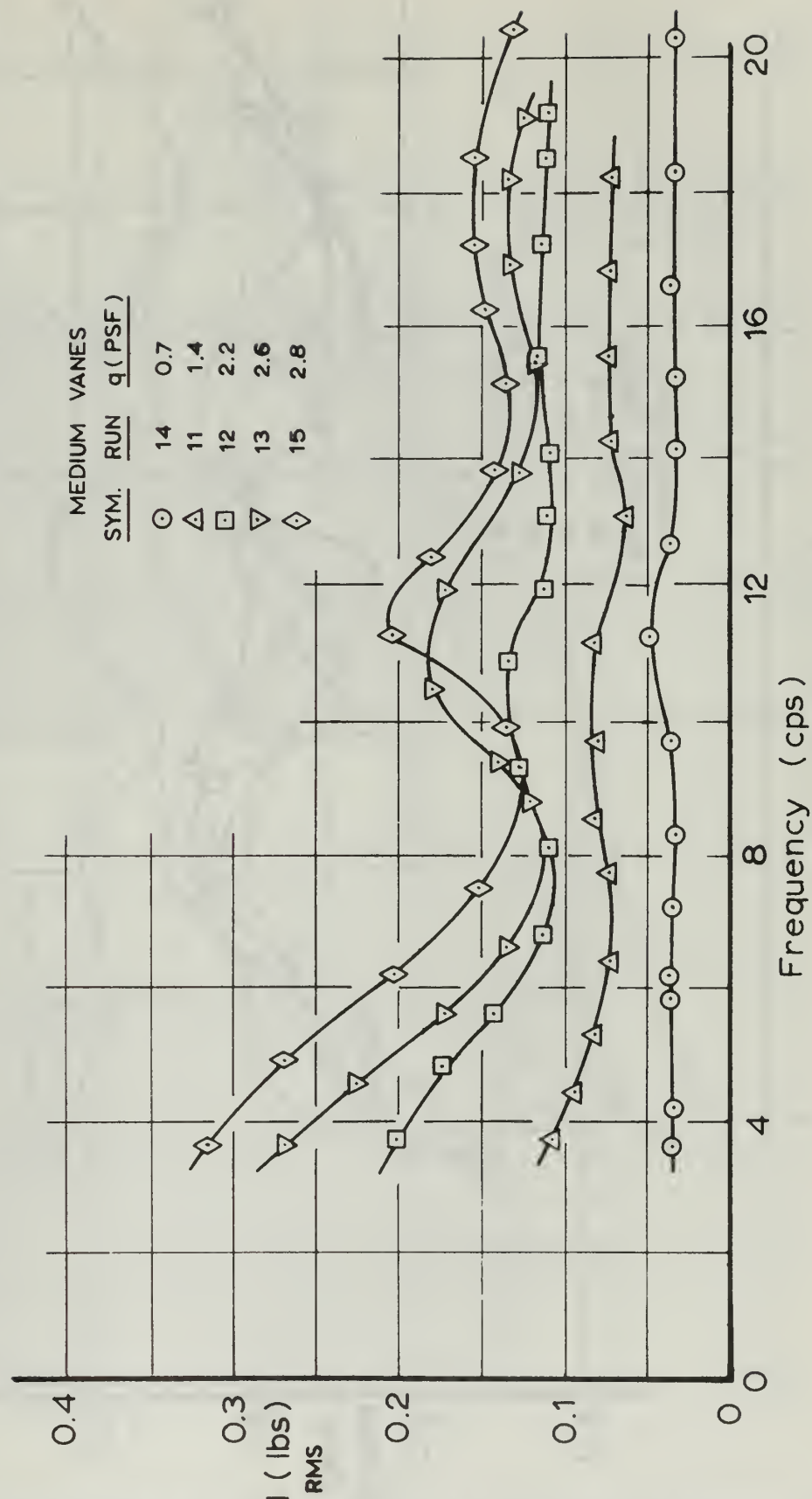


FIG.11: UNSTEADY DRAG vs. FREQUENCY
(MEDIUM VANES)

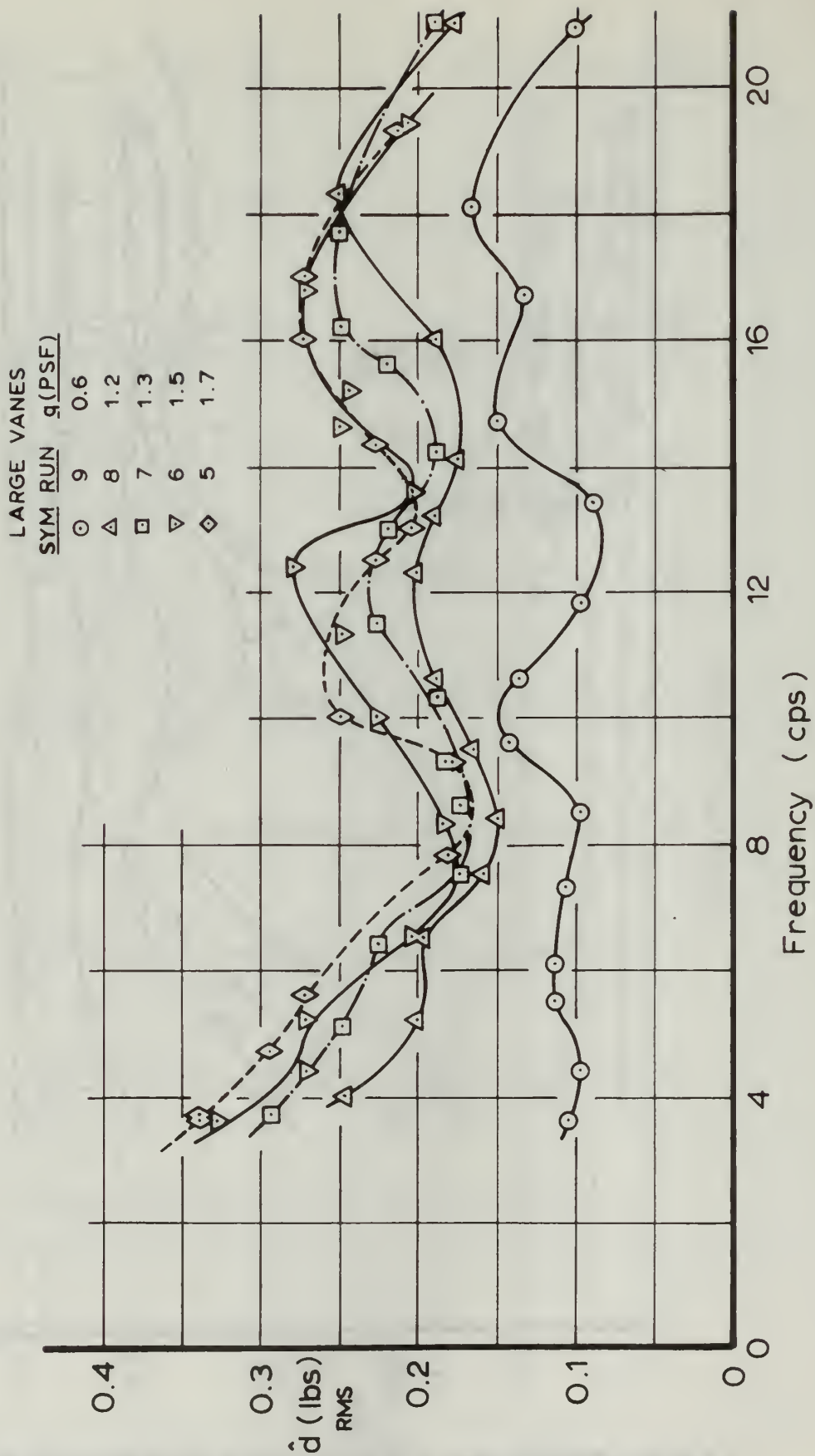


FIG.12: UNSTEADY \dot{d} (lbs) vs. FREQUENCY (LARGE VANES)

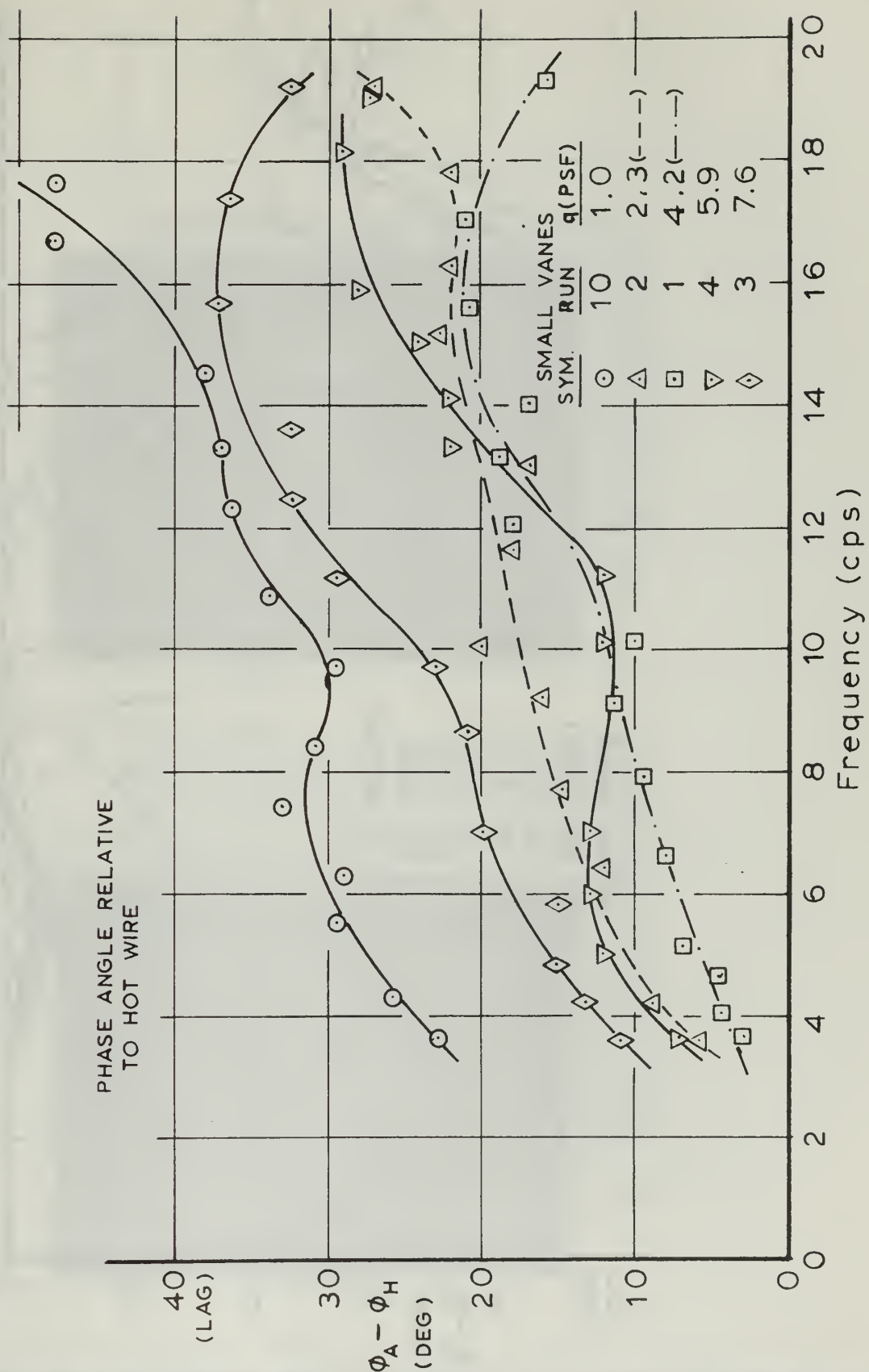


FIG.13: ANEMOMETER PHASE LAG (SMALL VANES)



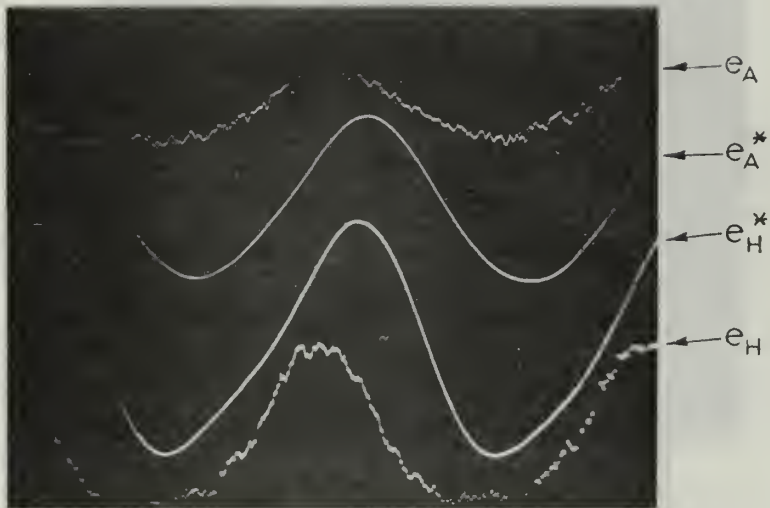
FIG. 15

SAMPLE WAVEFORMS

SMALL VALUES

Run 1-11

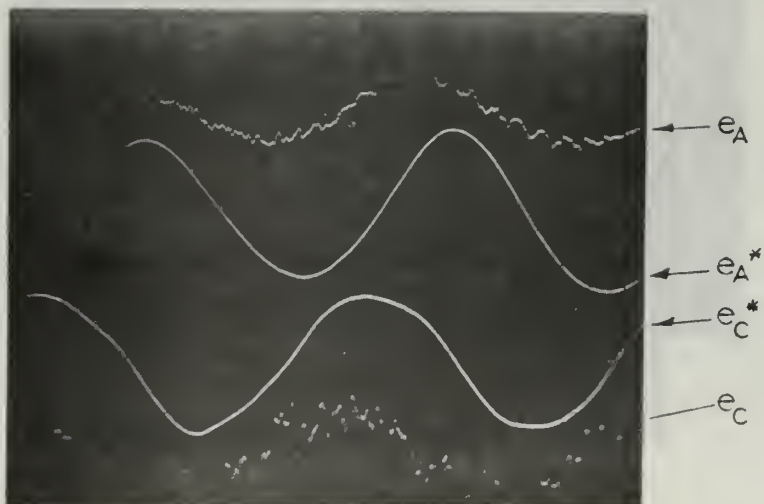
Sweep Rate = 20 msec/cm



* Filtered Signal

Run 1-11

Sweep Rate = 20 msec/cm

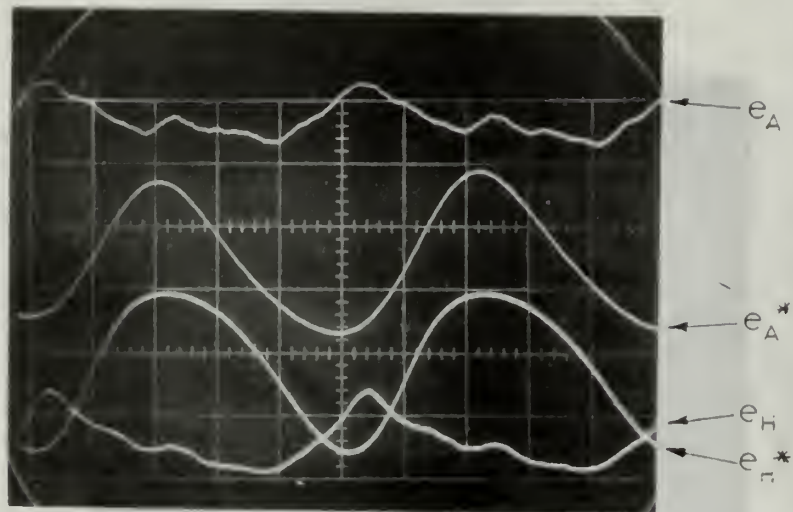


SAMPLE WAVEFORMS

MEDIUM VANCES

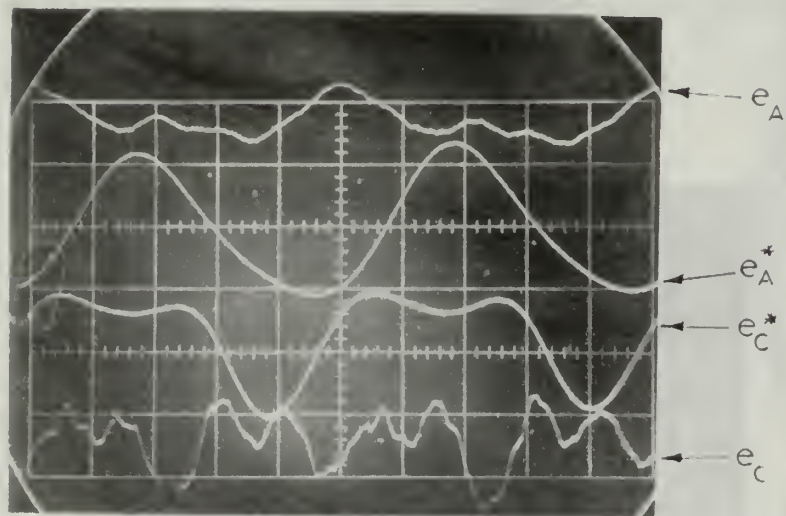
Run 12-8

Sweep Rate = 10 msec/cm



Run 12-8

Sweep Rate = 10 msec/cm



* Filtered Signal

FIG. 17
SIGNAL DISTORTION
LARGE VALUES

Run 9-9

Sweep Rate = 20 msec/cm



Run 9-9

Sweep Rate = 20 msec/cm



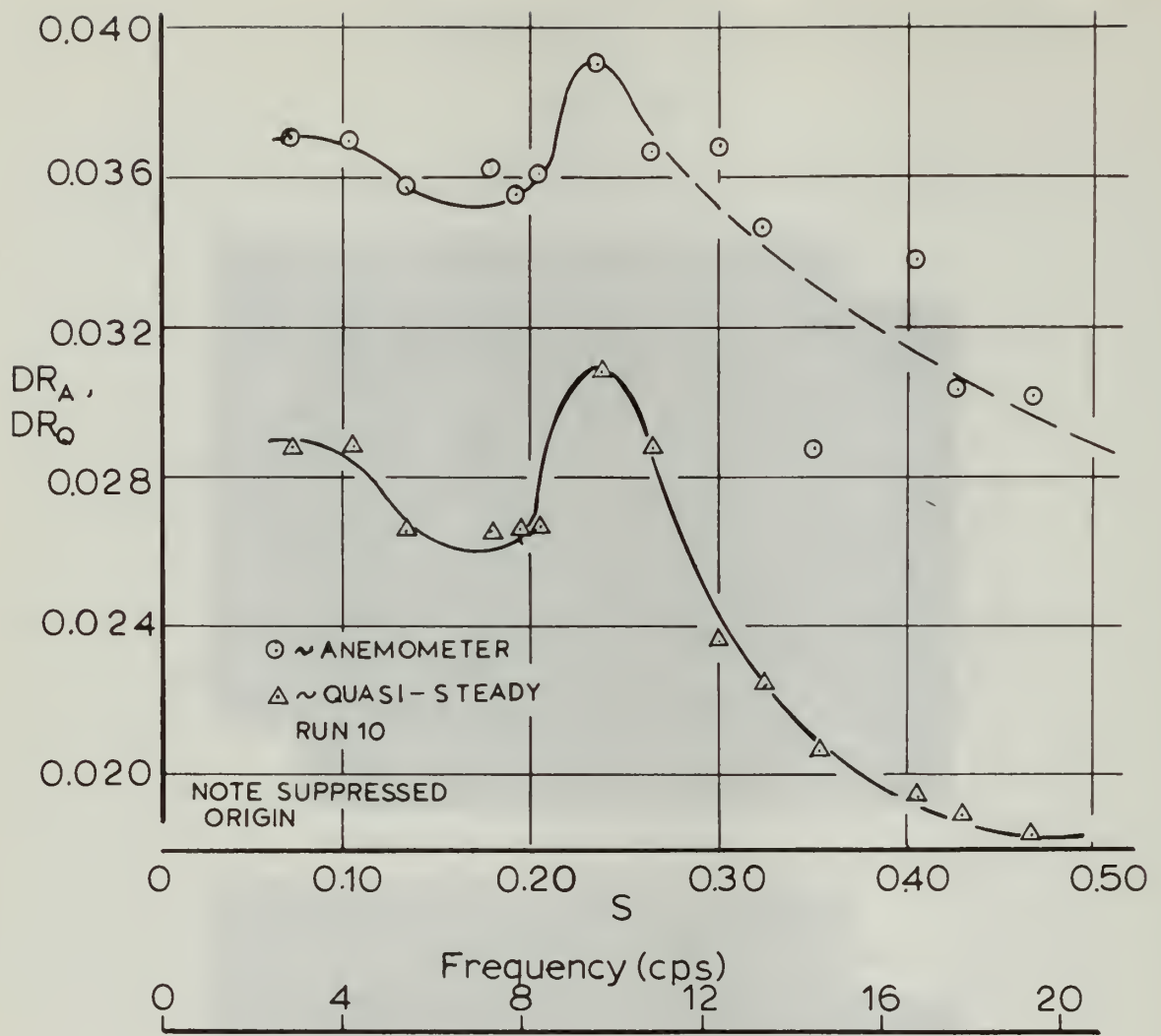


FIG.18: DRAG RATIO VARIATION (Small Vanes, $q=1.0$ psf)

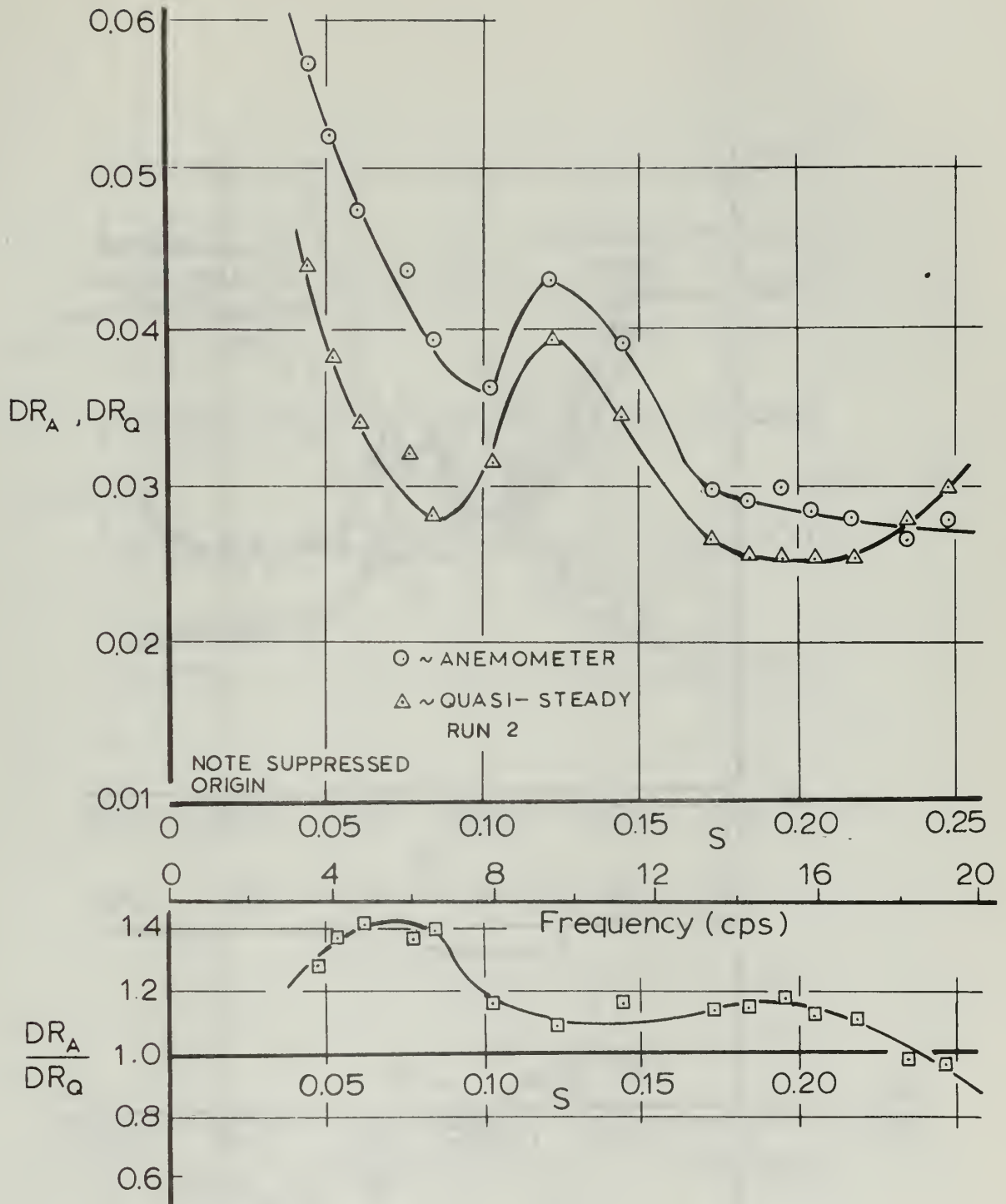


FIG.19: DRAG RATIO VARIATION (Small Vanes, $q=2.3$ psf)

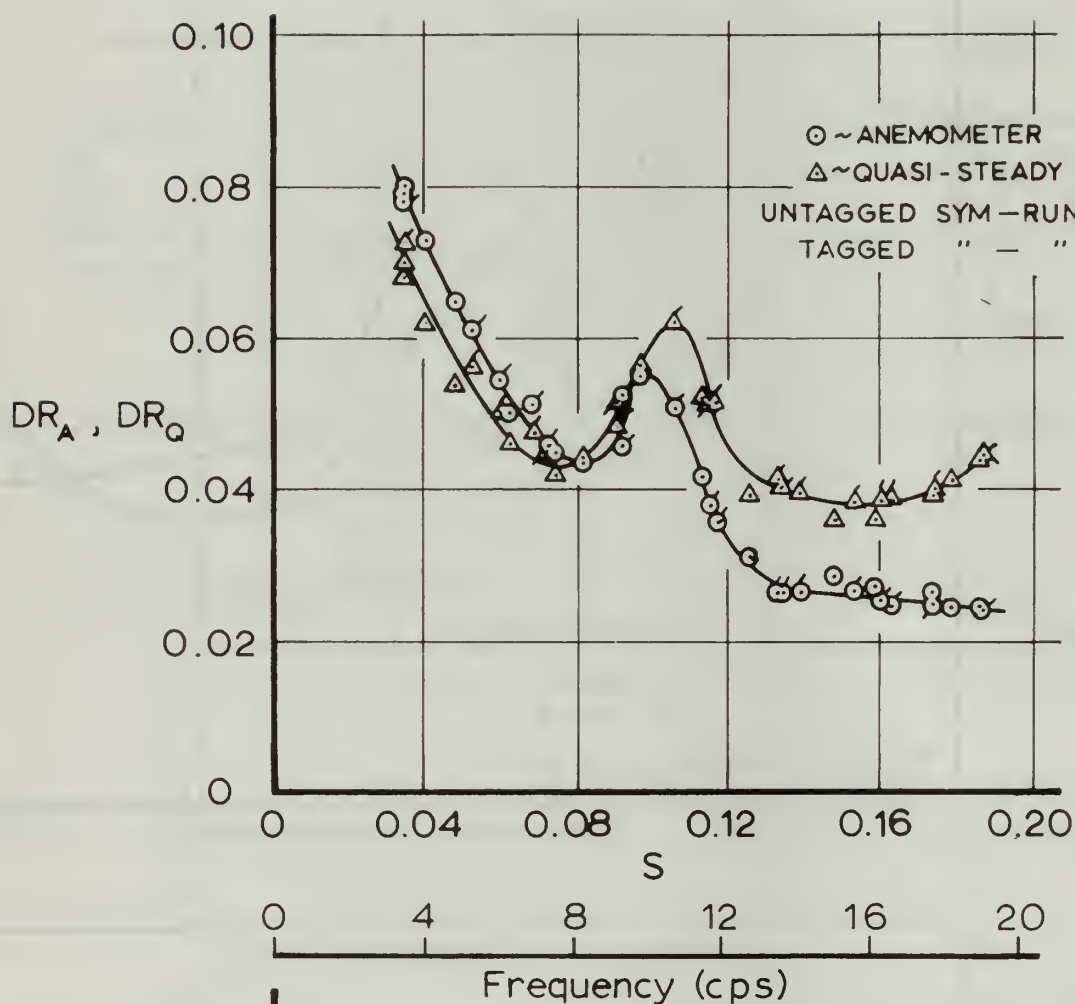


FIG. 20: DRAG RATIO VARIATION (Small Vanes, $q=4.2$ psf)

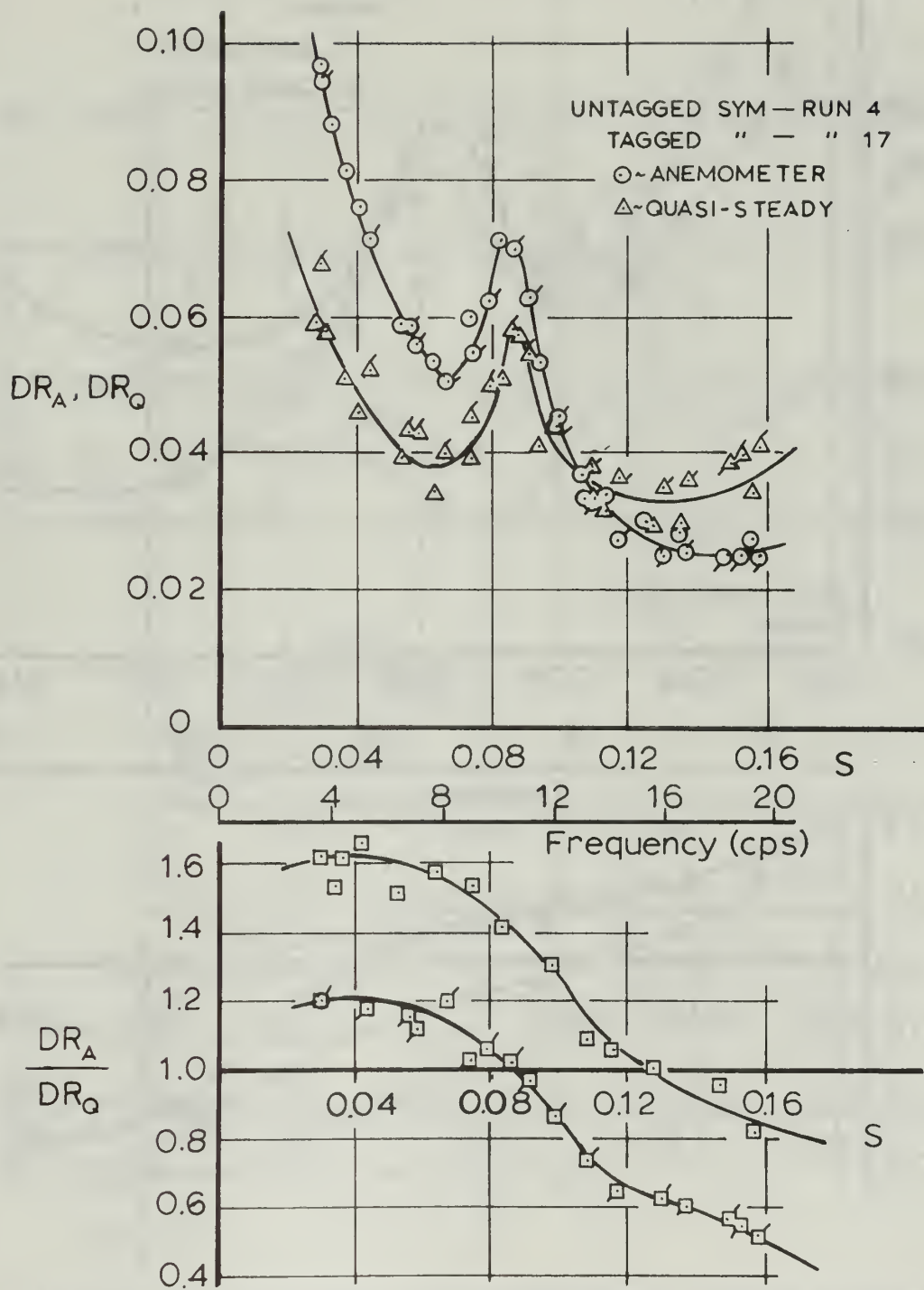


FIG.21: DRAG RATIO VARIATION (Small Vanes, $q=5.9$ psf)

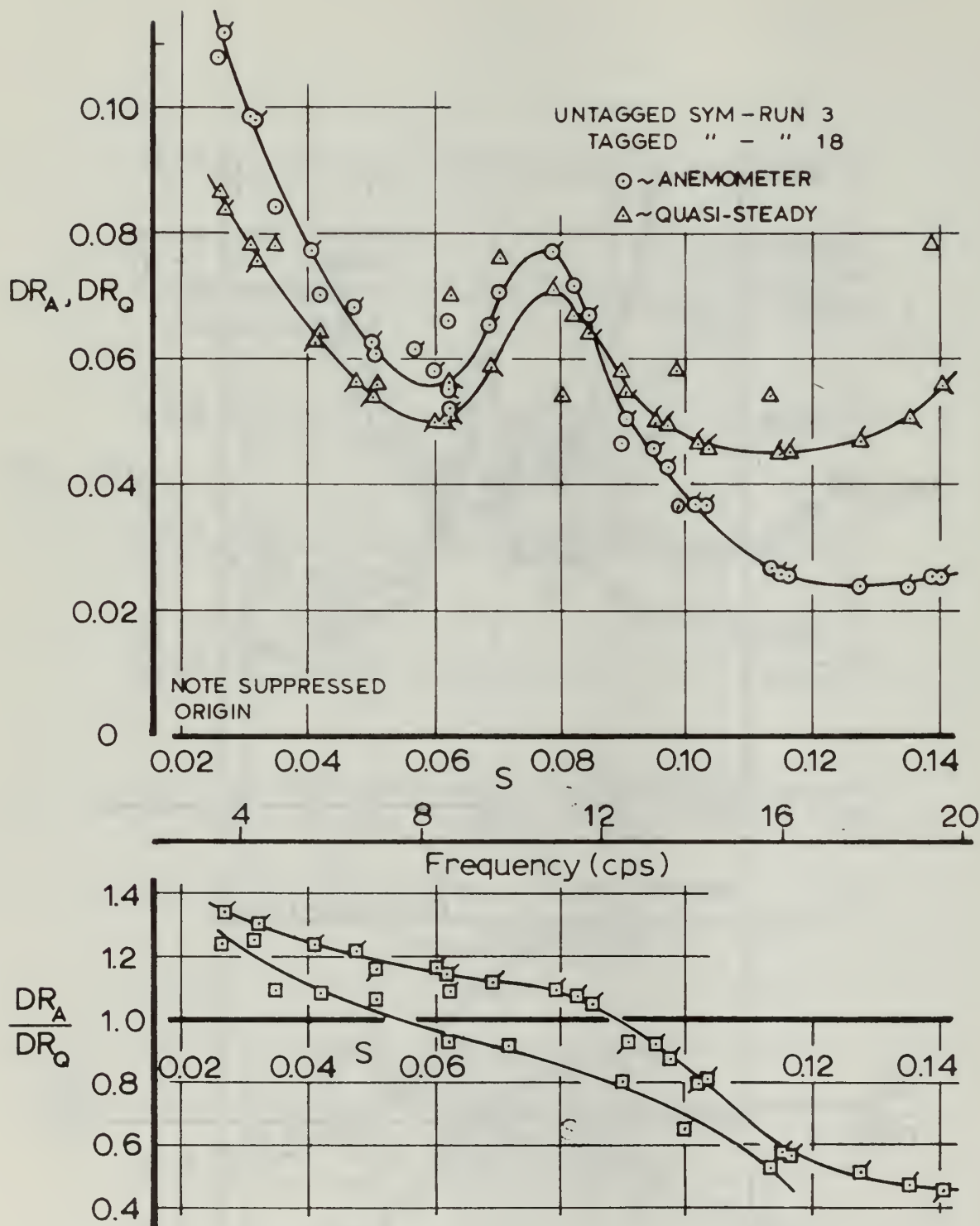


FIG. 22: DRAG RATIO VARIATION (Small Vanes, $q=7.6$ psf)

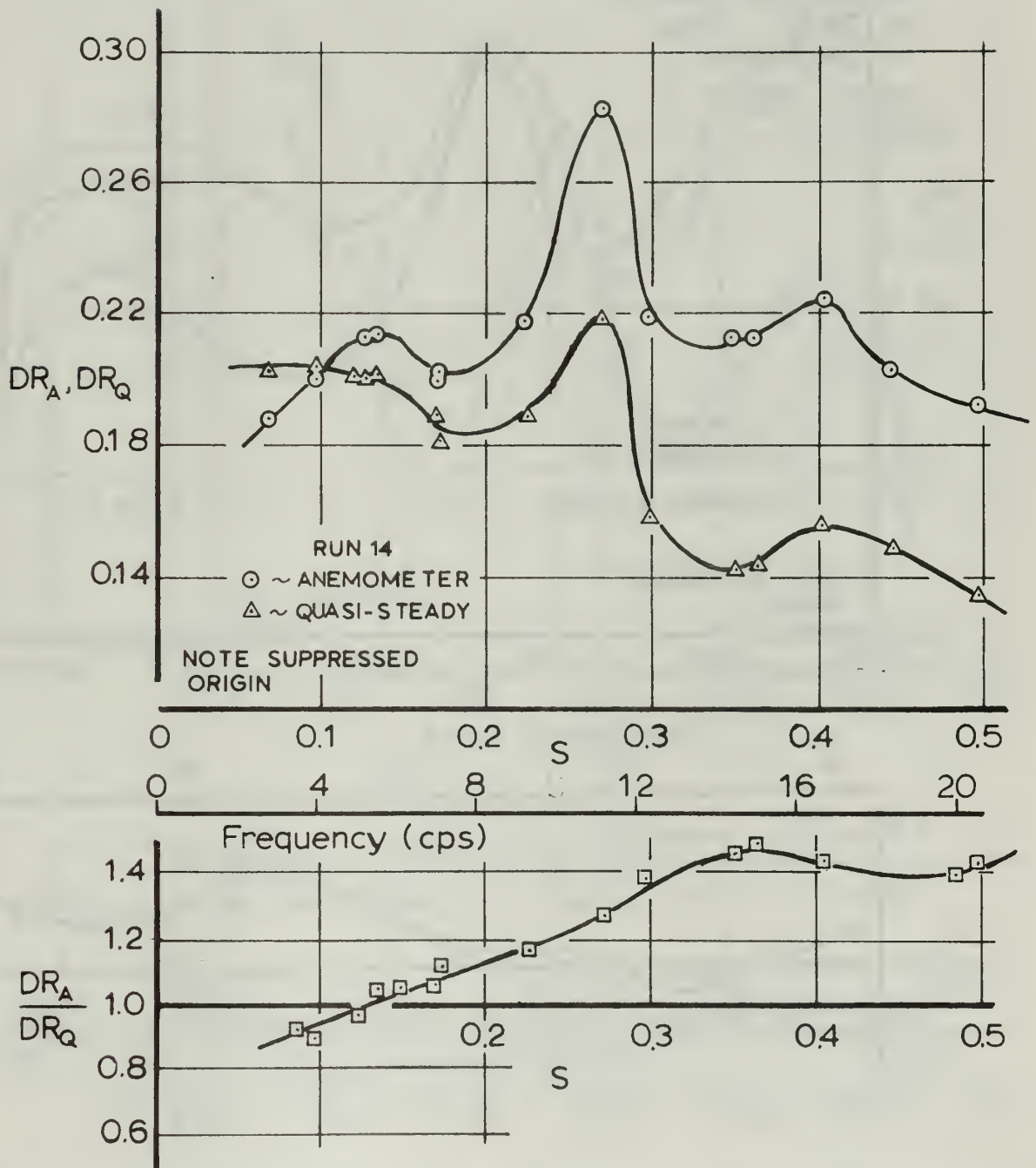


FIG. 23: DRAG RATIO VARIATION (Medium Vanes, $q=0.7$ psf)

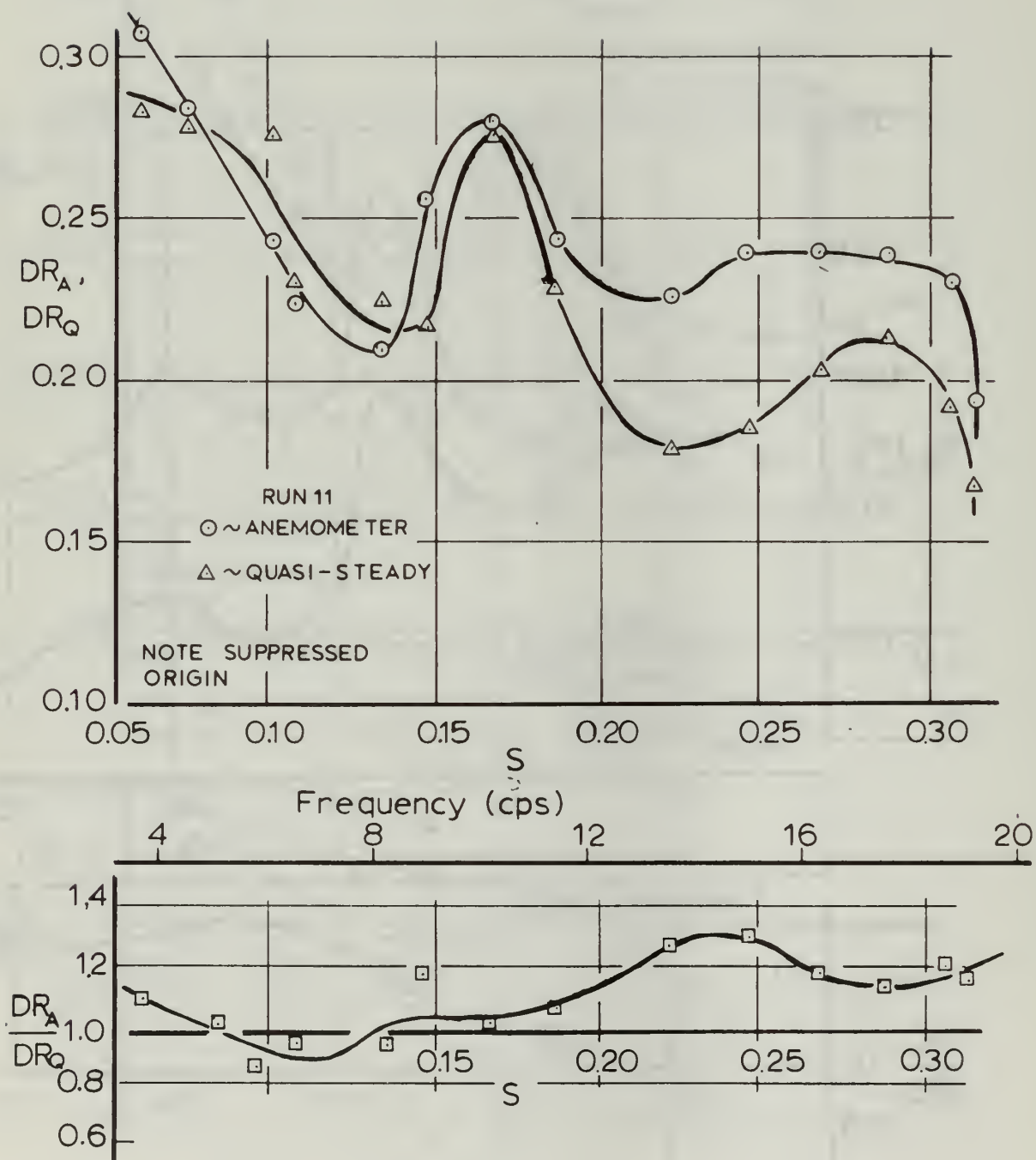


FIG. 24: DRAG RATIO VARIATION (Medium Vanes, $q=1.4$ psf)

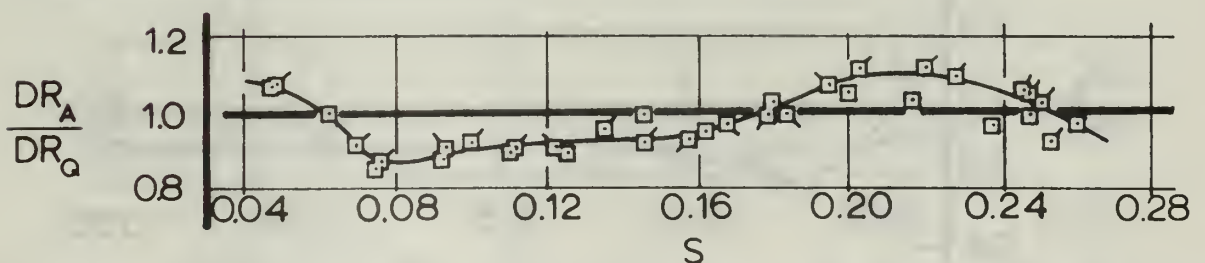
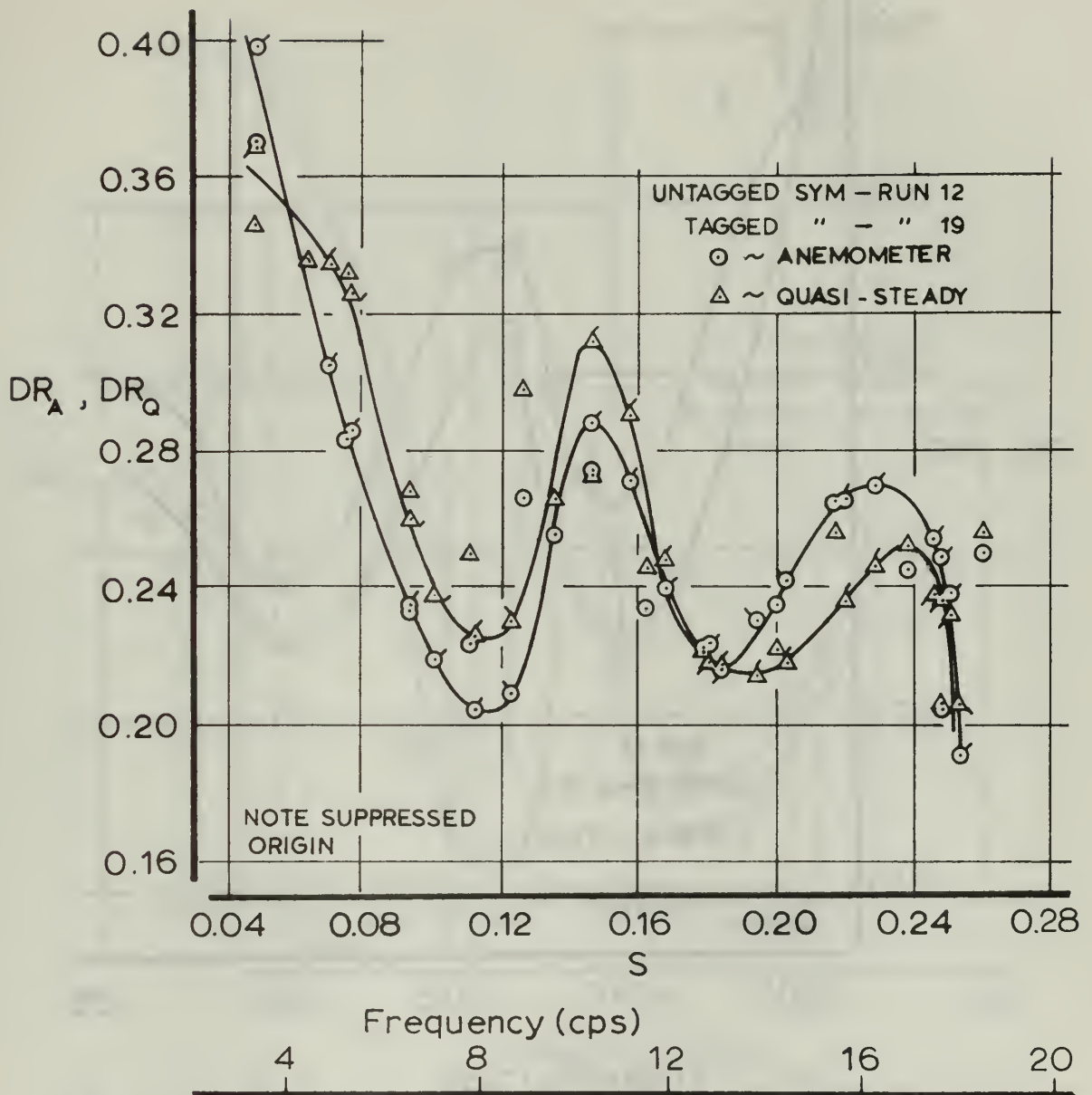


FIG.25: DRAG RATIO VARIATION (Medium Vanes, $q=2.2$ psf)

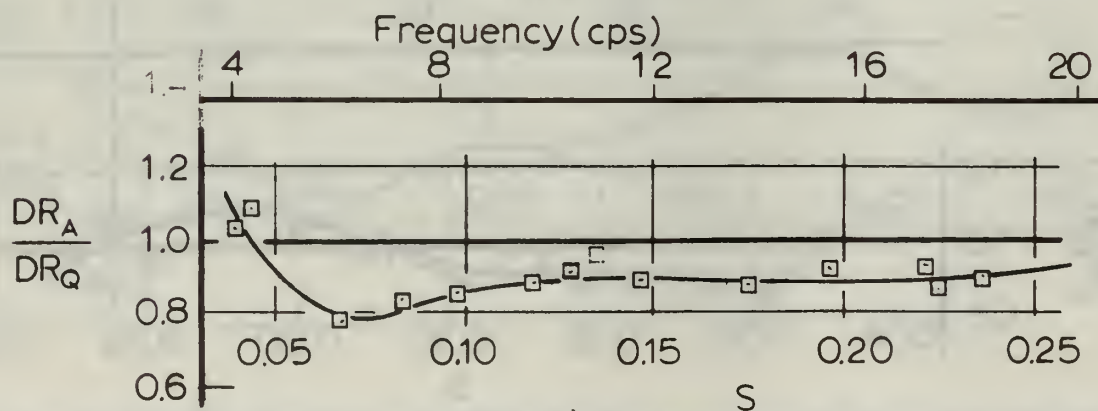
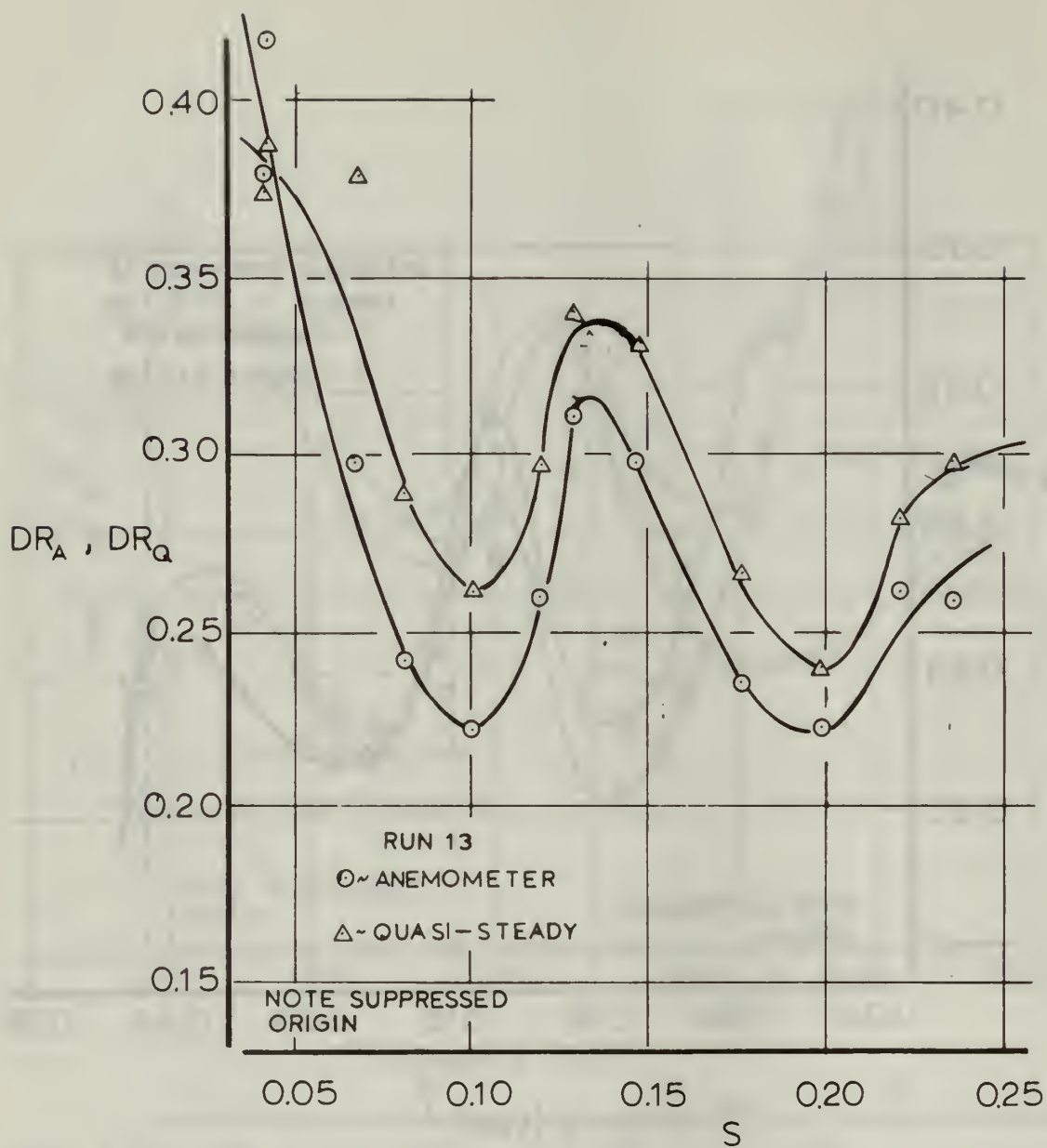


FIG. 26: DRAG RATIO VARIATION (Medium Vanes, $q = 2.6 \text{ psf}$)

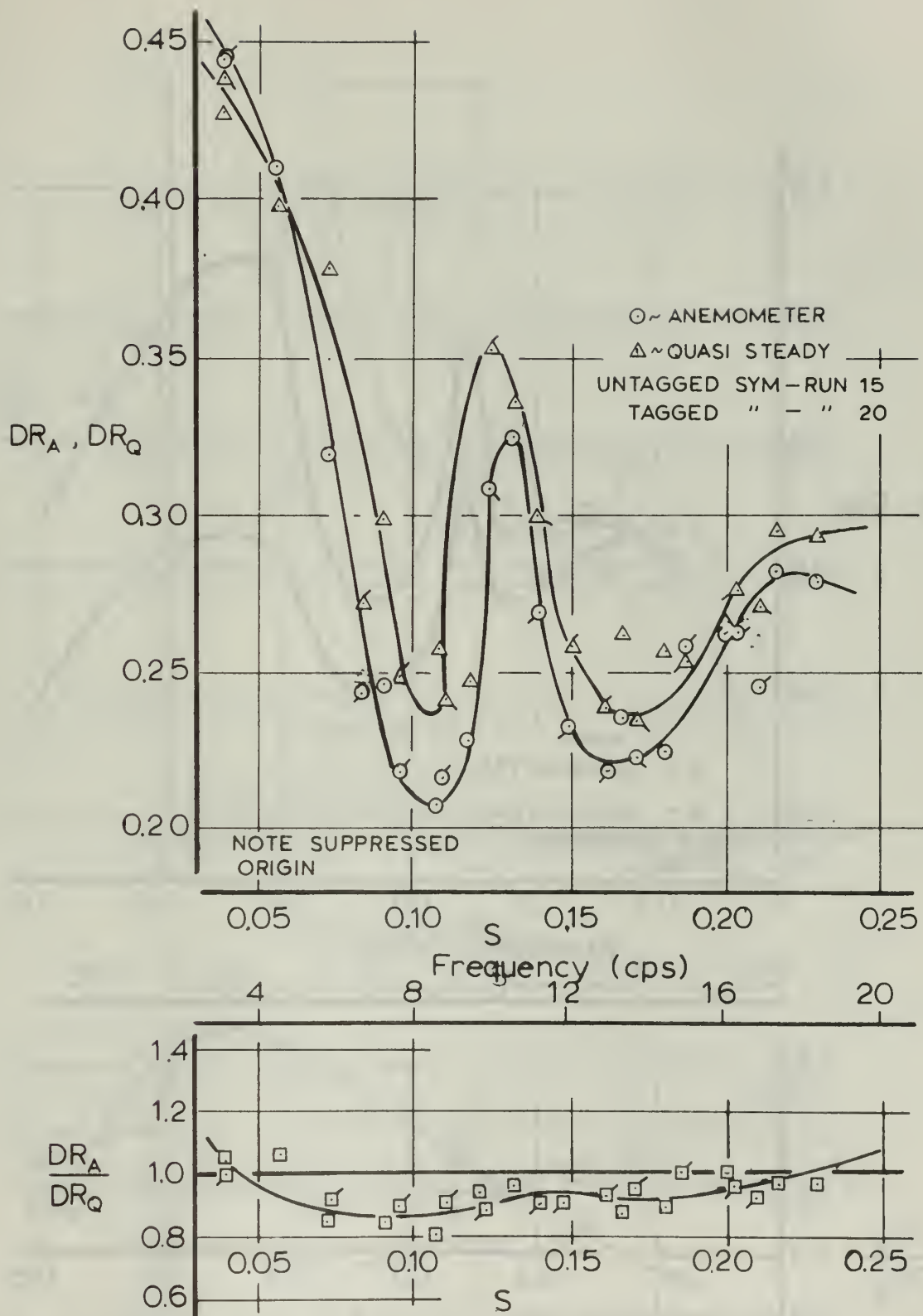


FIG.27: DRAG RATIO VARIATION (Medium Vanes, $q=2.8\text{psf}$)

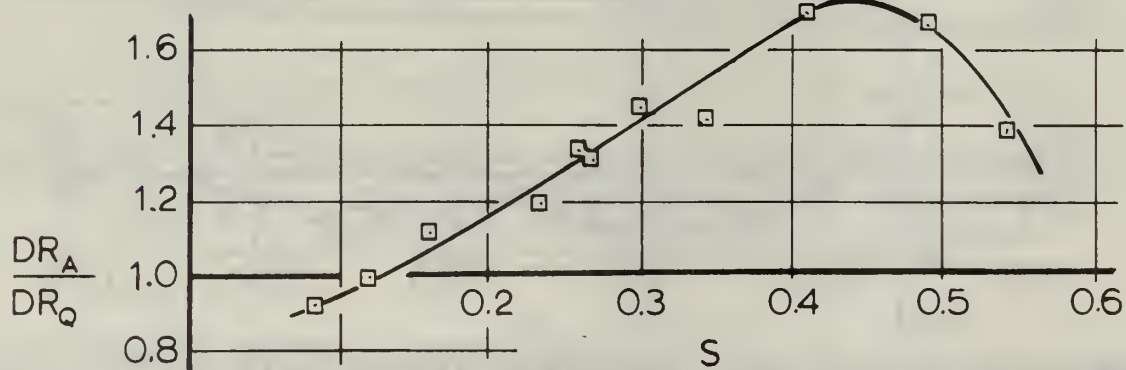
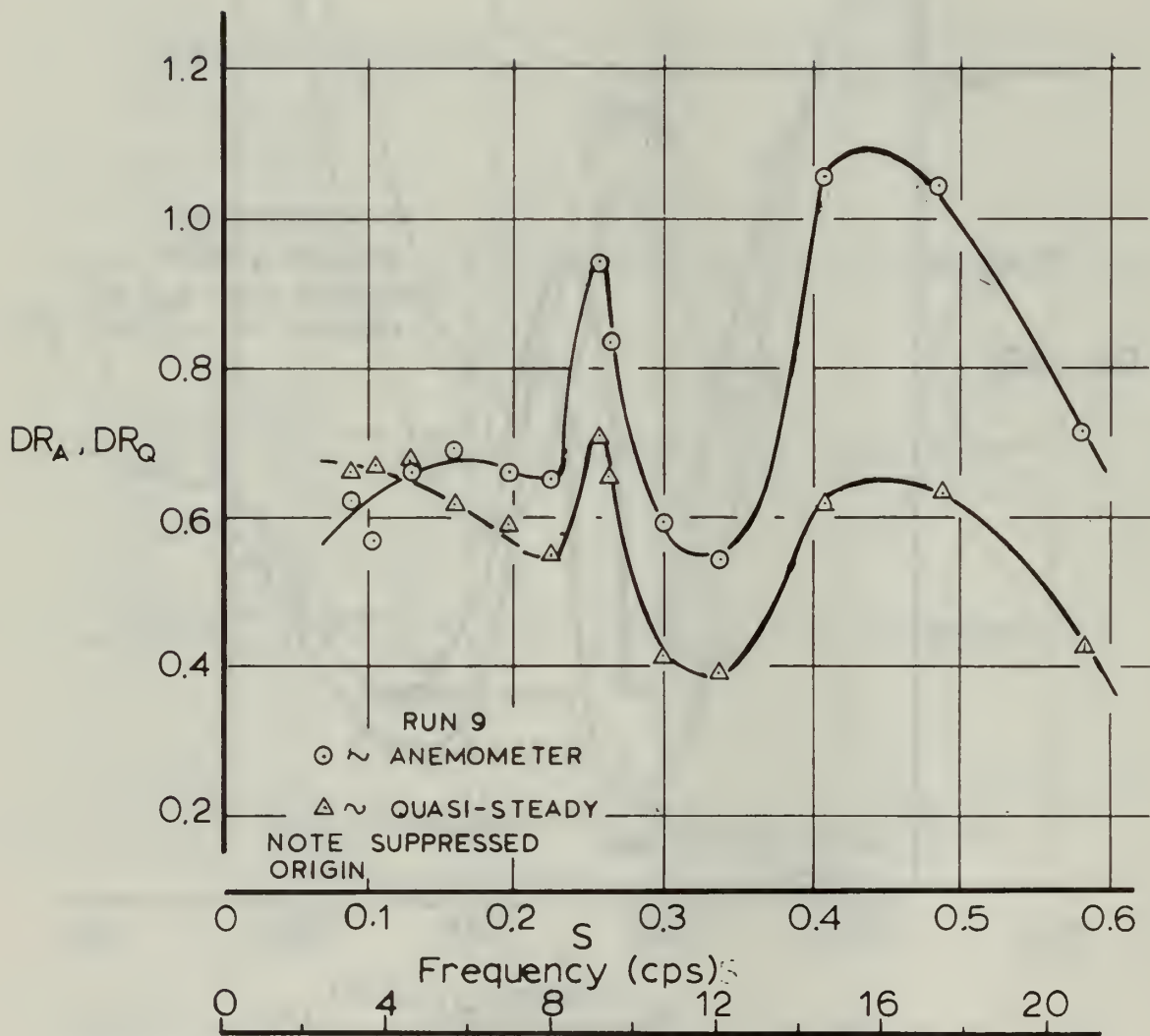


FIG.28: DRAG RATIO VARIATION (Large Vanes, $q=0.6$ psf)

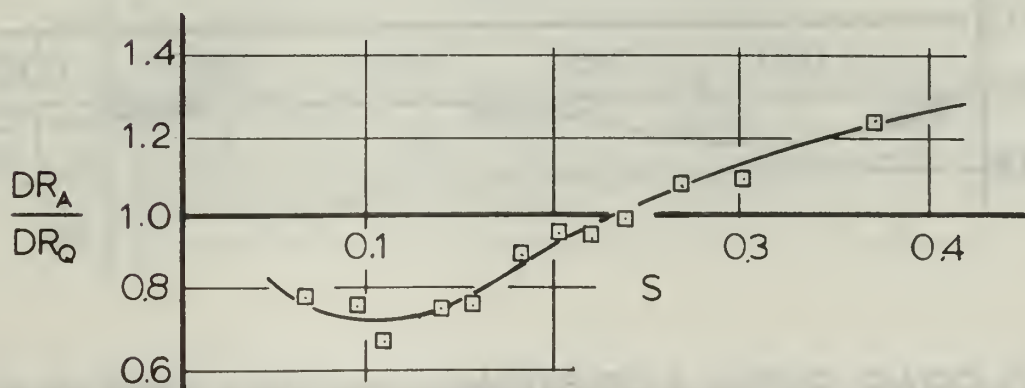
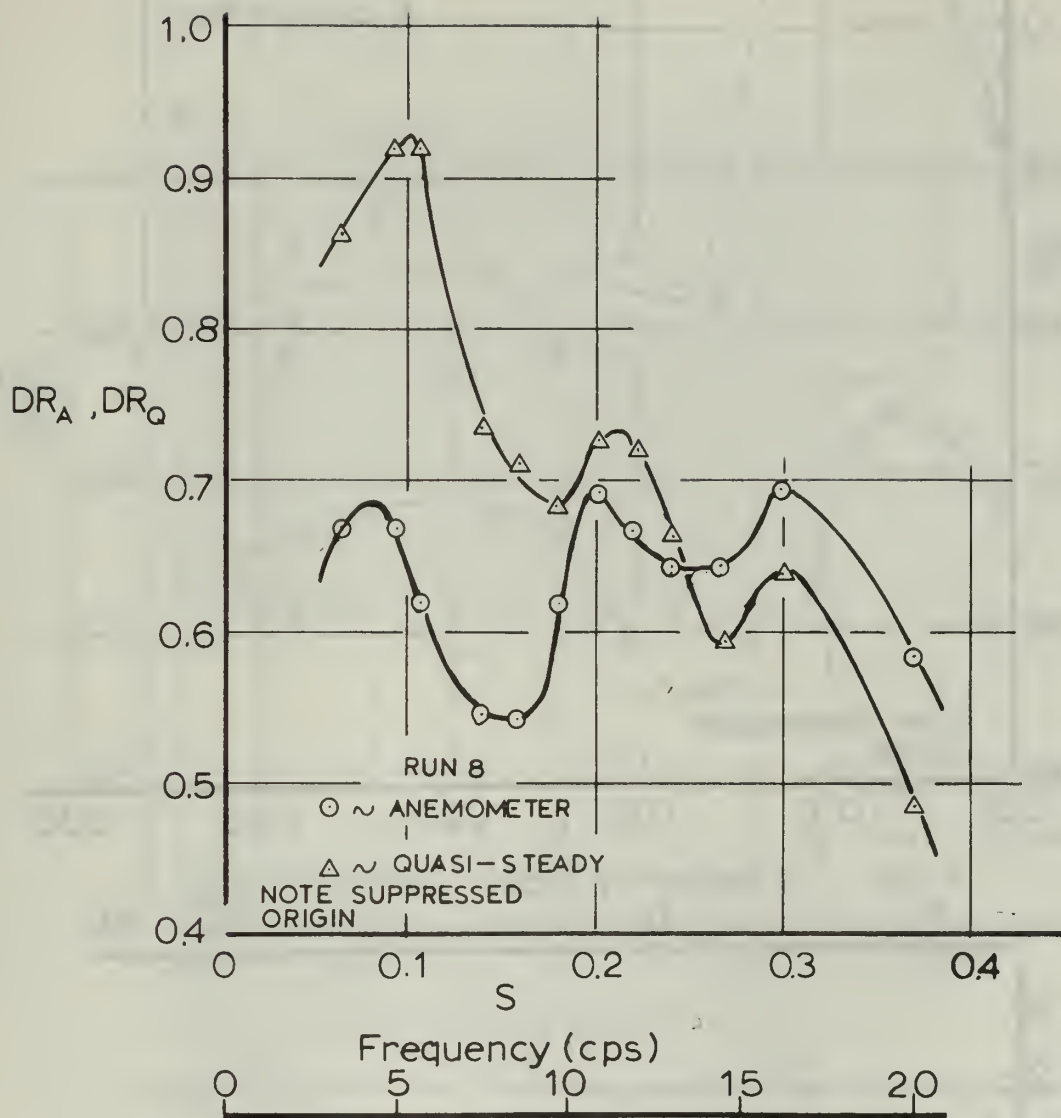


FIG. 29: DRAG RATIO VARIATION (Large Vanes, $q=1.2$ psf)

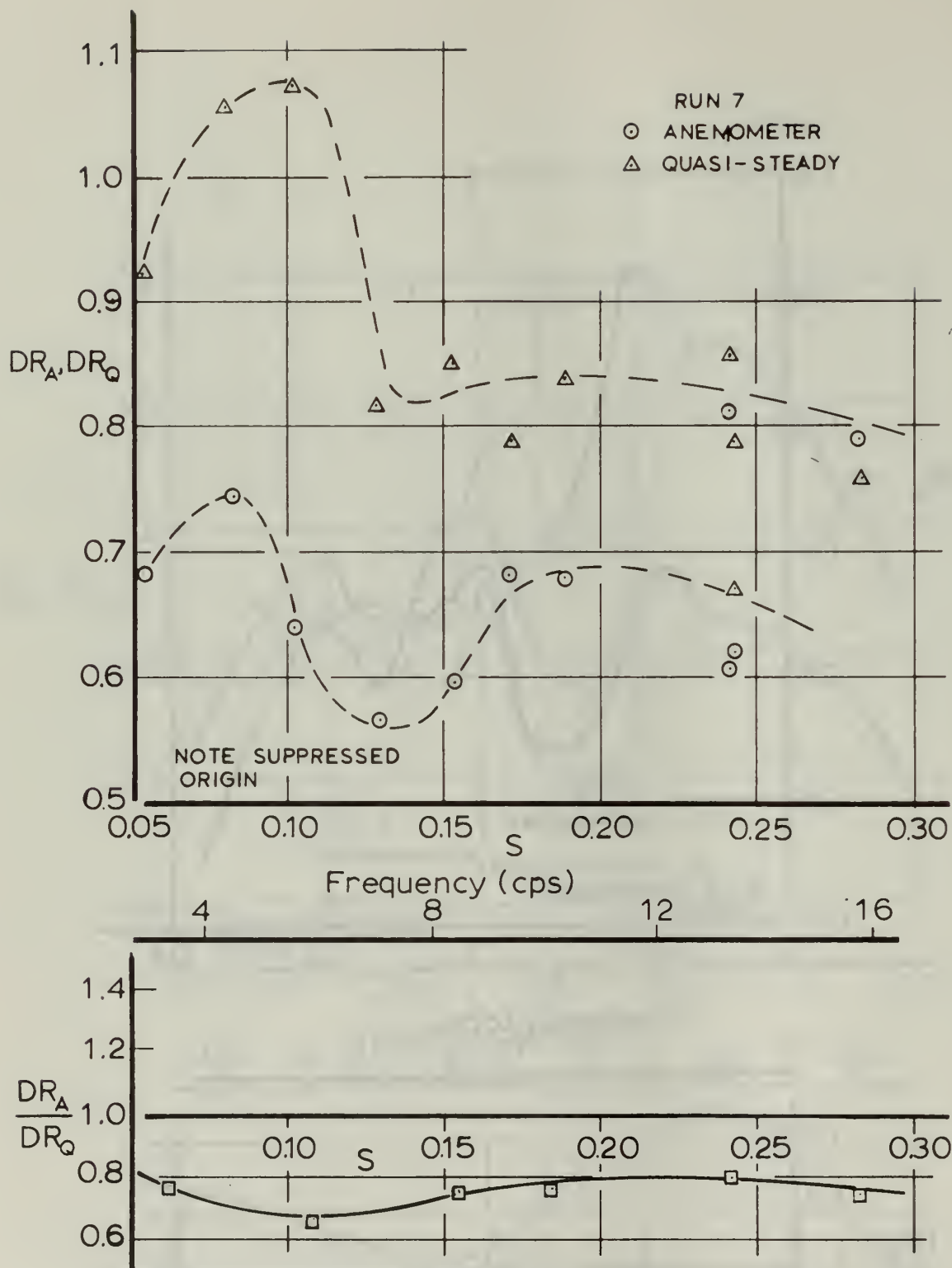


FIG. 30: DRAG RATIO VARIATION (Large Vanes, $q=1.3 \text{ psf}$)

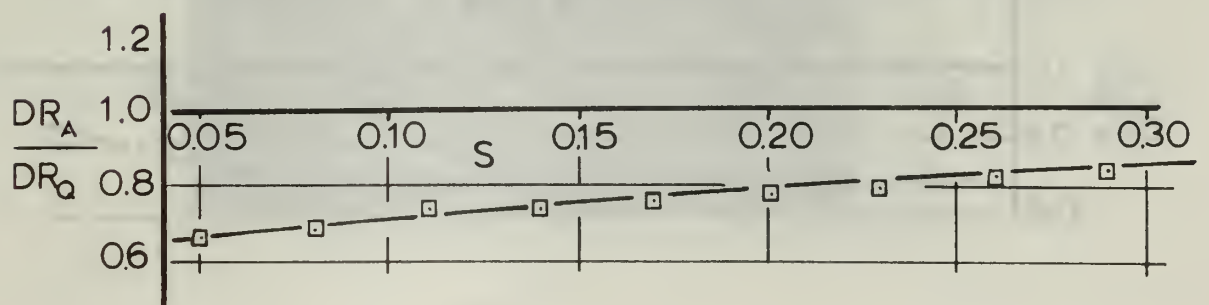
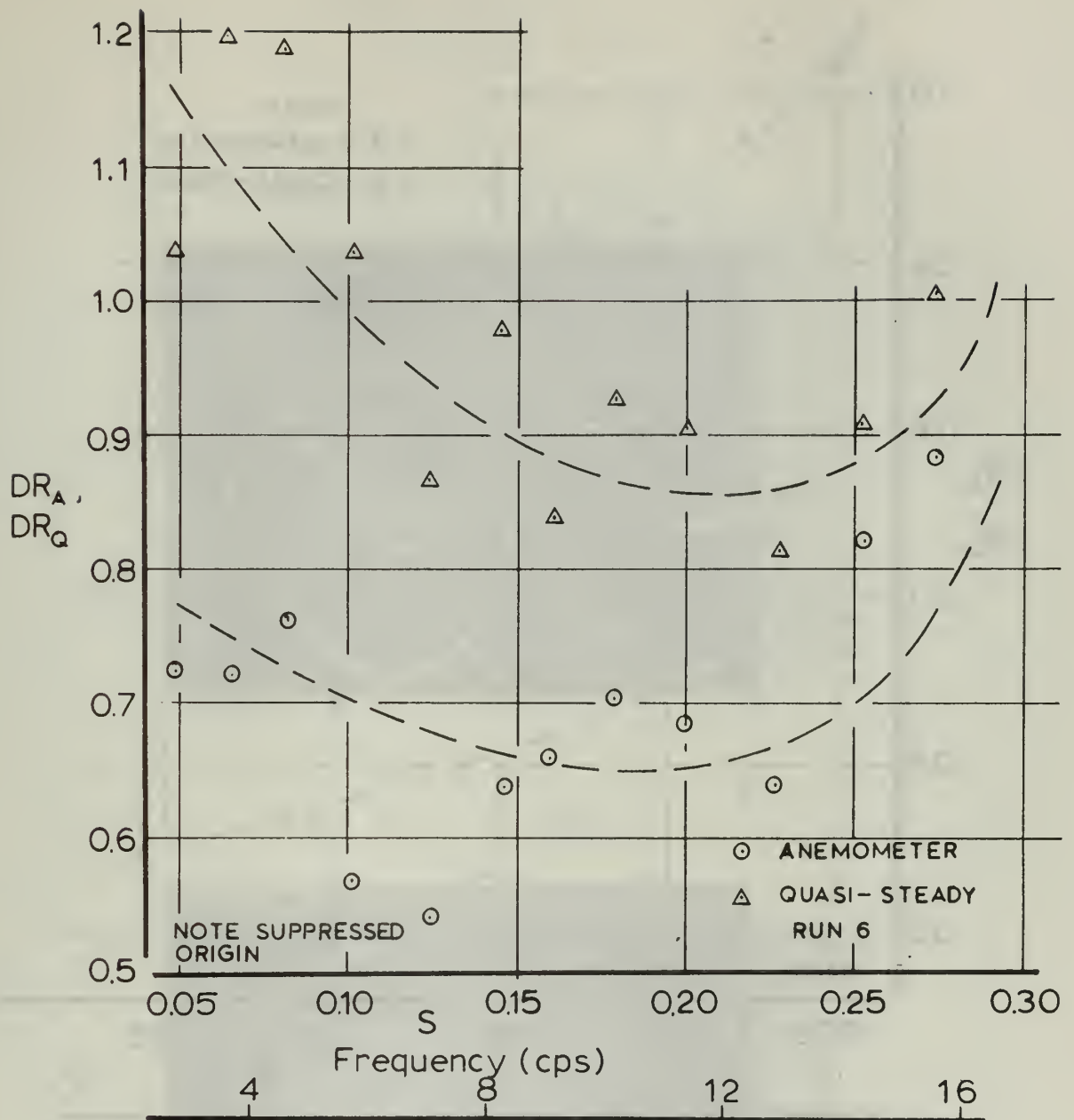


FIG.31: DRAG RATIO VARIATION (Large Vanes, $q=1.5\text{psf}$)

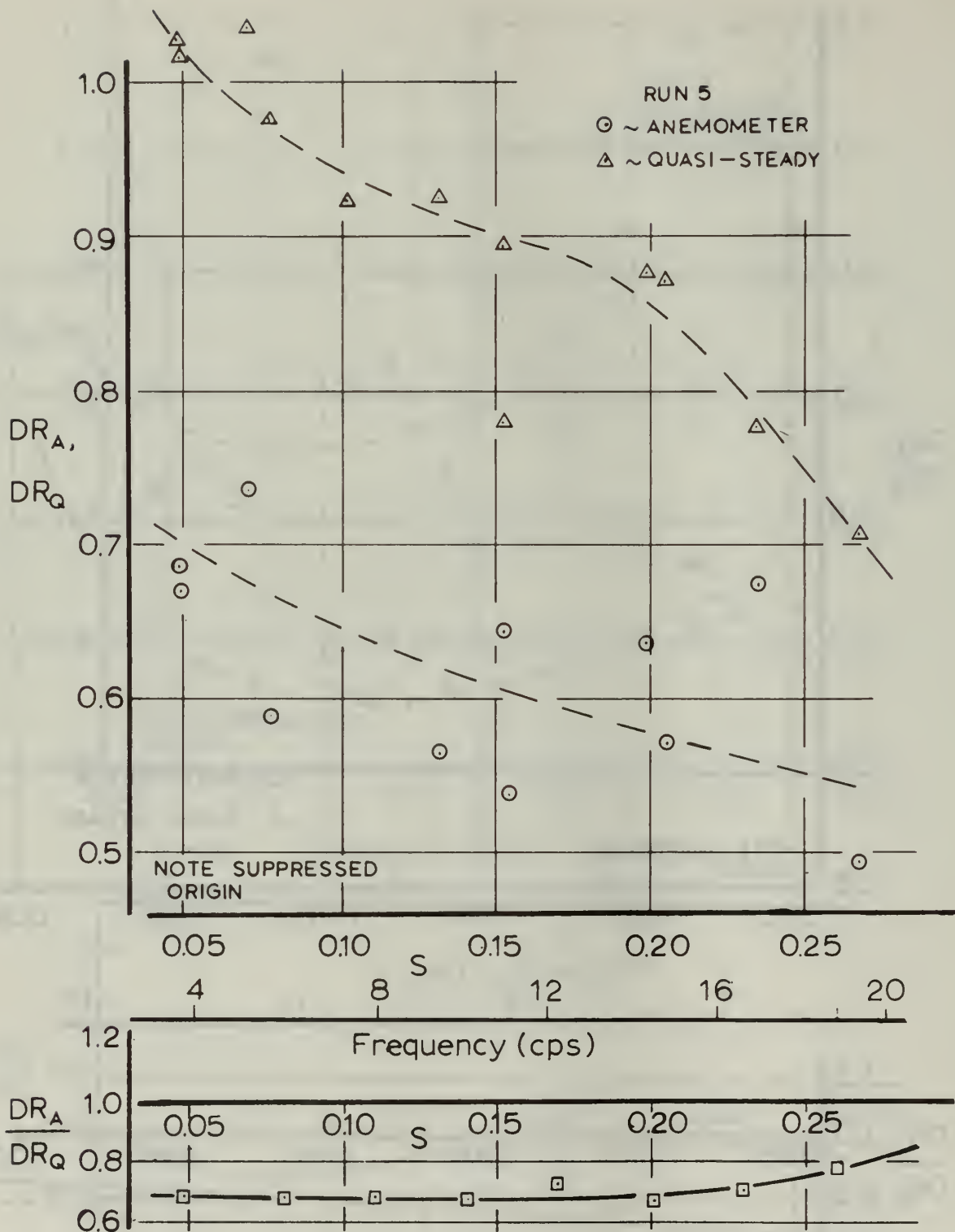
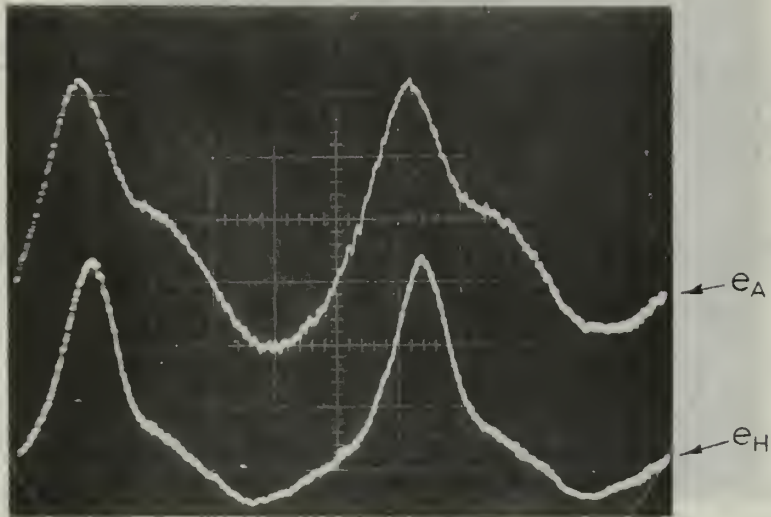


FIG. 32: DRAG RATIO VARIATION (Large Vanes, $q=1.7$ psf)

FIG. 53
SECOND HARMONIC
INFLUENCE

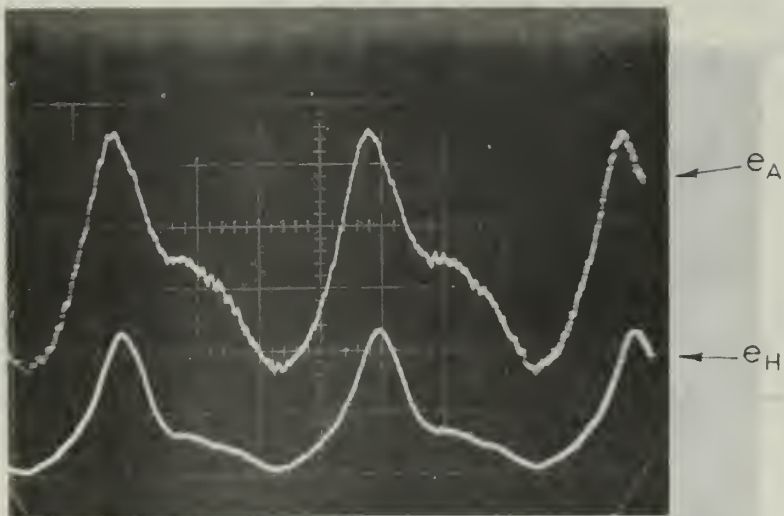
Run 12-1

Sweep Rate = 50 msec/cm



Run 12-14

Sweep Rate = 50 msec/cm



SPHERE VIBRATION

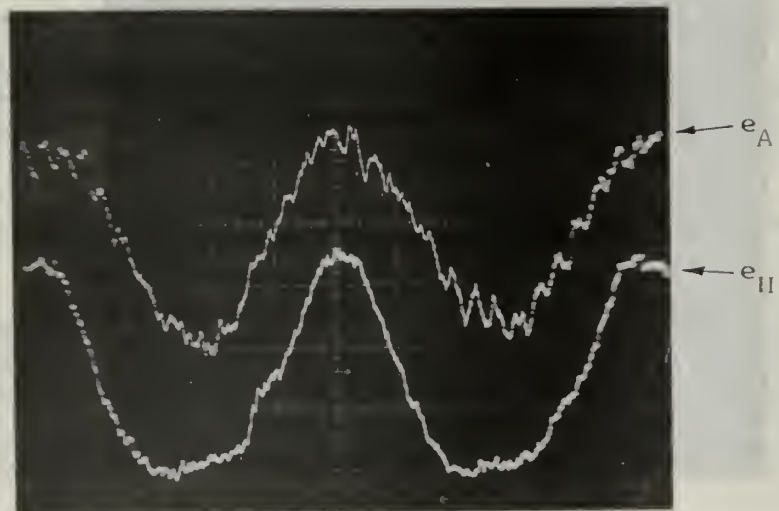
Run 1-3

Sweep Rate = 20 msec/cm



Run 1-4

Sweep Rate = 20 msec/cm



NOTE:

1. BRIDGE EXCITATION = 10.0 VOLTS (D.C.)

2. STATIC SENS. = $G_C(0) = 4.0$ MV/g

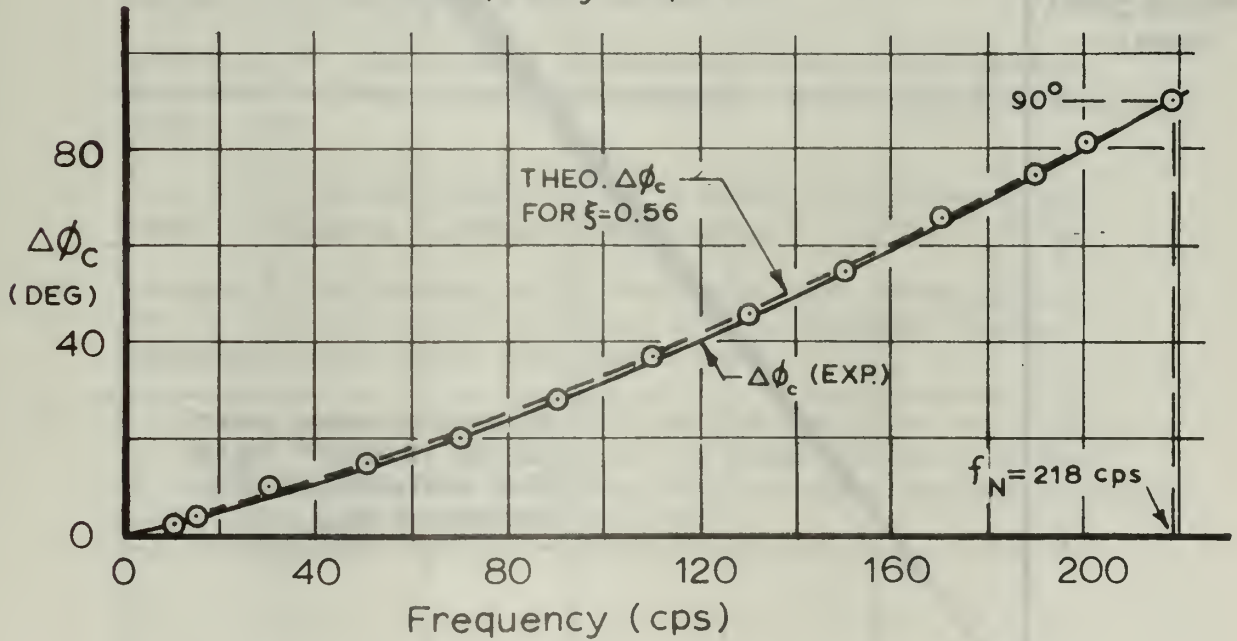
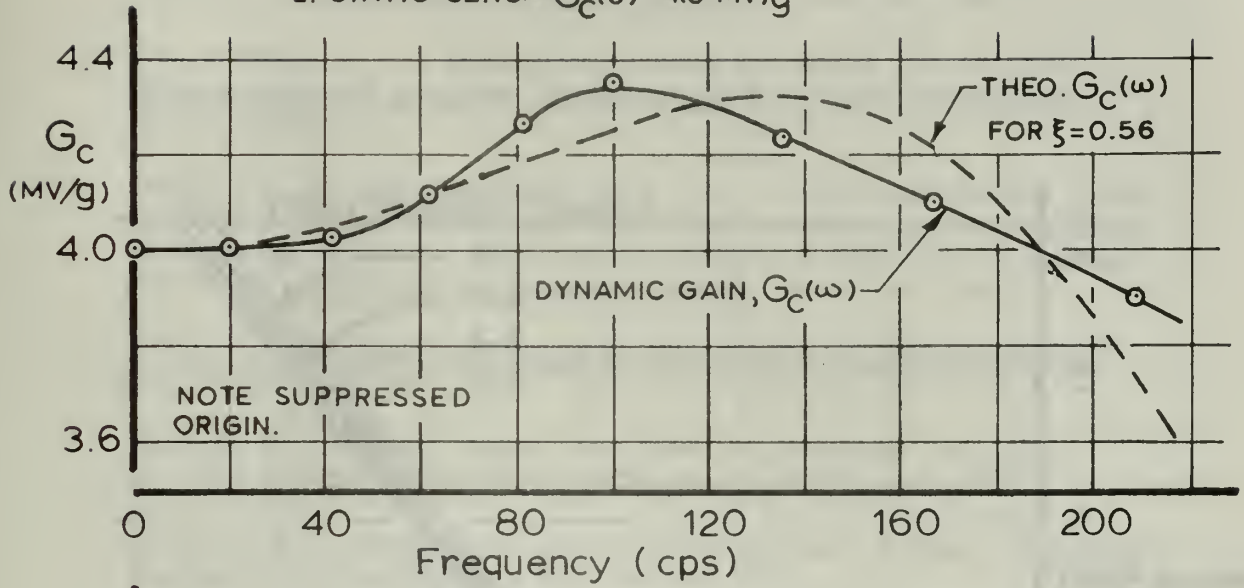


FIG. 35: STATHAM ACCELEROMETER CALIBRATION

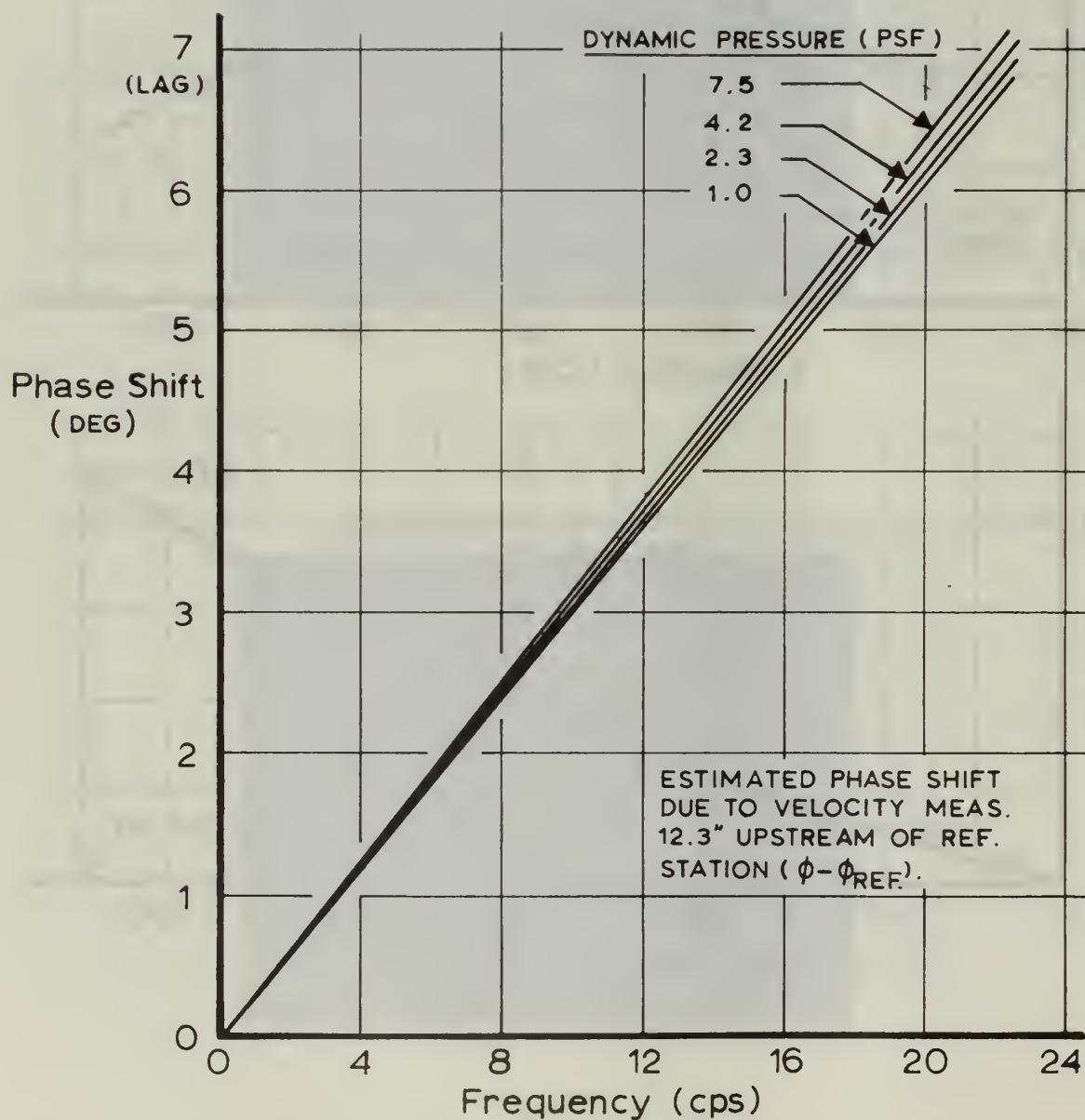


FIG. 36: SENSOR SEPARATION PHASE SHIFT

BIBLIOGRAPHY

1. Buell, D. A., et al. A Wind-Tunnel Investigation of Ground Wind Loads on Axisymmetric Launch Vehicles. NASA, TN D1893, 1963.
2. Davenport, A. G. An Approach to the Wind Tunnel Modelling of the Response of Structures to the Natural Wind. Paper presented at the Meeting on Ground Wind Load Problems in Relation to Launch Vehicles, NASA Langley Research Center, June 7-8, 1966.
3. Den Hartog, J. P. Transmission Line Vibration Due to Sleet. Transactions of American Institute of Electrical Engineers, v. 49, 1930.
4. Duncan, R. L. and Foughner, J. T., Jr. Wind Measurements Using a Vertical Array of Fast Response Anemometers. Paper presented at Meeting on Ground Wind Load Problems in Relation to Launch Vehicles, NASA Langley Research Center, June 7-8, 1966.
5. Fung, Y. C. An Introduction to the Theory of Aeroelasticity, John Wiley and Sons, 1955.
6. Isaacs, R. Airfoil Theory for Flows of Variable Velocity. Journal of the Aeronautical Sciences, v. 12 No. 1, 1945.
7. Miller, J. A. Transition in Oscillating Blasius Flow. Illinois Institute of Technology, PhD Thesis, 1963.
8. Murphy, J. C. The Effects of Nonsteady Flow on the Pressure Distribution About a Circular Cylinder. Thesis, Naval Postgraduate School, 1966.
9. Reed, W. H. III and Lynch, J. W. A Simple Fast Response Anemometer. Journal of Applied Meteorology, v. 2, No. 3, 1963.
10. Scruton, C. and Walshe, D. E. The Aerodynamic Investigation for the Proposed Tamar Suspension Bridge. National Physical Laboratory, Aero Report 311, August 1956.
11. Scruton, C. On the Wind Excited Oscillations of Stacks, Towers, and Masts. Paper 16 presented at the International Conference on the Wind Effects on Buildings and Structures, National Physical Laboratory, Teddington, England, 1963.

Accelerometer Calibration:

Calibration of the Statham accelerometer was obtained by measuring amplitude and frequency of motion, plus phase shift, between motion and accelerometer output when the accelerometer was mounted on the table of a Calidyne shaker unit, model A88.

Amplitude of motion was obtained using a Bently distance detector unit which is effectively a reluctance gage that senses the change in distance of the air gap between a flat, non-magnetic conducting material and the sensor coil face. For the calibration range considered, the reluctance gage frequency response was the same as the static sensitivity with a distance resolution of ± 20 micro-inches. Frequency was sensed to an accuracy of ± 0.1 cycles per second (cps) using a conventional electronic counter unit, Hewlett-Packard, model 522. Phase angle difference was sensed by an AD-YU, type 405 phase meter which had an accuracy of ± 1.0 degree.

The Statham accelerometer was operated at a 10.0 volt (D.C.) bridge excitation level and had an approximate static sensitivity of 4.0 millivolts per "g" where the gravitational unit "g" corresponds to a standard value of 32.2 feet per second². The dynamic response of the accelerometer is shown on Figure 35 including both gain, $G_C(\omega)$, and phase lag characteristic $\Delta\phi_C$. The acceleration response was checked for linearity at constant frequency up to two g's. The undamped resonant frequency, f_N , was evaluated as being 218 cps using the criteria of ninety degrees phase lag. The accelerometer was estimated to have a damping ratio of 0.558 relative to critical damping, and comparison is shown on the frequency response plot.

The calibration may be considered as related to true acceleration by the relationship:

If true acceleration is

$$\ddot{x}(t) = A \sin \omega t$$

Then the accelerometer reading will be (A.01)

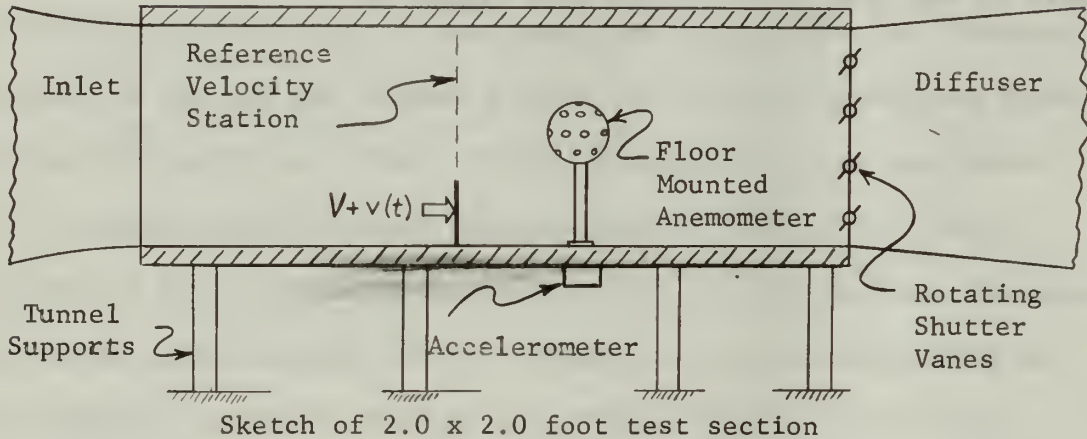
$$e_c(t) = A G_c \sin(\omega t - \Delta\phi_c)$$

Where G_c and $\Delta\phi_c$ are obtained from Figure 32.

APPENDIX B

Anemometer Corrections For Tunnel Floor Accelerations

It is the purpose of this section to illustrate a method for correcting the drag sphere anemometer balance-voltage reading for the influence of tunnel floor accelerations in the horizontal axial direction. A sketch of the environment is indicated below:



At the reference velocity station, the hot wire provides an indication of the air velocity. This station will be used as a source for the origin of time.

$$V + v(t) = V [1 + \sigma \sin \omega t] \quad (\text{B.01})$$

where σ represents the magnitude of velocity perturbation relative to the steady velocity value. The floor will experience an acceleration due to the aerodynamic loading induced by the operation of the rotating shutter mechanism, and this will occur principally in the horizontal axial direction. For purposes of this discussion, let us assume that the motion is harmonic in character at the dominant forcing frequency.

The floor acceleration can be expressed as:

$$\ddot{x}(t) = C_1 \sin(\omega t - \phi_1) \quad (\text{B.02})$$

where it is recognized that the quantities C_1 , and ϕ_1 , are not measurable directly.

The Statham accelerometer, which is firmly attached to the floor beneath the drag sphere anemometer installation, was aligned to respond to accelerations in the horizontal axial direction. Its electrical signal output due to the acceleration environment of equation B.02 will be:

$$e_c(t) = C_2 \sin(\omega t - \phi_2) \quad (\text{B.03})$$

where the quantities C_2 and ϕ_2 are directly measurable. From laboratory shaker table calibrations, it is known that:

$$C_2 = C_1 G_c(\omega) \quad , \text{ and}$$

$$\Delta\phi_c = \phi_2 - \phi_1$$

Also we know from a laboratory shaker table calibration of the drag sphere anemometer that

$$\begin{aligned} \Delta e_A(t) &= C_3 \sin(\omega t - \phi_3) \\ &= C_3 \sin[(\omega t - \phi_1) - \Delta\phi_A] \end{aligned} \quad (\text{B.04})$$

$$\text{where } C_3 = C_1 G_A(\omega) \quad , \text{ and } \Delta\phi_A = \phi_3 - \phi_1$$

Combining equations B.02 through B.04 allows us to estimate an inertial correction to the drag sphere balance reading. Note that ϕ_1 is cancelled out and is thus never required.

$$\Delta e_A(t) = C_2 \frac{G_A(\omega)}{G_c(\omega)} \sin[(\omega t - \phi_2) - \Delta\phi_A + \Delta\phi_c] \quad (\text{B.05})$$

The observed drag sphere anemometer balance output is directly measured and may be expressed as:

$$e_{A_{\text{OBS}}} = B \sin(\omega t - \phi_4) \quad (\text{B.06})$$

and it is desired to obtain a corrected reading in the form:

$$\begin{aligned} e_{A_{\text{CORR}}} &= B_{\text{CORR}} \sin(\omega t - \psi) \\ &= e_{A_{\text{OBS}}} - \Delta e_A \end{aligned} \quad (\text{B.07})$$

Solving equation B.07 in terms of quantities involved in equations B.05 and B.06, one obtains:

$$B_{\text{CORR}} = \left[B^2 + C_2^2 \frac{G_A^2}{G_c^2} - 2BC_2 \frac{G_A}{G_c} \cos(\phi_4 - \phi_2 - \Delta\phi_A + \Delta\phi_c) \right]^{1/2}$$

and

$$\psi = \arctan \left[\frac{\sin \phi_4 - \frac{C_2}{B} \frac{G_A}{G_c} \sin(\phi_2 + \Delta\phi_A - \Delta\phi_c)}{\cos \phi_4 - \frac{C_2}{B} \frac{G_A}{G_c} \cos(\phi_2 + \Delta\phi_A - \Delta\phi_c)} \right] \quad (\text{B.08})$$

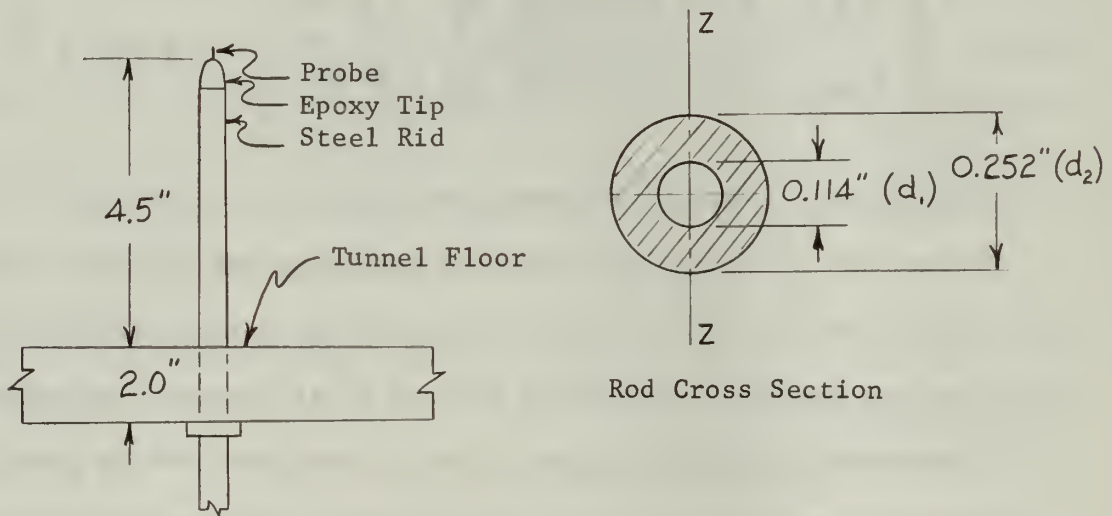
It should be noted that the phase relationship between the unsteady velocity and drag (hot wire and anemometer) is the correct relationship between the velocity at the hot wire and the drag at the anemometer. However it is not the relationship between the velocity and drag at the same point. Due to the longitudinal separation of hot wire and anemometer the pressure signals producing velocity perturbations reach the anemometer prior to reaching the hot wire. Based on the speed of sound in air, the mean flow velocity in the tunnel, the frequency of oscillation, and the distance between hot wire and anemometer, the maximum phase difference between velocity signals at the hot wire and anemometer, for the range of test conditions used, would be 7 degrees. This phase difference, due to the above factors, means that the phase angle (or time lag) between a velocity perturbation at the anemometer and the anemometer drag response is greater than

that indicated by phase angle measurements between the hot wire and the anemometer. Figure 36 shows the computed phase shift, due to the axial separation of the hot wire and anemometer sensors, as a function of frequency for four representative values of dynamic pressure.

APPENDIX C

Hotwire Response to Base Acceleration

An elementary beam theory analysis has been made for the cantilevered rod (supporting the hot wire probe and containing electrical leads) to determine the velocity of the probe induced by inertial loads during tunnel floor vibrations in the horizontal plane. The entire length of the rod (shown in the sketch below) was assumed to be identical to the hollow stainless steel portion in specific weight, cross section, and elastic properties.



SKETCH OF HOTWIRE INSTALLATION

The length of the rod was taken to be 6.5 inches since the rod is fixed at the bottom of the tunnel floor by a threaded collar arrangement. This is a conservative value because the floor provides some support due to the close fit between the rod and the hole through the floor.

The following properties and values were chosen or computed for the analysis:

Modulus of elasticity $E = 29 \times 10^6 \text{ lbs/in}^2$

Specific Weight $\gamma = 0.284 \text{ lbs/in}^3$

Second moment of the area with respect to the ZZ axis;

$$I_{ZZ} = \frac{\pi}{64} (d_2^4 - d_1^4)$$

$$I_{ZZ} = 1.895 \times 10^{-4} \text{ in}^4$$

Cross sectional area;

$$A = \frac{\pi}{4} (d_2^2 - d_1^2)$$

$$A = 0.0396 \text{ in}^2$$

Length of rod; $l = 6.5 \text{ in}$

Weight of rod per unit length $w' = \gamma A$

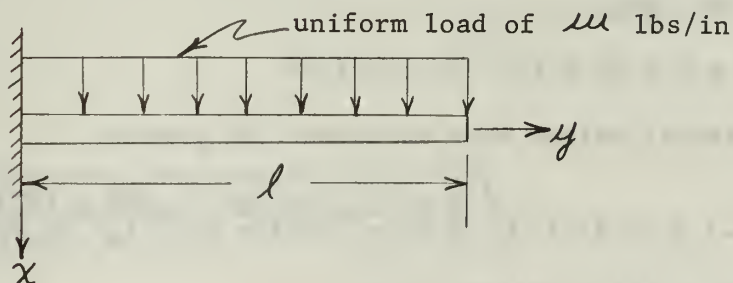
$$w' = 0.01125 \text{ lbs/in}$$

Weight of electrical leads $w'' = 0.05 w'$

Effective Weight $w = w' + w''$

$$w = 0.0118 \text{ lbs/in}$$

The vertically mounted rod, subjected to an acceleration of one "g" in a horizontal direction, is equivalent to the rod mounted horizontally, loaded by its own weight, as shown in the following sketch.



Elementary beam theory gives the deflection of the free end

($y = \ell$) as:

$$x = \frac{W \ell^3}{8 EI} \quad (C.01)$$

where, $W = w \ell$ under a one "g" condition, and the maximum deflection is then

$$x_0 = \frac{(0.0767) \text{ lbs } (6.5)^3 \text{ in}^3}{8 (2.9 \times 10^6) \text{ lbs/in}^2 (1.895 \times 10^{-4}) \text{ in}^4}$$

$$x_0 = 0.00048 \text{ in}$$

If the load were assumed to be applied harmonically, i.e.,

$$W = W_0 \sin \omega t, \quad (C.02)$$

then the deflections of the free end can be approximately expressed by

$$x = x_0 \sin \omega t \quad (C.03)$$

provided the frequencies of interest are small compared to the lowest natural frequency of the rod.

The natural frequencies of a continuous uniform beam are given by

$$\omega_n = (\beta \ell)_n^2 \sqrt{\frac{EI}{m \ell^4}} \quad (C.04)$$

where for a cantilever, $\beta \ell = 1.875$ is the lowest eigenvalue.

Mass per unit length

$$m = w/g$$

$$m = 3.06 \times 10^{-5} \text{ lb sec}^2/\text{in}^2$$

Substitution of values into equation C.04 yields

$$\omega_1 = (1.875)^2 \sqrt{\frac{29 \times 10^6 \text{ lbs/in}^2 (1.895 \times 10^4) \text{ in}^4}{(3.06 \times 10^{-5}) \text{ lb sec}^2/\text{in}^2 (6.5)^4 \text{ in}^4}}$$

$$\omega_1 = 1113 \text{ radians per sec}$$

$$\text{or } f_1 = 177 \text{ cycles per second}$$

Since the maximum frequency of interest is 20 cycles per second, the ratio (f/f_1) is sufficiently small for an order of magnitude analysis based on (C.03):

For $x = x_0 \sin \omega t$, the velocity of the probe tip is $\dot{x} = \omega x_0 \cos \omega t$.

Thus the tip velocity, relative to the base, can be further expressed as $x = n \omega x_0 \cos \omega t$ where n is the number of "g's" acceleration.

Converting units from radians to cycles and inches to feet yields an expression for the maximum tip velocity in terms of the test variables n ("g" factor) and f (frequency): $\dot{x}_{\max} = 6.36 n f \times 10^{-6}$ ft/sec

During the nonsteady tunnel test program the maximum horizontal acceleration recorded was one-fourth "g" ($n = 1/4$), while maximum frequencies were 20 cycles per second; thus

$$\dot{x}_{\max} = 6.36 (1/4) (20) \times 10^{-6} \text{ ft/sec}$$

$$\dot{x}_{\max} = 31.8 \times 10^{-6} \text{ ft/sec}$$

The minimum velocity perturbations which occur anywhere in the investigation are about 0.26 feet per second. Therefore \dot{x}_{\max} represents about 0.01 percent and is negligible

Tunnel Floor Velocity Effects on Hotwire Signal

The following analysis was used to determine the velocity produced at the hot wire as a result of tunnel floor velocity, considering the hot wire support to be rigid.

The floor motion was assumed to be simple harmonic, and expressed as

$$x_f = A \sin \omega t \quad (D.01)$$

from which the floor velocity and acceleration are given by

$$\dot{x}_f = \omega A \cos \omega t \quad (D.02)$$

and

$$\ddot{x}_f = -\omega^2 A \sin \omega t \quad (D.03)$$

respectively.

The factor $\omega^2 A$ can be determined from the accelerometer data for each run. Then using the oscillation frequency of that run the maximum displacement, A , can be determined, and the product A is the velocity amplitude. Due to the rather large variations in acceleration, and the fact that the term A varies with frequency, no expression can be obtained which describes the entire test. Instead the quantity A must be computed for each test point.

The following sample calculation indicates the method used:

Run 5-1:

from raw data: $f = 3.7$ cycles per second

$e_c = 0.2$ millivolts (RMS)

accelerometer sensitivity: $k_c = 4.02$ millivolts per "g"

$$\omega^2 A = e_c / k_c = 0.0498 \text{ "g's"} \text{ (RMS)}$$

$$\omega^2 A = 1.60 \text{ feet/sec}^2 \text{ (RMS)}$$

Now the velocity amplitude, ωA , is given by

$$\dot{x}_F = \omega A = \frac{\omega^2 A}{\omega} = \frac{1.60}{2\pi f}$$
$$\dot{x}_F = 0.0689 \text{ ft/sec (RMS)}$$

From previous data reduction

$$e_H = 0.21 \text{ volts (RMS)} \Rightarrow \hat{v} = 24 \text{ ft/sec (RMS)}$$

The relative magnitude is then

$$\dot{x}_F / \hat{v} = 0.00287$$

or about 0.3 percent.

The maximum value of \dot{x}_F / \hat{v} found in the test runs was of the order of 2 percent, which was considered to be a negligible influence.

Quasi-Steady Theory:

The ability of the drag sphere to sense dynamic pressure changes by the change in drag force is clear for "steady" velocity changes, however, the ability of the time-varying drag force to provide a reasonable representation of time-dependent variation of dynamic pressure cannot be assured by a linearized approach unless verified by experiment. The quasi-steady theory, as explained here, is based upon the premise that the drag force coefficient remains invariant and that the instantaneous value of drag is dependent directly upon the instantaneous value of dynamic pressure. Comparison between experiment and quasi-steady theory is the purpose of this research, with the goal of showing both the drag magnitude and phase shift as a function of dimensionless frequency. Quasi-steady theory assumes no phase shift.

If the velocity is assumed to be a harmonic component superimposed upon a steady term, then we have that:

$$V + v(t) = V \left(1 + \sigma \sin \omega t \right) \quad (\text{E.01})$$

where σ represents the amplitude ratio between unsteady and steady velocity. The instantaneous value of dynamic pressure can then be expressed as:

$$q = \frac{1}{2} \rho V^2 \left[\left(1 + \frac{\sigma^2}{2} \right) + 2\sigma \sin \omega t - \frac{\sigma^2}{2} \cos 2\omega t \right] \quad (\text{E.02})$$

Applying the quasi-steady assumption to drag force yields:

$$D + d(t) = \frac{1}{2} \rho C_D A V^2 \left[\left(1 + \frac{\sigma^2}{2} \right) + 2\sigma \sin \omega t - \frac{\sigma^2}{2} \cos 2\omega t \right] \quad (\text{E.03})$$

It will be noted that the steady drag term increases slightly over the value in uniform flow due to the presence of the $\sigma^2/2$ term in equation E.03 . As explained in Section 3, the influence of the term was experimentally verified as being small, which is reasonable to expect for velocity perturbations up to about 15 percent of the steady velocity; i.e., $|v(t)| \leq 0.15 V$.

From equation E.03, we can readily discern that the ratio of unsteady drag to steady drag by quasi-steady theory is given by:

$$\frac{d(t)}{D} = 2 \sigma \sin \omega t - \frac{\sigma^2}{2} \cos 2\omega t \quad (\text{E.04})$$

Next we consider equation E.04 from the standpoint of mean square values, which becomes upon applying the limit operation for the mean square of a temporally varying term:

$$\begin{aligned} \frac{\overline{d^2}}{D} &= \lim_{T \rightarrow \infty} \left\{ \frac{1}{T} \int_0^T (4 \sigma^2 \sin^2 \omega t - 2 \sigma^3 \sin \omega t \cos 2\omega t + \frac{\sigma^4}{4} \cos^2 2\omega t) dt \right\} \\ \frac{\overline{d^2}}{D} &= 2 \sigma^2 \left(1 + \frac{\sigma^2}{16} \right) \end{aligned} \quad (\text{E.05})$$

Defining $\hat{d} = \sqrt{\overline{d^2}}$ and considering equation E.05,

$$\frac{\hat{d}}{D} = \sqrt{2} \sigma \left(1 + \frac{\sigma^2}{16} \right)^{1/2} = \sqrt{2} \sigma \left(1 + \frac{\sigma^2}{32} + \dots \right)$$

We now must recognize that the velocity perturbation σ corresponds to a peak amplitude and may be expressed in terms of the RMS of velocity perturbation, ϵ , by $\sigma = \sqrt{2} \epsilon$.

Hence we obtain that

$$\frac{\hat{d}}{D} = 2 \epsilon \left(1 + \frac{\epsilon^2}{16} + \dots \right)$$

which to a first order term may be stated as:

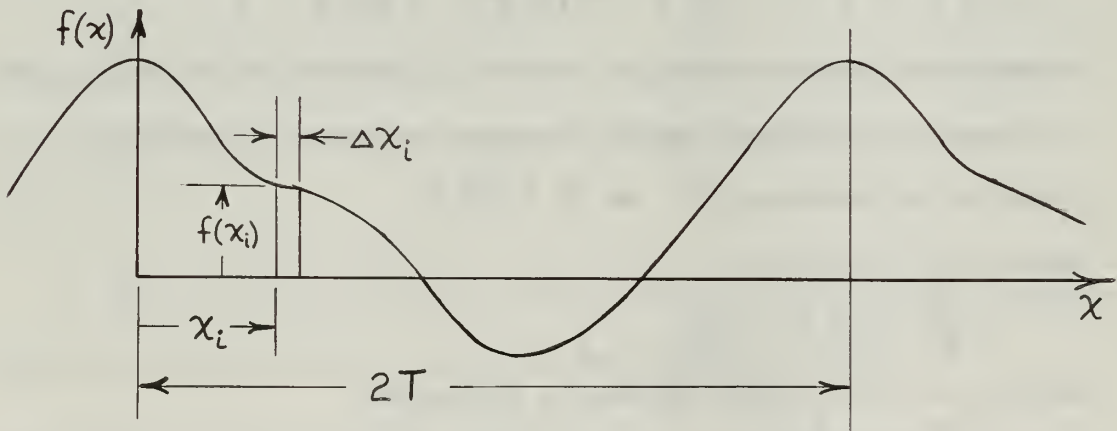
$$\frac{\hat{d}}{D} = 2 \frac{\hat{v}}{V} \quad (\text{E.06})$$

Equation E.06 is a statement of the quasi-steady drag ratio as used in Section 3 of this analysis.

Fourier Analysis of Signal:

A simple analysis was made of the time varying electrical signals from the hot wire and drag sphere anemometer in order to evaluate the quality of the unsteady velocity perturbation and the response of the anemometer to the various harmonics. Strictly speaking, the analysis using a Fourier series of consecutive harmonics is not valid for this experimental program, since it is possible that a frequency may be present in the signal which is not an integer multiple of the fundamental, and hence a Fourier analysis using a truncated series could give a false indication of signal content. However, the Fourier approach was rationalized in this instance on the basis that the time to do a true power spectral and cross-spectral analysis was not consistent with the available time, and at least an approximate indication of frequency content had to be obtained.

Consider a periodic function of period $2T$ as shown in the sketch below:



The Fourier series representation for the cyclical function may be expressed as:

$$f(x) = \frac{A_0}{2} + \sum_{n=1}^{\infty} \left(A_n \cos \frac{n\pi x}{T} + B_n \sin \frac{n\pi x}{T} \right) \quad (F.01)$$

where

$$A_n = \frac{1}{T} \int_0^{2T} f(x) \cos \frac{n\pi x}{T} dx, \quad n = 0, 1, 2, \dots \quad (F.02)$$

$$B_n = \frac{1}{T} \int_0^{2T} f(x) \sin \frac{n\pi x}{T} dx, \quad n = 1, 2, 3, \dots \quad (F.03)$$

One complete cycle of the signal to be analyzed was obtained from an oscilloscope photograph (cf., Figure 30) and divided into 36 equal parts, such that

$$36 \Delta x_i = 2\pi \text{ radians} = 360 \text{ degrees}$$

$$\Delta x_i = 10 \text{ degrees}$$

$$x_i = 10i \text{ degrees } (i = 0, 1, 2, \dots, 35)$$

Now express period as

$$2T = 360 \text{ degrees}$$

Then at each 10 degree station (x_i) through the cycle, the amplitude, $f(x_i)$, was measured. This information allowed the coefficients, A_n and B_n , to be evaluated, using a numerical approximation to the integral equations F.02 and F.03, as

$$A_n = \frac{1}{180} \sum_{i=0}^{35} f(x_i) \cos nx_i \Delta x_i \quad (F.04)$$

which, with $x_i = 10$ degrees, is

$$A_n = \frac{1}{18} \sum_{i=0}^{35} f(x_i) \cos nx_i \quad (F.05)$$

Similarly

$$B_n = \frac{1}{18} \sum_{i=0}^{35} f(x_i) \sin nx_i \quad (F.06)$$

Equation (F.01) may be alternately expressed as

$$f(x) = \frac{A_0}{2} + \sum_{n=1}^{\infty} C_n \cos(\omega_n t - \phi_n) \quad (F.07)$$

where

$$C_n = \sqrt{A_n^2 + B_n^2} \quad (F.08)$$

and

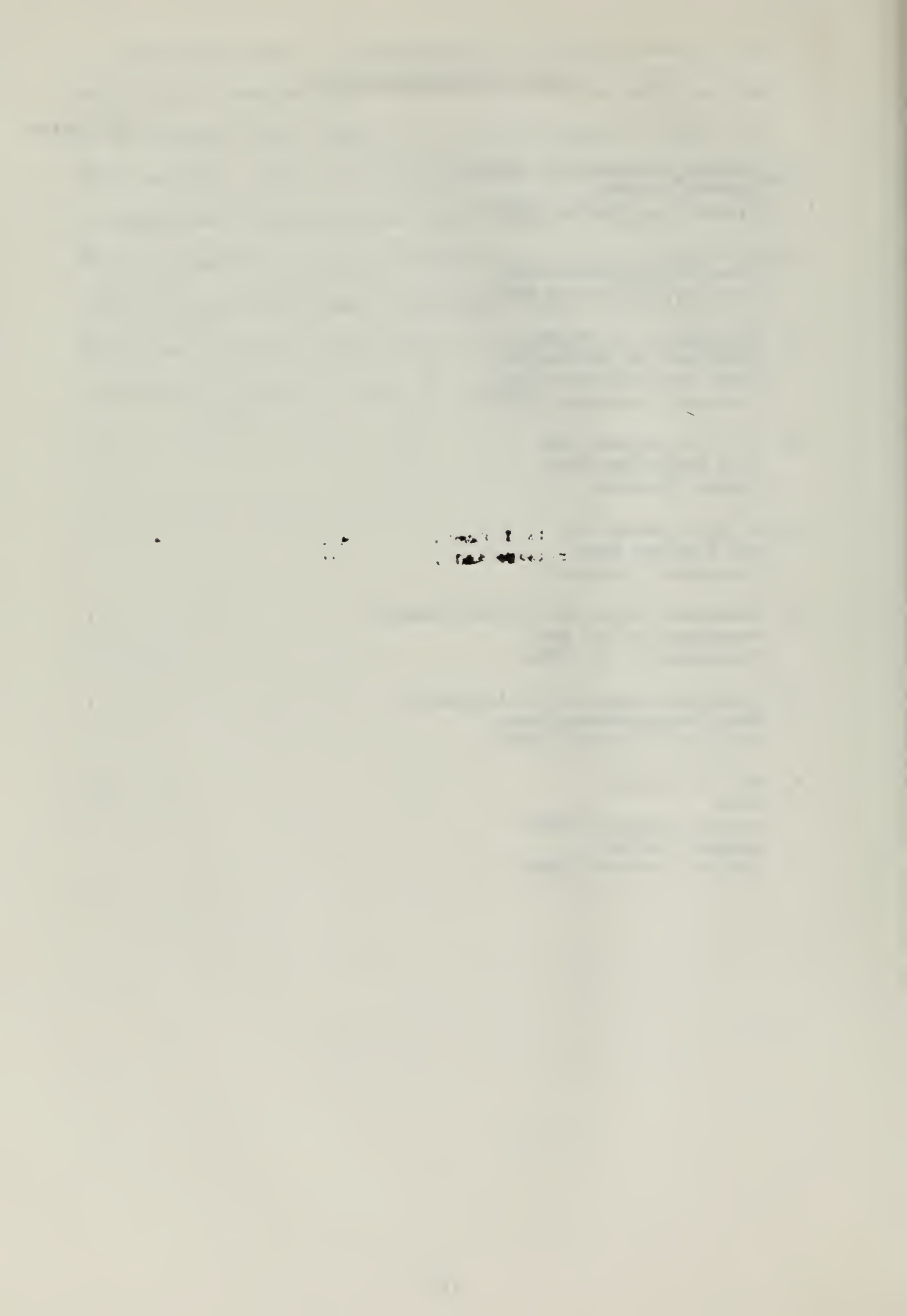
$$\phi_n = \arctan \left[\frac{B_n}{A_n} \right] \quad (F.09)$$

The constant term, A_0 , is a function of the axis location (from which $f(x_i)$ is measured) and is of no value in this analysis. Only three components were computed, i.e., the fundamental, second, and third harmonic. After C_n was computed ($n = 1, 2, 3$) for a given signal, the magnitudes of the second and third harmonic components, relative to the fundamental, was given by the ratios, C_2/C_1 and C_3/C_1 . Computation of ϕ_n provided phase relationships among components of one signal, and also phase relationships between two signals processed relative to the same time scale and origin.

INITIAL DISTRIBUTION LIST

No. Copies

1. Defense Documentation Center
Cameron Station
Alexandria, Virginia 22314 20
2. Library
Naval Postgraduate School
Monterey, California 93940 2
3. Professor L. V. Schmidt
Department of Aeronautics
Naval Postgraduate School
Monterey, California 93940 2
4. LT J. D. Laferty, USN
1541 Longfellow Court
McLean, Virginia 1
5. LT W. F. Hicks, USN
205 Elmhurst Lane
Portsmouth, Virginia 1
6. Commander, Naval Air Systems Command
Department of the Navy
Washington, D. C. 20360 1
7. Chairman, Department of Aeronautics
Naval Postgraduate School
Monterey, California 93940 1
8. Mr. W. H. Reed
NASA
Langley Research Center
Langley Station
Hampton, Virginia 23365 10



DOCUMENT CONTROL DATA - R&D

(Security classification of title, body of abstract and indexing annotation must be entered when the overall report is classified)

1. ORIGINATING ACTIVITY (Corporate author) Naval Postgraduate School Monterey, California		2a. REPORT SECURITY CLASSIFICATION UNCLASSIFIED	
		2b. GROUP	
3. REPORT TITLE AN INVESTIGATION OF THE AERODYNAMIC RESPONSE OF A WIND ANEMOMETER			
4. DESCRIPTIVE NOTES (Type of report and inclusive dates) Thesis			
5. AUTHOR(S) (Last name, first name, initial) LAFERTY, J. D., LT, USN HICKS, W. F., LT, USN			
6. REPORT DATE June 1967		7a. TOTAL NO. OF PAGES 116	7b. NO. OF REFS 11
8a. CONTRACT OR GRANT NO.		9a. ORIGINATOR'S REPORT NUMBER(S)	
b. PROJECT NO.			
c.		9b. OTHER REPORT NO(S) (Any other numbers that may be assigned to this report)	
d.		This document has been approved for public release and sale; its distribution is unlimited.	
10. AVAILABILITY/LIMITATION NOTICES This report is subject to special export controls and such information to foreign governments or foreign nationals may be made only with prior approval of the Naval Postgraduate School.			
11. SUPPLEMENTARY NOTES		12. SPONSORING MILITARY ACTIVITY Naval Postgraduate School Monterey, California	

13. ABSTRACT

An experimental investigation was made to determine the aerodynamic response of a wind anemometer to unsteady air loads. The anemometer, a perforated drag sphere mounted upon a cylindrical pedestal, sensed dynamic pressure by a strain gage balance system. The anemometer response was calibrated for static and dynamic mechanical inputs and for steady aerodynamic loads prior to the unsteady investigation. The unsteady environment was obtained in an oscillating flow wind tunnel which utilizes a rotating shutter valve to superimpose a harmonically varying velocity upon a mean free stream. For steady flow conditions the anemometer drag coefficient remained essentially constant, apparently independent of Reynolds number. The anemometer responded well to the unsteady air loads at frequencies up to 20 cycles per second and mean dynamic pressures to 8.85 pounds per square foot. Unsteady aerodynamic response was qualitatively substantiated by a quasi-steady approximation to the measured unsteady drag.

14.

KEY WORDS

LINK A

LINK B

LINK C

ROLE

WT

ROLE

WT

ROLE

WT

Anemometer
Drag Sphere
Unsteady Flow
Oscillating Flow
Drag, Unsteady



thesL2414

An investigation of the aerodynamic resp



3 2768 002 11266 6

DUDLEY KNOX LIBRARY